Control of capillary break-up in spiralling liquid jets

Suriyaprakash Senthil Kumar

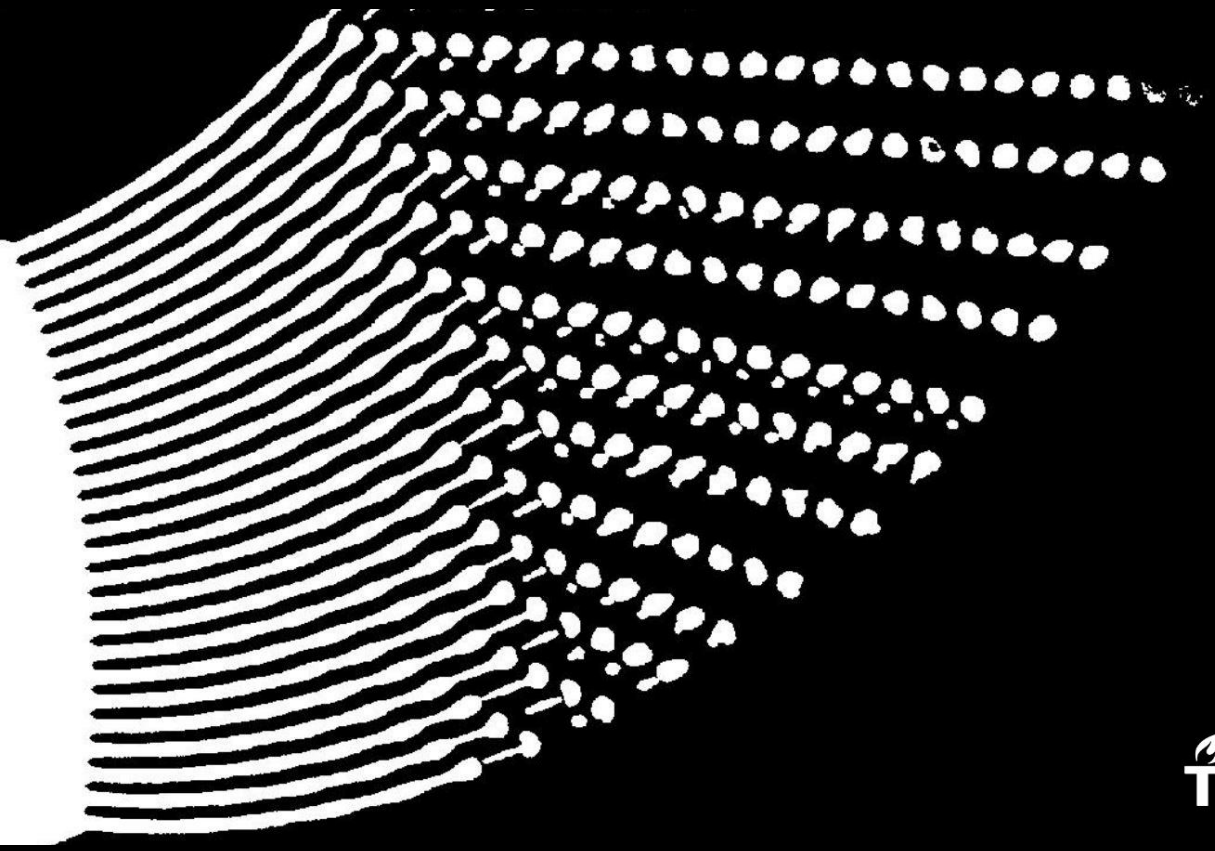

TU Delft

TU Delft

Control of capillary break-up in spiralling liquid jets

by

Suriyaprakash Senthil Kumar

to obtain the degree of Master of Science
at the Delft University of Technology,
to be defended publicly on Tuesday September 22, 2020 at 14:00 hours.
P & E report number: 3030

Student number:	4771893	
Project duration:	October 15, 2019 – September 22, 2020	
Thesis committee:	Dr. ir. W.-P Breugem,	TU Delft, supervisor
	Dr. ir. H. B. Eral,	TU Delft, supervisor
	Dr. ir. L. Botto	TU Delft
	Dr. L. Portela	TU Delft
	Ir. Y. E. Kamis,	TU Delft, Daily supervisor

This thesis is confidential and cannot be made public until September 22, 2020.

Acknowledgement

I would like to thank my supervisors **Dr. Burak H. Eral** and **Dr. Wim-Paul Breugem** for giving me the opportunity to work on this thesis. They gave me ample responsibility and plenty of freedom for my research, whilst helping me with mathematical and experimental details, and always guided my attention to focus on the bigger picture. Their enthusiasm, drive and the appreciation they gave me was one of the most motivating factors throughout my entire thesis. My daily supervisor **Yavuz E. Kamis** was always there guiding me; I can't thank him enough. The countless hours we spent doing instability derivations will be some of the best memories of my master thesis life.

I would like to extend my gratitude to the technicians in the Fluid mechanics lab who supported the building of my experimental setup. **Edwin Overmars**, **Jan Graafland**, **Jasper Ruijgrok** and **Gertjan Mulder** were the ones who advised me on camera, manufacturing consumables, electronics for motor and miscellaneous equipment. Needless to say, more than half of my thesis time was in corona lock down imposed by the Dutch government, without the extra effort these people put in to help me, my thesis wouldn't have been completed on time.

I collaborated with my colleagues and PhD students in the fluid mechanics lab to get ideas for my experimental setup. This was very crucial to build a novel experimental rig. **Shravan**, **Floor**, **Vasu**, **Mike**, **Bob**, **Wout**, **Sudharshan**, **Willian**, **Ankur** and **Udhav** were always available for short discussions.

This project was partly funded by Kreber B. V. in Vlaardingen. Kreber was also generous to me, lending their piezo-electric crystal and also manufacturing the spiraling jet experimental setup. Their timely delivery of the products and their collaboration in this project was invaluable. I thank **Gelmer**, **Toon** and **Marco** for their spirited discussions.

The interest in fluid mechanics was instilled in me by professors in TU delft and in PSG College where I did my bachelor studies. I thank professors Dr. Madhu Ganesh (PSG), Dr. Wim-Paul Breugem, Dr. Burak Eral, Dr. Daniel Tam, Dr. Mathieu Pourquie and Dr. Rene Delfos for introducing me to the exciting world of fluid mechanics.

Living thousands of miles away from my motherland never took a toll on me, thanks to my friends who made delft my home away from home. My time spent with **Floor, Vasu, Jip, Bob, Xiao, Lyke, Keerthana, Thea, Lowik, Tim, Diego, EFPT Prescott Joule student association** were the most memorable of my time so far in the Netherlands. Finally, I would like to thank my parents who made is possible to pursue my dream of master's education in TU Delft. I am forever indebted to their unconditional love and support.

Suriyaprakash Senthil Kumar
Delft, September 2020

Abstract

A cylindrical column of fluid breaks into drops under the action of surface tension when other forces are relatively small. This phenomenon is called the capillary break-up. Since the introduction of the seminal theory of inertial-capillary jet instability by Rayleigh in the late 19^{th} century, this phenomenon has seen a rich influx of academic research and industrial interests over the past few decades. The theory suggests that out of all the unstable wavelengths only the most unstable wavelength determines the drop size. But in reality, random background perturbations and non-linear pinch-off dynamics result in bi-modal drop size distribution. The two peaks in the bi-modal distribution correspond to the formation of main drops and satellite drops. The main drops are the desired product of the industry and the satellite drops are relatively smaller in size and are discarded by post-production processes like sieving. To reduce post-production processes and ensure repeatability, the industrial demand is to have a "narrow uni-modal" drop size distribution. Meaning, elimination of satellite drops and having uniform-sized main drops.

Narrow distribution is achieved by employing finite-amplitude perturbation on the jet. This way the jet is not affected by the random background perturbation as the finite-amplitude perturbation dominates the break-up process. But this does not ensure satellite drop elimination. Uni-modality is achieved when the satellite drops merge with the main drops. Merging happens when the satellite and the main drop have different velocities and follow the same trajectory. The amplitude of the sinusoidal perturbation can be tuned to have this merging condition. The externally perturbed jet finds its application in a plethora of industrial processes such as powder production, combustion, micro-encapsulation, extreme ultraviolet rays (EUV) and, laser-plasma production (LPP), ink-jet printing, etc.

The focus of this thesis is the production of crystalline fertilizer pellets from the capillary break-up of a spiralling jet of molten fertilizer. This process is called rotary prilling. Experimental studies in spiraling jets without external perturbation also shows bi-modal distribution of drops. The fine satellite drops produced in prilling process are a potential safety hazard as they can cause dust explosions which can be detrimental to air quality. Expensive filters and wet scrubbers are placed inside the prilling tower to remove the fine satellite drops. Hence uni-modal drop size distribution in prilling is highly beneficial for both economic and environmental reasons. As perturbed spiralling jets are not studied in detail in the existing literature, this thesis employs sinusoidal perturbations on spiraling water jets and aims to achieve uni-modal drop size distribution.

While the straight jets have a nearly constant base flow, the spiraling jets have a base flow that accelerates due to the centrifugal and Coriolis forces in the downstream direction. As a result of mass conservation the accelerating base flow results in jet stretching in the downstream direction. The evolution of perturbations on such a stretched jet not only depends on surface tension and inertial forces of the local jet radius, but also on the wavelength that is excited initially. Hence the evolution of perturbations on straight jets with constant base flow is an eigen-value problem whereas, on a stretched jet it is an initial value problem. When the stretching rate is faster than the capillary growth rate damping of the surface perturbations will occur. For the process parameters investigated in this thesis, the capillary growth rate is faster resulting in negligible damping. The other effect of jet stretching is that the wavelengths are also stretched, that is the wavelength that is excited initially becomes longer in the downstream direction, thus the wavenumber decreases.

The linear spatial instability theory for spiraling jets is experimentally validated in this thesis. For the set of non-dimensional numbers chosen in this thesis, uni-modal distribution of drops is achieved by tuning the frequency and amplitude of the sinusoidal perturbation. Uni-modality is observed when the non-dimensional wavenumber near break-up is approximately 0.7 and the amplitude is tuned accordingly. As the wavenumber decreases in downstream direction the wavenumber excited at the nozzle should be greater than 0.7.

Contents

Nomenclature

We - Weber number
Fr - Froude number
Oh - Ohnesorge number
Rb - Rossby number
We_{cr} - Critical weber number
g - gravity (m/s^2)
Ω - Angular velocity of spiralling jet (rad/s)
C_d - Coefficient of discharge
λ - Wavelength (m)
k - Wave number (1/m)
k_r - Real wave number (1/m)
ω - Angular frequency of perturbation (1/s)
ω_r - Real angular frequency of perturbation (1/s)
k_i - Spatial growth rate of perturbations (1/m)
ω_i - Temporal growth rate of perturbations (1/s)
k^* - Non-dimensional wave number
k_r^* - Non-dimensional real wave number
ω^* - Non-dimensional angular frequency of perturbation
ω_r^* - Non-dimensional real angular frequency of perturbation
k_i^* - Non-dimensional spatial growth rate of perturbations
ω_i^* - Non-dimensional temporal growth rate of perturbations
σ - Strain rate (1/s)
SD - Standard deviation
U - Velocity at the nozzle of the jet (m/s)
H - Radius at the nozzle (m)
t_c - Capillary time scale (s)
γ - Surface tension (N/m)
ρ - Density of the liquid (kg/m^3)
t_a - Advection time scale (s)
ν - Viscosity of the liquid (Pa s)
t_b - Break up time of jet (s)
L_{BU} - Break up length (m)
ϵ_u - Perturbation amplitude in velocity at the nozzle
ϵ_h - Perturbation amplitude in radius at the nozzle
δ - Small perturbation

List of Figures

List of Tables

1

Introduction

Narrowly dispersed drops when required in high production rates, of the order of a few tons per hour, the process adopted is prilling (see Van't Land [43]). Some of the most commonly prilled materials are made for the fertilizer industry producing urea and ammonium nitrate. The prilling process has a cylindrical or conically shaped perforated bucket (also called prillers), shown in figure 1.1. Typically these bucket are of diameter of 0.5 m and the size of perforated holes are of the order of 1 mm. The bucket is filled with the

Figure 1.1: Perforated rotary bucket (Courtesy of Kreber, Vlaardingen, The Netherlands)

molten liquid that is to be prilled and is rotated at speeds of utmost 350 rpm. The high rotation rate increases the radial pressure in the molten liquid near the walls and hence the liquid is forced out of the perforations. The jets coming out of these perforations eventually undergo capillary break-up and form drops. These drops are then cooled for the crystallisation to initiate. The crystallised drops are called as prills. The cooling is facilitated by the prilling tower built around the perforated bucket. A schematic of the entire prilling process is shown in figure 1.2. The entire assembly of the bucket is enclosed in a prill tower which could be utmost 60 m tall and provides enough residence time for the drops to crystallise. To increase the heat transfer a counter

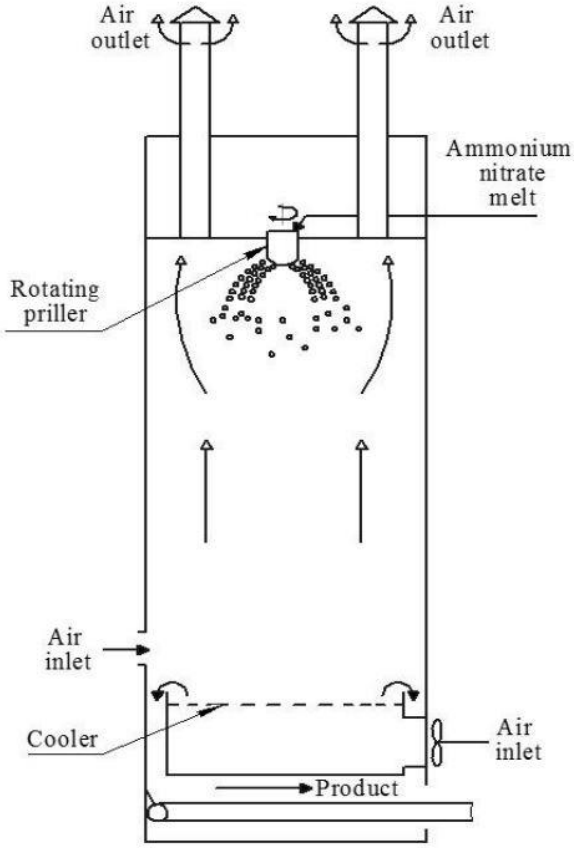

Figure 1.2: Schematic of prilling process, reproduced from Skydanenko et al. 2017

flow arrangement of air flow is also found in the prilling tower. Finally, the prills are collected at the bottom of the tower.

Although a narrow range of drop sizes is claimed in the prilling process, there is still a bi-modal distribution of drop sizes (see Wong et al. [45]). This is because of the near break up non-linearity which results in two drop sizes, viz. main drops (desired ones) and satellite drops. These satellite drops are undesirable for many reasons. As the satellites are some times very fine, of the order of few microns, the counter-flow air carries these fine drops in to the atmosphere. This can cause serious environmental issues such as dust explosion. Hence the counter-flow air is passed through cyclone separators or wet scrubbers to filter them. These filters contribute to additional equipment costs and also incur maintenance costs [43]. Moreover, satellite drops that are filtered results in loss of valuable material. Owing to these issues with the satellite drops this study aims to eliminate[1] them in a dimensionally similar experimental setup with water as the working fluid.

1.1. Outline of thesis

A brief overview of the theory of break-up for straight jets and spiralling jets is presented in chapter 1 followed by the literature review. Chapter 2 deals with straight jets in detail and presents the preliminary experiments done in straight jets. Chapter 3 discusses the new improved experimental setup for understanding the spiralling jets and also discusses the post-processing of image data obtained from spiralling jet experiments. The results are presented in chapter 4 and the agreement of experimental results with the theory is discussed. Conclusion of the thesis and future recommendations are given in chapter 5.

[1]The satellite drops are universal and are always present in jet breakup. In this thesis, "elimination of satellite" means a controlled merging of the satellite drops with the main drops.

1.2. Theory

1.2.1. Rayleigh's linear instability theory

Rayleigh [31] solved the linearized Navier-Stokes equation and the kinematic boundary condition corresponding to a radially perturbed straight jet.

$$h = h_0 + \tilde{h} \tag{1.1}$$

$$\tilde{h} = \delta e^{i(kx-\omega t)} \quad \text{where, } \omega = \omega_r + i\omega_i \tag{1.2}$$

$$\tilde{h} = \delta e^{\omega_i t} e^{i(kx-\omega_r t)} \tag{1.3}$$

The radial perturbations are given in equations 1.1 and 1.3. h_0 is the unperturbed jet radius and $\tilde{h}$ is the perturbation imposed on it. ω_r is the angular frequency of perturbation and ω_i is the growth rate. 'x' is the streamwise direction and 'r' is the radial direction of the jet.

$$\omega^2 = -\frac{\gamma}{\rho h_0^3}(kh_0)(1-(kh_0)^2)\frac{I_1(kh_0)}{I_0(kh_0)} \tag{1.4}$$

The dispersion relation obtained by Rayleigh is given in the equation 1.4. Where, k ($=\frac{2\pi}{\lambda}$) is the wavenumber, ρ & γ are the density & surface tension of the liquid, and I_0 and I_1 are the 0^{th} order and 1^{st} order modified Bessel function of the first kind. When ω has a non-zero imaginary part it can be seen from equation 1.3 that the perturbations grow exponentially and lead to break-up. The dispersion relation gives the growth rate associated with a particular wavenumber. Figure 1.3 shows the imaginary part of ω (growth rate) scaled by the capillary time ($t_c = \sqrt{\rho h_0^3/\gamma}$) plotted against the non-dimensional wavenumber ($k^* = kh_0$).

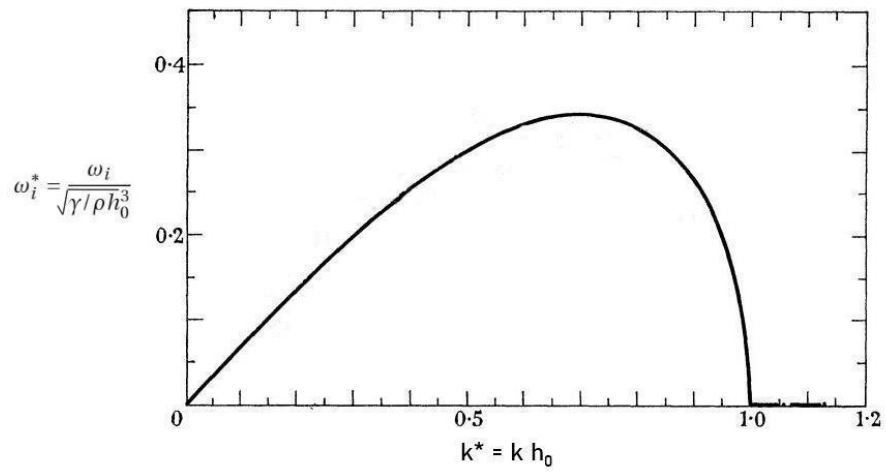

Figure 1.3: Non-dimensional growth rate plotted against the non-dimensional wavenumber, reproduced from Donnelly and Glaberson [7]

It can seen from the figure 1.3 that the fastest growing dimensionless wavenumber is approximately 0.7. This wavenumber will dominate the break-up process and will correspond to the drop size. With the intertial-capillary time scale (t_c) being one of the relevant time scales, the other time scale that is relevant is the advection time scale (t_a) given in equation 1.5.

$$t_a = h_0/u_0 \tag{1.5}$$

$$We = \frac{t_c^2}{t_a^2} = \frac{\rho u_0^2 h_0}{\gamma} \tag{1.6}$$

Where u_0 is the jet velocity in the streamwise direction. The square of the ratio of these two time scales gives the Weber number (We) as shown in equation 1.6.

1.2.2. Slender jet analysis

A slender jet assumption is valid when the length scale in the streamwise direction (l_x) is much longer than the length scale in radial direction (l_r) of the jet. Subtituting this into the linearized Navier-Stokes equation gives a one dimensional approximation of the jet.

$$\omega^2 = -\frac{1}{2}\frac{\gamma}{\rho h_0^3}\left[(kh_0)^2 - (kh_0)^4\right] \tag{1.7}$$

Equation 1.7 is the dispersion relation obtained from such a 1-D model. The solution of the 1-D model is more transparent than the one given by Rayleigh [31] and allows incorporating more complexities. For instance, jets with finite viscosities can be incorporated with ease. The dispersion relation for viscous jets is given in the equation 1.8. Where ν is the dynamic viscosity of the jet.

$$\omega^2 = -\frac{1}{2}\frac{\gamma}{\rho h_0^3}\left[(kh_0)^2 - (kh_0)^4\right] + (-i\omega)\frac{3\nu}{h_0^2}(kh_0)^2 \tag{1.8}$$

$$t_a = \nu h_0/\gamma \tag{1.9}$$

The inclusion of viscosity brings in a new time scale known as the visco-capillary time scale (t_ν), given in equation 1.9. The effect of viscosity on the capillary growth is measured in terms of the Ohnesorge number (Oh) which is the ratio of the visco-capillary time scale to interial-capillary time scale and is given in equation 1.11.

$$Oh = \frac{t_\nu}{t_c} \tag{1.10}$$

$$Oh = \frac{\nu}{\sqrt{\rho h_0 \gamma}} \tag{1.11}$$

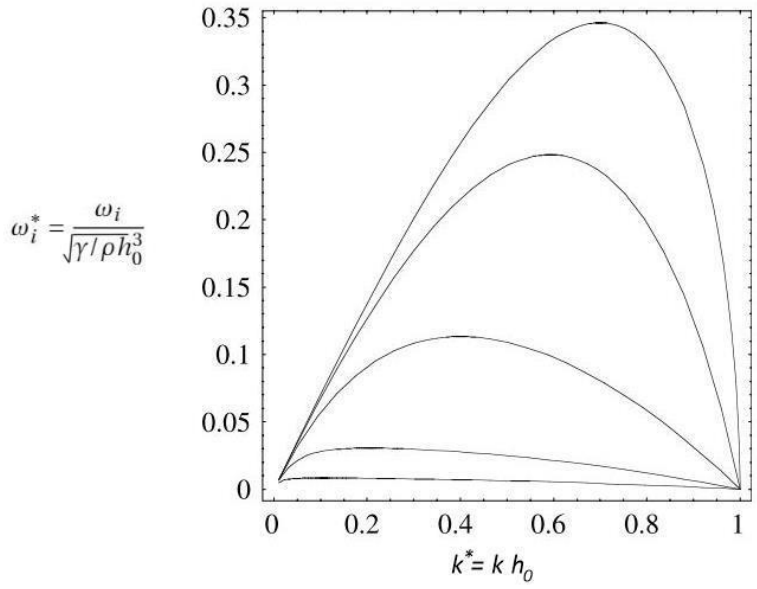

Figure 1.4: Non-dimensional growth rate plotted against the non-dimensional wavenumber for increasing Oh numbers $Oh = 0.01, 0.2, 1, 5, 20.$ (top to bottom in the graph) , reproduced from Eggers and Villermaux [12]

The capillary growth rate for different Oh numbers is shown in figure 1.4. It can be seen that increasing viscosity slows down the capillary growth rate.

1.2.3. Satellite drop formation

Although the growth of the capillary perturbations are governed by linear theory the near break-up phenomena are non-linear in nature. When following a sinusoidal perturbation over time it was found that the sinusoidal waves deviate from their sine shape. It was first noticed in jets by Goedde and Yuen [15]. Figure 1.5 shows the temporal evolution of sinusoidal waves becoming non-sinusoidal.

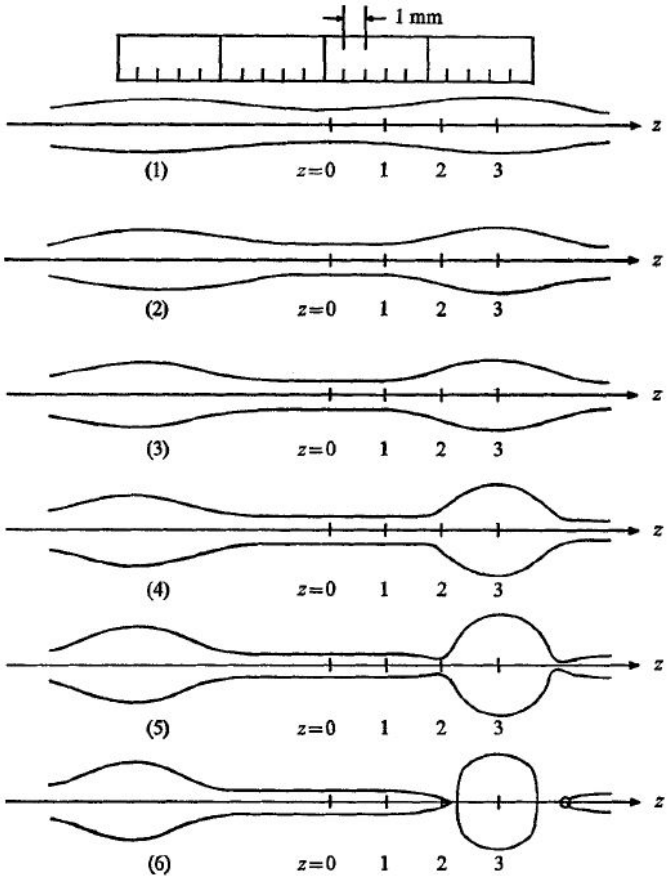

Figure 1.5: Trace of water jet surface in time sequence measured from experiments, the jet corresponds to a perturbation frequency of dimensionless wavenumber 0.43, reproduced from Goedde and Yuen [15]

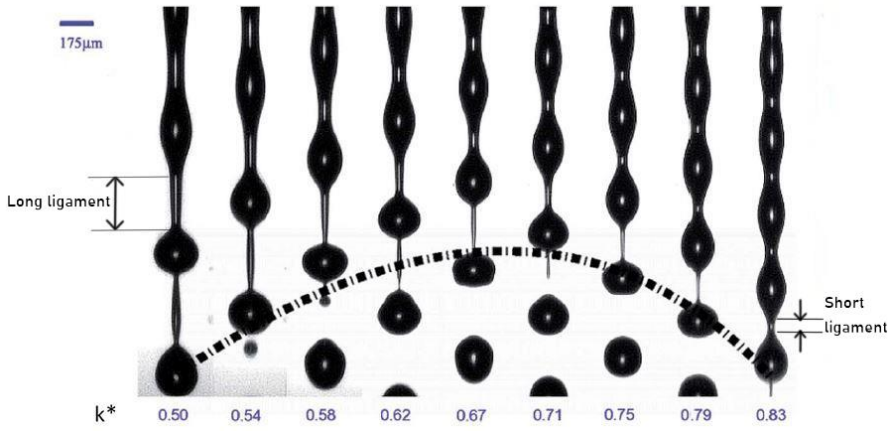

Figure 1.6: Jet perturbed at different wavelengths. It can be seen that the ligament size becomes smaller with decreasing wavelengths (left to right), reproduced from Sharma et al. [37]

The jet break-ups into drops with ligaments in between them. These ligament recoil into smaller drops

also called as the satellite drops. The longer the wavelength of perturbation the longer the ligament size is, which results in bigger satellite drops. Figure 1.6 shows the same jet perturbed at different wavelengths and the corresponding ligament lengths. As the wavelength of perturbation decreases (left to right) it can be seen that the ligament size also decreases and smaller satellite drops are formed. Thus the non-dimensional wavenumber ($k^* = 2\pi h_0/\lambda$) becomes an important dimensionless number for satellite drop formation. Although satellite drops are formed ubiquitously (see Eggers [9]), they merge with the main drops downstream. The merging phenomena depends on the amplitude of perturbation. At low perturbation amplitudes forward separation and rear merging is observed. A forward separation is when the ligament pinches off form the main drop first at its fore end. The resulting un-balanced momentum causes the satellite to merge with the main drop behind it, hence the term rear merging. The time evolution of such a forward separation and rear merging is shown in figure 1.7.

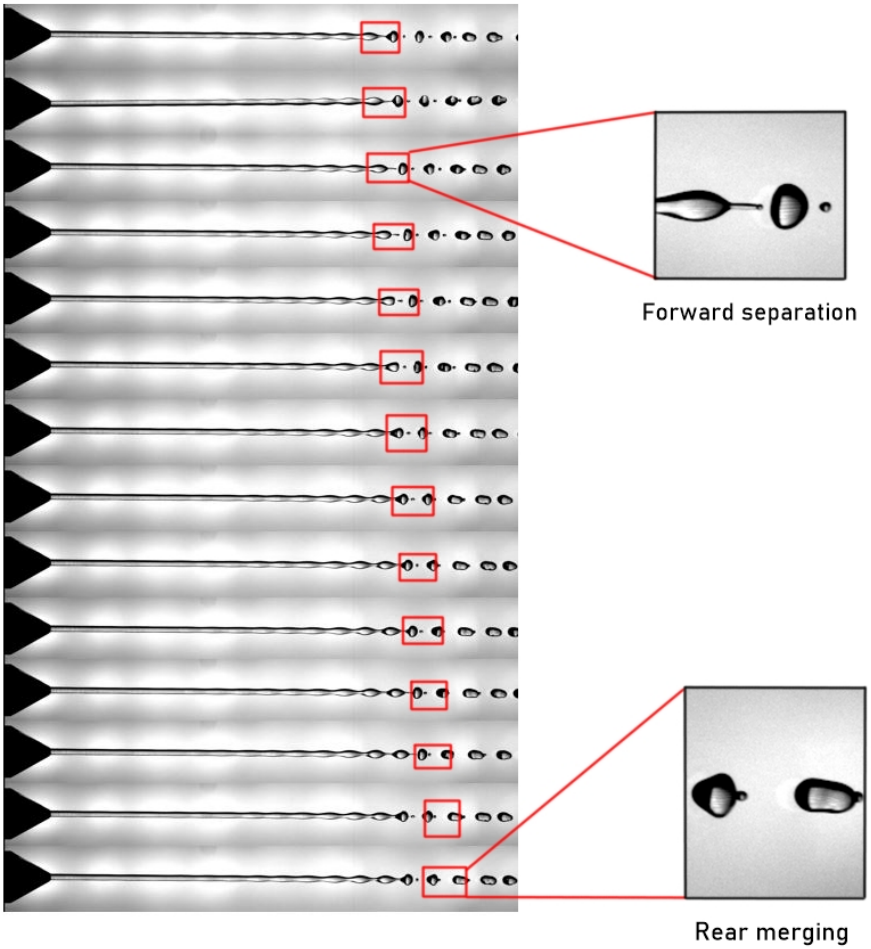

Figure 1.7: Time evolution of straight jet depicting forward separation and rear merging. These images are taken by the author of this thesis. The jet is perturbed at the fastest growing wavelength and the images are taken at 4000 fps. The voltage applied to the piezo crystal is 40 V.

As the amplitude of the perturbation is increased the infinite satellite condition is encountered. This occurs when the satellite break-ups from the fore end and rear end simultaneously. This is termed as the, "infinity condition" by Pimbley and Lee [29]. The satellite does not have any unbalanced momentum, so the relative velocity of the satellite with respect to the main drops is zero. Hence the satellite does not merge with the main drops. Figure 1.8 shows the infinity condition.

Moving from rear merging condition to infinity condition it is also seen that the merging time increases and when the infinity condition is reached the merging time becomes infinity. When the amplitude of perturbation is increased beyond the infinity condition the satellite pinches off form the rear end and merges with the main drop upstream. This is called rear separation and forward merging. As the amplitude is increased even further the merging time in the forward direction decreases. Figure 1.9 shows the condition of

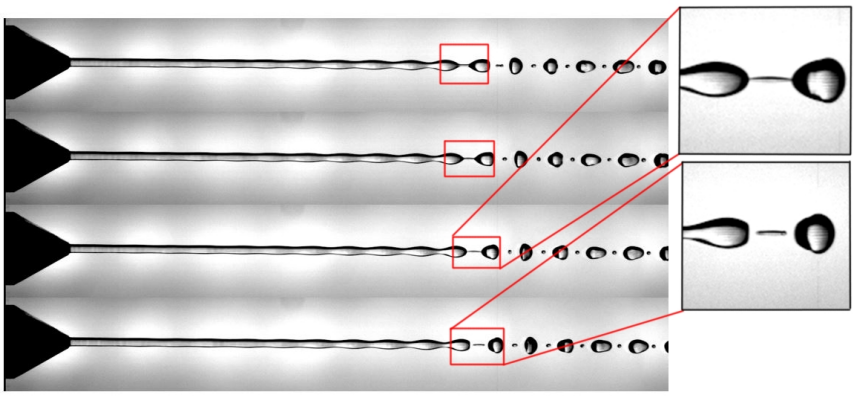

Figure 1.8: Time evolution of straight jet depicting the infinity condition. These images are taken by the author of this thesis. The jet is perturbed at the fastest growing wavelength and the images are taken at 4000 fps. The voltage applied to the piezo crystal is 65 V.

rear separation and forward merging. Thus for a given non-dimensional wavenumber, the non-dimensional amplitude of perturbation decides the type of merging and the merging time.

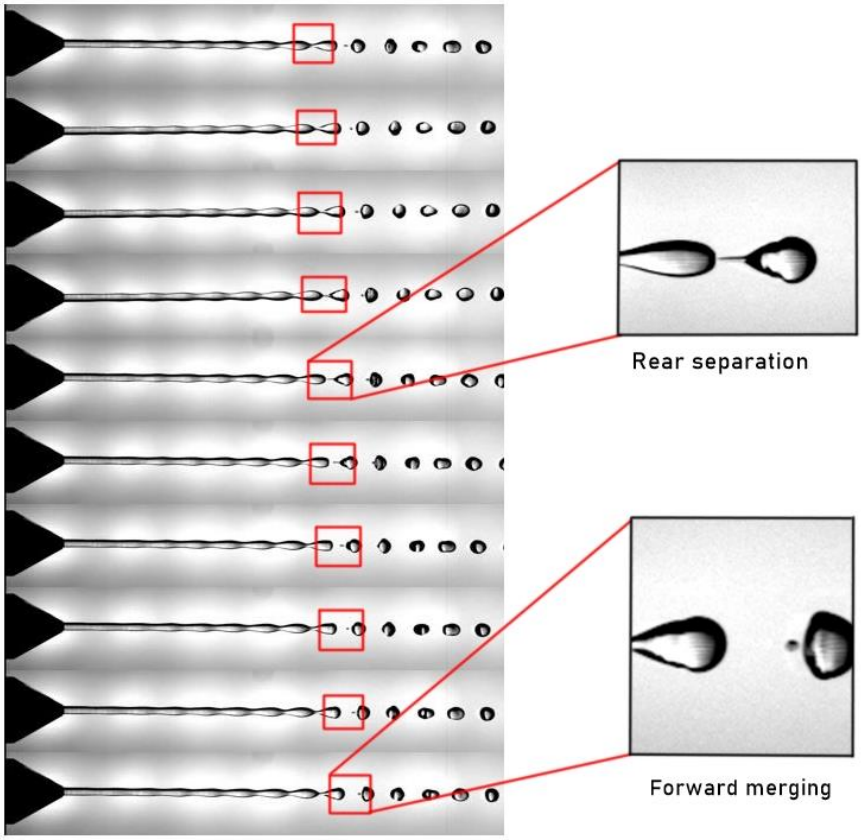

Figure 1.9: Time evolution of straight jet depicting rear separation and forward merging. These images are taken by the author of this thesis. The jet is perturbed at the fastest growing wavelength and the images are taken at 4000 fps. The voltage applied to the piezo crystal is 150 V.

1.2.4. Stability of thinning jets

In the previous analysis the instability of a jet with constant base flow is presented. In this section a jet that is accelerating is considered. An accelerating jets thins in radius in the downstream direction due to mass conservation. The growth of capillary waves on such a temporally evolving jet becomes an initial value problem.

$$u_0 = \sigma x, \tag{1.12}$$

$$v_0 = \frac{-\sigma}{2} r \tag{1.13}$$

The base flow velocities are given in equations 1.12 and 1.13. Here σ is the strain rate, and u_0 and v_0 are the velocity in x and r direction. Integrating equation 1.13 gives the radius of the base flow as a function of time which is given as,

$$h_0(t) = h_0(0) e^{\frac{-\sigma}{2} t} \tag{1.14}$$

and integrating equation 1.12 gives the stretching of a fluid element in the base flow as a function of time which is given as,

$$\delta x(t) = \delta x(0) e^{\sigma t} \tag{1.15}$$

Hence the wavelength that is excited at the nozzle temporally evolves as,

$$\lambda(t) = \lambda(0) e^{\sigma t} \tag{1.16}$$

$$k^*(t) = k^*(0) e^{\frac{-3}{2}\sigma t} \tag{1.17}$$

From equations 1.14 and 1.16 the non-dimensional wavenumber as a fuction of time is found by $k^* = 2\pi h_0/\lambda$, given in equation 1.17. The growth rate is now a function of the time dependent jet radius ($h_0(t)$) and the time dependent wavenumber which is given as,

$$\omega^2 = -\frac{1}{2} \frac{\gamma}{\rho h_0(t)^3} \left[(k(t) h_0(t))^2 - (k(t) h_0(t))^4 \right], \tag{1.18}$$

with $h_0(t=0)$ and $k(t=0)$ as the initial conditions. Scaling the growth rate by the capillary time scale at time (t = 0) and substituting $k^* = k h_0$ in equation 1.18, the non-dimensionalized growth rate is given as,

$$\omega_i^* = \frac{\omega_i}{\sqrt{\gamma/(\rho h_0(0)^3)}} = \frac{1}{2} \sqrt{k^{*2} - k^{*4}} \tag{1.19}$$

In straight jets for $k^* > 1$ the perturbations are always stable but for a thinning jet with an initial condition of $k^*(0) > 1$ it is not the case. As the k^* decreases over time and becomes less than 1, the initially stable perturbations can become unstable. Figure 1.10 shows the capillary growth rate of a stretching jet ($\sigma = 0.2$) with different initial conditions of k^*. It can be seen from the figure that for $k^*(0) = 1.2$ the perturbations are initially stable but they become unstable later due to wavelength stretching.

Now consider the small perturbation $\tilde{h}$ growing on a stretching jet. If $\epsilon(t)$ is the real part of $\tilde{h}$, for a small change in time (Δt) the change in $\epsilon(t)$ is given as follows,

$$\epsilon(t + \Delta t) = [h_0(t) + \epsilon(t)] e^{\frac{-\sigma}{2}\Delta t} - h_0(t) e^{\frac{-\sigma}{2}\Delta t} + \omega_i \epsilon(t) \Delta t, \tag{1.20}$$

taking the limit $\Delta t \to 0$ in equation 1.20, ϵ takes the form of,

$$\frac{d}{dt} ln(\epsilon) = \frac{-\sigma}{2} + \omega_i. \tag{1.21}$$

Integrating the above equation gives,

$$\epsilon(t) = \epsilon(0) e^{\frac{-\sigma}{2} t} e^{\omega_i t} \tag{1.22}$$

This analysis is similar to the one presented in Tomotika [42]. The perturbation grows exponentially over time due to the growth rate term $e^{\omega_i t}$ and the stretching term $e^{\frac{-\sigma}{2} t}$ dampens the exponential growth rate. This brings in another time scale $t_\sigma = 1/\sigma$ which is related to the strain rate of the jet. A new dimensional

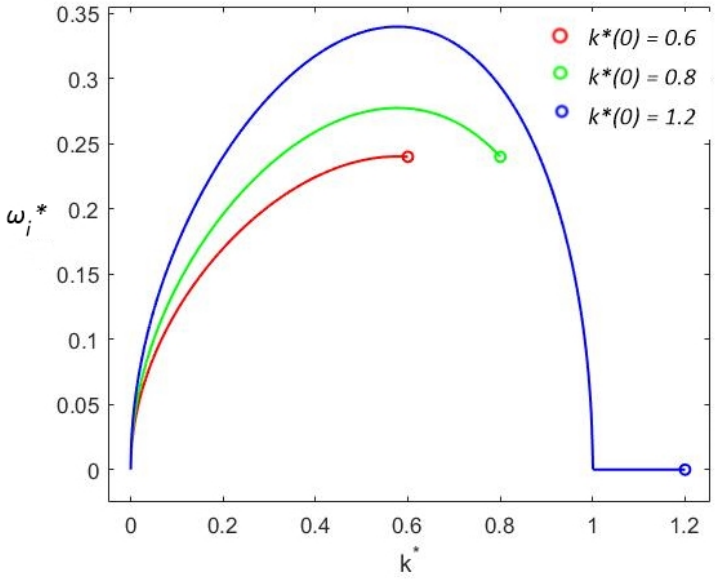

Figure 1.10: Non-dimensional growth rate plotted against the non-dimensional wavenumber for different initial conditions of k^*. The circles in the figure indicate the time instance t = 0; as time increases the k^* decreases. For all three initial conditions $\sigma = 10$.

number (T) can be defined as the ratio of square of t_σ to square of capillary time scale. This dimensionless number was first introduced by Frankel and Weihs [13].

$$T = \frac{t_\sigma^2}{t_c^2} \tag{1.23}$$

$$= \frac{\gamma}{\rho h_0^3 \sigma^2} \tag{1.24}$$

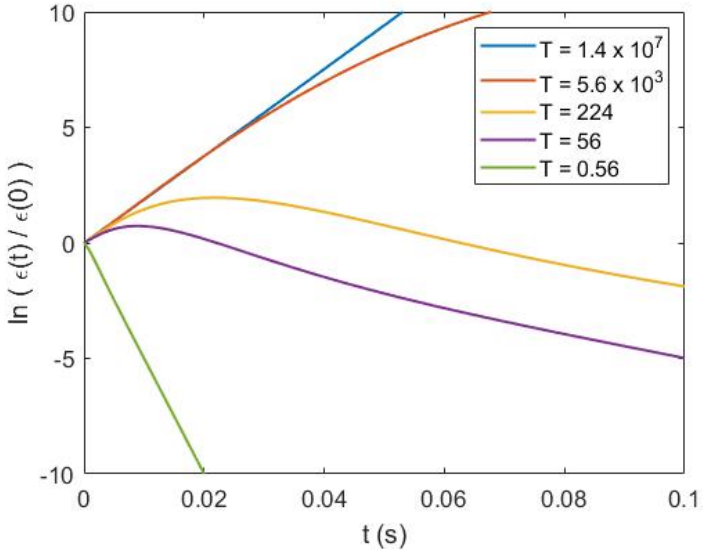

Figure 1.11: Evolution of perturbations for a water jet. The initial conditions are $h_0(0) = 0.5$ mm, $\epsilon(t = 0) = 0.01 \times h_0(0)$ and $k^*(0) = 0.7$.

For the case of T $\rightarrow \infty$ ($\sigma = 0$) the growth rate becomes independent of time which is same as the straight jet case. When T is finite, the growth of perturbations is dependent on time due to the time dependent damping

resulting from the stretching of the jet. The other limiting case, that is when T = 0 ($\sigma \rightarrow \infty$) the capillary waves are over-damped and do not grow in time. For a water jet with the initial conditions, $h_0(0) = 0.5$ mm, $\epsilon(t = 0) = 0.01 \times h_0(0)$ and $k^*(0) = 0.7$, the evolution of perturbation for different values of strain rate is shown in the figure 1.11. For a strain rate of $\sigma = 10$ (T = 5600), figure 1.12 shows the temporal evolution of the perturbation

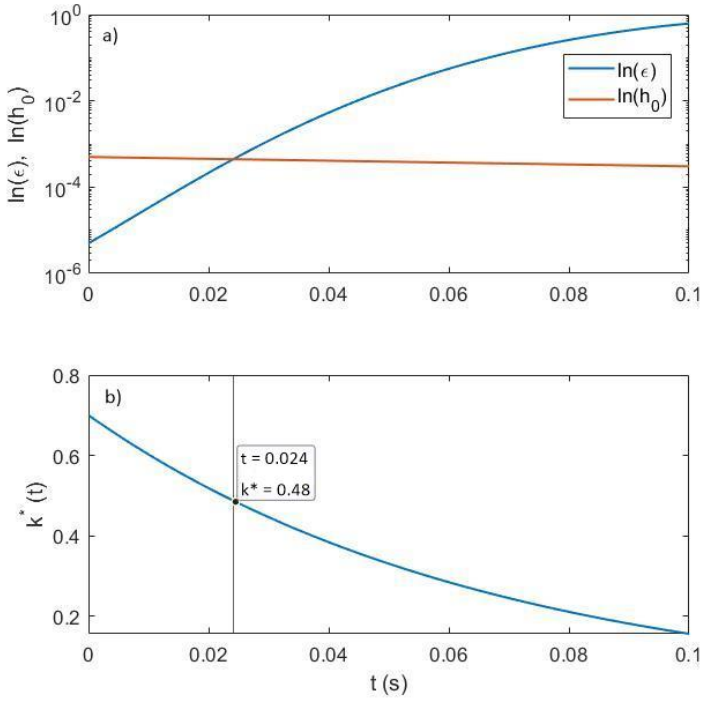

Figure 1.12: Evolution of perturbations for a water jet along with h_0 and k^*. The initial conditions are $h_0(0) = 0.5$ mm, $\epsilon(t = 0) = 0.01 \times h_0(0)$ and $k^*(0) = 0.7$. The σ is chosen to be 10 (T = 5600)

alongside the h_0 and k^*. In the figure 1.12 a, the point where $ln(\epsilon(t))$ and $\ln(h_0(t))$ meet corresponds to the time t = 0.024. This is the time instant the perturbations become as large as the local jet radius and the break-up occurs. The corresponding non-dimensional wavenumber at the same time instant is found from the figure 1.12 b, indicated by the vertical line. The k^* has reduced from 0.7 at the nozzle to 0.48 near break-up. Therefore, even when the damping caused by stretching is insignificant the non-dimensional wavenumber changes significantly affecting the near break-up dynamics. In this case bigger satellite drops are formed as the wavelength of the perturbation is longer near the break-up.

$$\sigma = g/u_0 \tag{1.25}$$

An example of accelerating straight jet in reality would be a free falling jet. A liquid jet that falls under gravity would have a constant stretching rate given in equation 1.25, where g is the acceleration due to gravity and u_0 is the velocity. To sum up, the dimensional numbers governing the growth of capillary waves on a straight jet are We, Oh, initial non-dimensional wavenumber, initial non-dimensional perturbation amplitude, the dimensionless number T and density ratio of fluids in contact. The effect of density ratio is discussed in subsection 2.1.1.

1.2.5. Stability of spiralling jets

Liquid jets emanating from a spinning source is termed as spiralling jets. A schematic representation of spiralling jets is shown in figure 1.13. These spinning jets are found in many industrial applications including the prilling process. To solve for the capillary growth rate the base flow of the spiralling jet has to be solved. Shikhmurzaev and Sisoev [38] presents a rigorous mathematical framework for solving the base flow of the spiralling liquid jets. Three dimensionless numbers were found to govern the base flow. They are the Weber number, Froude number and Rossby number which are defined as,

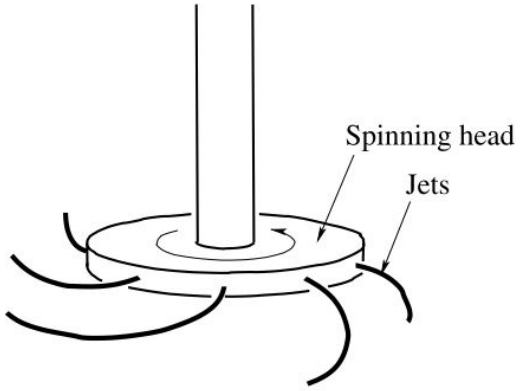

Figure 1.13: A schematic representation of spiralling jets in nano-fibre production, reproduced from Shikhmurzaev and Sisoev [38]

$$We = \frac{\rho U^2 H}{\gamma}, \quad Fr = \frac{U}{\sqrt{gL}}, \quad Rb = \frac{U}{(\Omega/2\pi)L}, \tag{1.26}$$

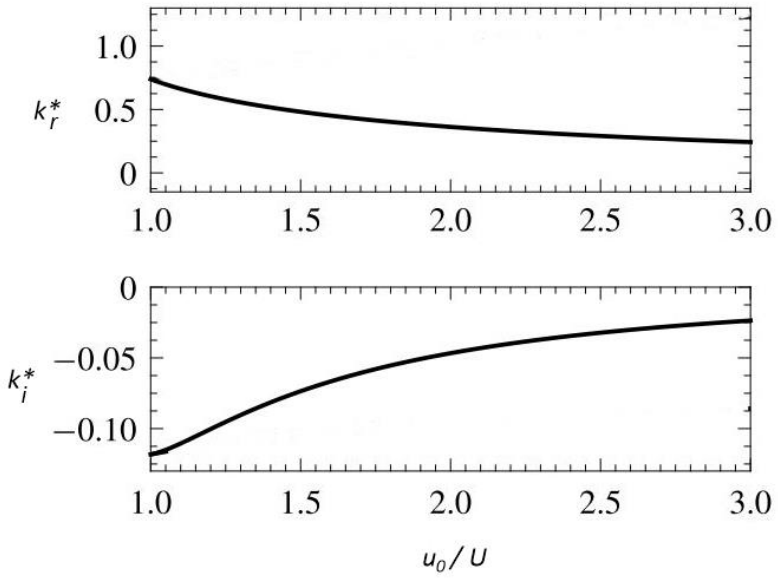

Figure 1.14: Non-dimensionalized k_r and k_i as a function of u_0/U for We = 10, reproduced from Li et al. [24]

here L is the radius of the rotating arm, H is the unperturbed radius of the jet at the nozzle, U is the velocity of the jet at the nozzle in the streamwise direction and Ω is the angular velocity in rad/s. The centrifugal forces causes the jet to accelerate in the downstream direction and the jet thinning occurs. The Coriolis and the gravity forces cause the jet to curve in the directions normal to the streamwise direction. A spatial instability analysis is performed on this base flow and the dispersion relations are obtained by Li et al. [24]. In the spatial instability analysis the wavenumber[2] ($= k_r + ik_i$) is taken as a complex quantity and the angular frequency as a real quantity. k_r^* is the non-dimensional wavenumber and k_i^* is the non-dimensional spatial growth rate. Because of the accelerating base flow in the spiralling jets one can expect wavelength stretching. Figure 1.14 shows the non-dimensionalized k_r and k_i as a function of u_0/U. It can be seen that the dimensionless wavenumber (k_r^*) decreases in the downstream direction which confirms wavelength stretching. Here u_0/U

[2]When discussing spatial instability analysis distinction is made between real and complex wavenumbers with appropriate subscripts. Whereas in temporal instability analysis the wavenumber is always real and does not have a subscript

is a proxy for the downstream direction. The quantity u_0/U increases in the downstream direction because of the accelerating base flow.

The control of break-up of spiralling jets to eliminate the satellite drops requires combining the knowledge of dispersion relation, effect of external perturbation's frequency and amplitude on merging, dimensionless number T and wavelength stretching. By understanding these phenomena one can manipulate the near break-up dynamics to eliminate satellite drops.

1.3. Literature review of straight jets

The surface tension forces on a liquid surface was first proposed by marquis de Laplace [25] and Young [46] independently in their seminal works. Savart [36] conducted a series of experiments in jet breakup but failed to identify surface tension as the driving force for the breakup. It was Plateau [30] who included surface tension into account for jet break up and applied surface energy minimization principle to predict the size of the wavelengths that would lead to breakup. This analysis leads to the definition of critical wavelength (λ_{cr}), any wavelength greater than this will be unstable and lead to breakup. $\lambda_{cr} = 2\pi h_0 \approx 6.28 h_0$ where h_0 is the unperturbed jet radius. This theory, although, supports the experiments, doesn't explain the experimental value of wavelength that is observed by Savart [36], $\lambda \approx 8.76 h_0$. This discrepancy can be attributed to not accounting for flow dynamics by Plateau [30]. A more comprehensive theoretical analysis was put forth by Rayleigh [32] who proposed the linear perturbation analysis on a inviscid Navier Stokes equations which gives a dispersion relation for temporal instabilities of the jet. Of all the wavelengths that are unstable, $\lambda \approx 9.01 h_0$ was found to have the fastest growth which agrees well with the previous experiments. A more rigorous linear stability analysis was performed by Keller et al. [19] who considered the spatial instabilities in a cylindrical jet. This addresses the un-physical fluid behavior in Rayleigh's analysis. A temporal growth rate would mean that everywhere along the jet the waves are growing in time, which is not the case near the jet nozzle; the waves always have negligible growth near the nozzle. This effect can be captured by considering a spatial instability analysis where the wavenumber was considered to be complex and the frequency of perturbation to be real. Although this analysis being more thorough, Rayleigh's analysis is usually adopted for simplicity. Chandrasekhar [1] accounted for viscosity in the instability analysis and found that viscosity decreases the growth rate of the fastest growing modes. This leads to a longer break up length. But the mechanism of break-up continued to be capillary instabilities.

The linear stability analysis doesn't capture the satellite droplets observed by Savart as early as 1833, this can be attributed to linearizing the Navier-Stokes equation in all the above analyses. The satellite drops, finite jet perturbations and the near breakup dynamics are inherently non-linear processes. The effect of finite disturbances on the jet surface was considered by Yuen [47]. Before this, it was accepted that the presence of non-sinusoidal surface waves was due to presence of higher harmonics in the initial perturbation as suggested by Rayleigh [32].

Yuen [47] looking at the radius of the jet as a function of time makes it clear that the jet neck and swell has to grow at different rates making the process essentially non-linear. This study concludes with a new inference that the initial finite amplitude perturbation also affects the jet breakup. Lee [21] was the first to consider the effect of finite perturbations in detail. The model developed was a simplified version of Navier-stokes with an assumption that the axial velocity of the jet is uniform in the radial direction. It was found that the linearized version of their model agreed well with Rayleigh's temporal model and the non-linear model was able to predict the satellite drop formation quite well. The paper also gives an estimate of break up time which slightly varies with the break up time estimated by linear theory.

A more detailed description of the role of finite perturbations is given by Pimbley and Lee [29]. This paper extends the spatial instability analysis by Keller et al. [19] to include second order non-linear terms to predict the formation of satellite droplets. This theory predicts the satellite droplet separation more accurately than the previous non-linear theories. Chaudhary and Redekopp [4] present a different approach to the non-linear problem by introducing a method of strained co-ordinates with Galilean transformation. They obtain a third order solution with an initial velocity disturbance condition. They find that the satellite drops are ubiquitously present. So they introduce an additional sub-harmonics on top of the fundamental harmonic perturbation to have a desired break-up[3]. The amplitude of the fundamental and sub harmonics are of the same order and the phase difference between them is adjusted to achieve desired break-up. It was found that the magnitude of the harmonics also grow in time and because of this it was possible to eliminate satellite droplets even for long wavelengths which are not the fastest growing ones.

[3] Accorging to the authors desired break up is when each wavelength collapse into a single drop

The non-linear spatial instability analysis was only able to qualitatively predict the satellite formation; hence, solving the complete Navier-Stokes was necessary. But solving the full Navier-Stokes equation with the necessary boundary conditions is computationally very expensive. Hence, a one-dimensional approximation similar to lubrication theory by Reynolds [33] was put forth by Eggers and Dupont [11]. This one dimensional model is computationally affordable yet retains all the important non-linear aspects. This also offers the ease of incorporating more complex rheology and different base flow models.

Savart [36] was the first to conduct careful experimentation of straight jets and also developed a stroboscope technique to capture the jet in a slowed down manner as shown in Figure 1.15. Only after the experimental evidence of jet break-up was published, the theoretical analysis was proposed by Rayleigh [32].

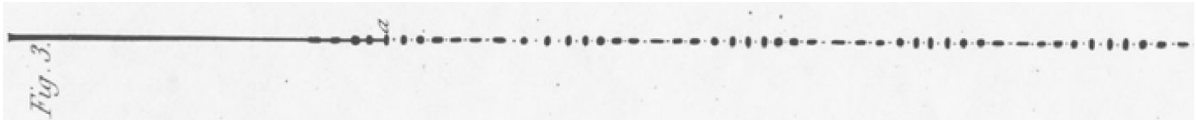

Figure 1.15: Jet break as captured by Savart [36] reproduced from [12]

Donnelly and Glaberson [7] experimentally proved the growth rate curve predicted by Rayleigh [32]. Although the theory was temporal stability analysis, the experimental data was obtained from spatial growth. In this case, because of having high speed jets, both spatial and temporal analysis happened to give the same growth rates. They also found the existence of non-sinusoidal surfaces, a non-linear phenomenon in the jet break up but accounted it to existence of higher order harmonics in the jet disturbance. After the weakly non-linear temporal instability analysis was published by Yuen [47], Goedde and Yuen [15] experimentally proved the predictions of neck and swell of the jets growing at different rates. The Figure 1.16 shows normalized neck and swell diameter with respect to time. It shows that the neck contracts at almost a constant rate whereas, the swell initially has a slow growth rate but at near break-up has rapid growth. The neck and swells growing at different rates is the reason for non-sinusoidal surfaces found earlier by [7], not the presence of higher order harmonics as suggested by the same.

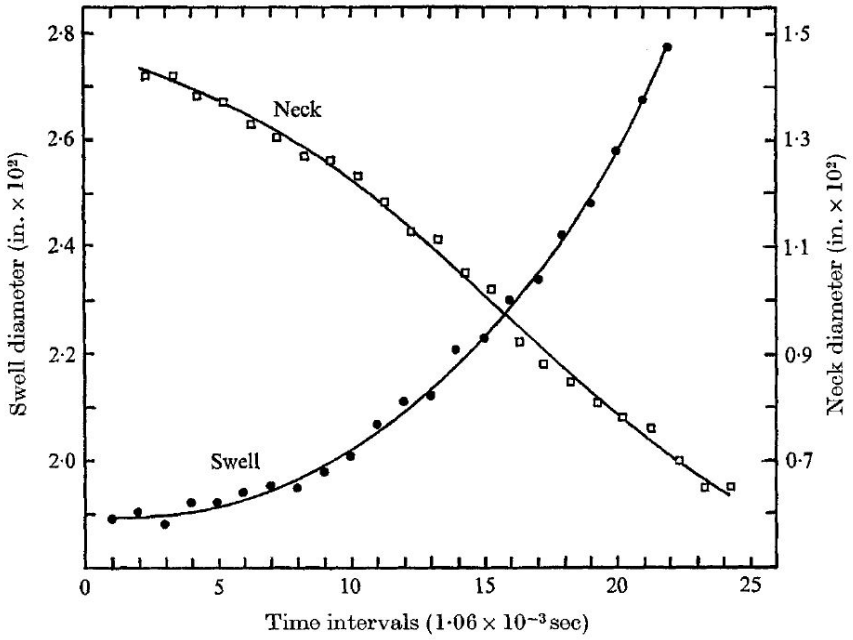

Figure 1.16: Neck and Swell diameter changing with time, reproduced from Goedde and Yuen [15]

Theoretically predicted by Yuen [47], these non-sinusoidal surfaces are the result of non-linear nature of break up process. These difference in growth rates can also explain the formation of satellite droplets and how they vary with wavenumbers. Goedde and Yuen [15] use a different imaging technique which enables them to get a real time sequence of images unlike the strobed images by Savart [36] and Donnelly and Glaberson [7]. This enables them to track a one wavelength in time and discuss the implications of non-sinusoidal

surfaces. Figure 1.5 shows the trace of the jet break up corresponding to a reduced wavenumber of 0.43. Initially, the neck contracts faster than the crests swelling as shown in Figure 1.16. Whereas near breakup the scenario reverses, the neck contracts slowly than the crests swelling. This leads to the point of detachment between the 'neck end' and the 'swell beginning' as depicted in Figure 1.5 (6) (near z = 2). They validate the linear growth rate theory by calculating the average growth rate of neck and swell. This paper claims that the downstream of the ligament is always the pinch off point as it has more time to contract than the upstream of the ligament. This claim will be more refined in later experimental evidence, which is attributed to the amplitude of the disturbance influencing the break-up.

Pimbley and Lee [29] who gave the spatial instability analysis with higher order terms also did experiments to validate their claim. They carefully considered the effect of finite disturbances and the effect of its amplitude. Equation 1.27 gives the relationship between the velocity perturbation and the break-up time[4] derived by Lee [21]. Pimbley and Lee [29] uses the break-up time of jet (equation 1.27) for a given amplitude of velocity perturbation to make sure that the experiment is operated in the linear regime. Figure 1.17 shows the logarithmic relation between break-up time and the amplitude of velocity perturbation. After establishing that they operate in the linear regime, the author's focus is on satellite drop formation and merging phenomena. A new term "infinite satellite" condition is defined, meaning the satellite droplets formed in the jet does not merge with the main drops. This infinite satellite condition was observed ubiquitously; doesn't depend on the method of perturbation, frequency of perturbation or the viscosity, but only on amplitude of perturbation. It was found that the merging of satellite with the main drops or the lack of it (infinity condition), is a function of the amplitude of perturbation. An empirical relation between the break-up time for infinite satellite condition and wavelength over diameter was found as shown in equation 1.28. Where λ is the wavelength of perturbation and h_0 is the jet radius.

$$t_b = -\frac{1}{\gamma_0} ln\left(\frac{\pi\Delta v}{2\lambda\gamma_0}\right) \tag{1.27}$$

$$t_{b\infty} = 76e^{0.28\lambda/2h_0} \tag{1.28}$$

Note: By comparing equation 1.27 and 1.28 and equating $t_{b\infty} = t_b$ the amplitude of velocity perturbation corresponding to the infinite condition can be obtained as,

$$\Delta v = \frac{2\lambda\gamma_0}{\pi} e^{-76\gamma_0 e^{0.28\lambda/d}} \tag{1.29}$$

Comparing this Δv with Figure 1.17 the required current input to the perturbing device for infinite condition can be determined.

The different merging conditions plotted against the break-up time is shown in figure 1.18. Here the break-up time t_b is used as a proxy for the amplitude of perturbation. When the break-up time is large (low perturbation amplitudes) rear merging is seen. As the break-up time reduces satellite condition and forward merging occurs.

Following this Chaudhary and Maxworthy [3] attempted to characterize the modulator, i.e. the perturbation device which produces finite amplitude perturbation. In this study the modulator is considered as a black box and a transfer function is used to model it. It compares the break up time form the numerical analysis to the experimental analysis. When the break up time corresponding to a theoretical perturbation (ϵ) is same as the experimental break up time, then the applied voltage, which determines the experimental perturbation, should have some relation to ϵ. This relation is given by the transfer function. As an additional check for this theory the authors compare the experimentally obtained surface profile with the numerically calculated ones.

Chaudhary and Maxworthy [3] continued their experimental work in their next paper Chaudhary and Maxworthy [2] focusing on post break up scenario. In this study they confirm the results of Pimbley and Lee [29] on satellite drop formation. This paper delves deep into the control of satellite drops to achieve a uniform drop size. The forward merging, rear merging and the infinity condition reported in Pimbley and Lee [29] is acknowledged by these authors.

Instead of using the breakup length as a measure for the amplitude of perturbation, García et al. [14] perturbs the pressure in the fluid chamber which is connected to the jet. This gives a more straight forward

[4] Time spent by the jet from nozzle exit to breaking up into drops

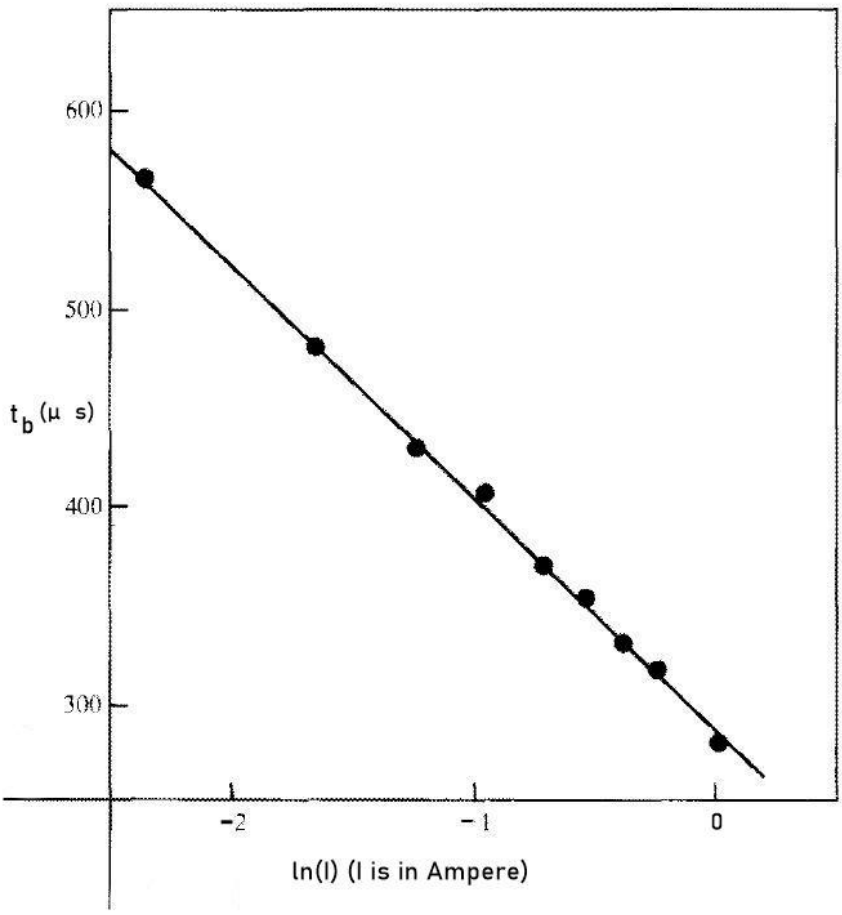

Figure 1.17: Jet break up time (t_b) plotted against electric current I applied to the piezo crystal which is an indirect measure of velocity perturbation amplitude, reproduced from Pimbley and Lee [29]

approach to determining the amplitude of fluctuations instead of having to calculate a transfer function. Figure 1.19 shows the decrease of breakup length with increase in amplitude (bottom to top). On closer look it can also be seen that there is forward separation and rear merging at low amplitudes. With increasing amplitude exactly at 7.5 Pa exists the infinity condition and later there exists rear separation and forward merging.
Additional literature of break-up regime classification for straight jet and different perturbation mechanisms used in literature are discussed in chapter 2.

Stretched jets were first considered by Tomotika [42]. The author finds that the stretching dampens the exponential growth of the perturbations on the surface of the jet. Frankel and Weihs [13] considers stretching in inertia dominated jets. Because of stretching the capillary instabilities which is an eigen value problem in straight jets becomes a initial value problem in stretched jets (see sub-section 1.2.4). The other effect of stretching is that the initially perturbed wavelength increases in the downstream direction. The damping of the capillary waves could explain why jets of honey falling under gravity do not break-up due to capillary instabilities. Viscous liquids already have a smaller growth rate and this coupled with strong stretching of the jets leads to very long intact lengths. Another example of such jets are seen in nature during volcanic eruptions. The molten lava which is a very viscous liquid is drawn into jets by wind. These jets have diameter less than 0.5 mm and are so long as 2 m. After they molten lava jets cool down it forms long fibres as shown in figure 1.20.

1.4. Literature review of spiralling jets

Wallwork et al. [44] considered the stability of inviscid spiralling liquid jets. The authors define an orthogonal co-ordinate system in a rotating frame of reference and obtain asymptotic steady state solution for the tra-

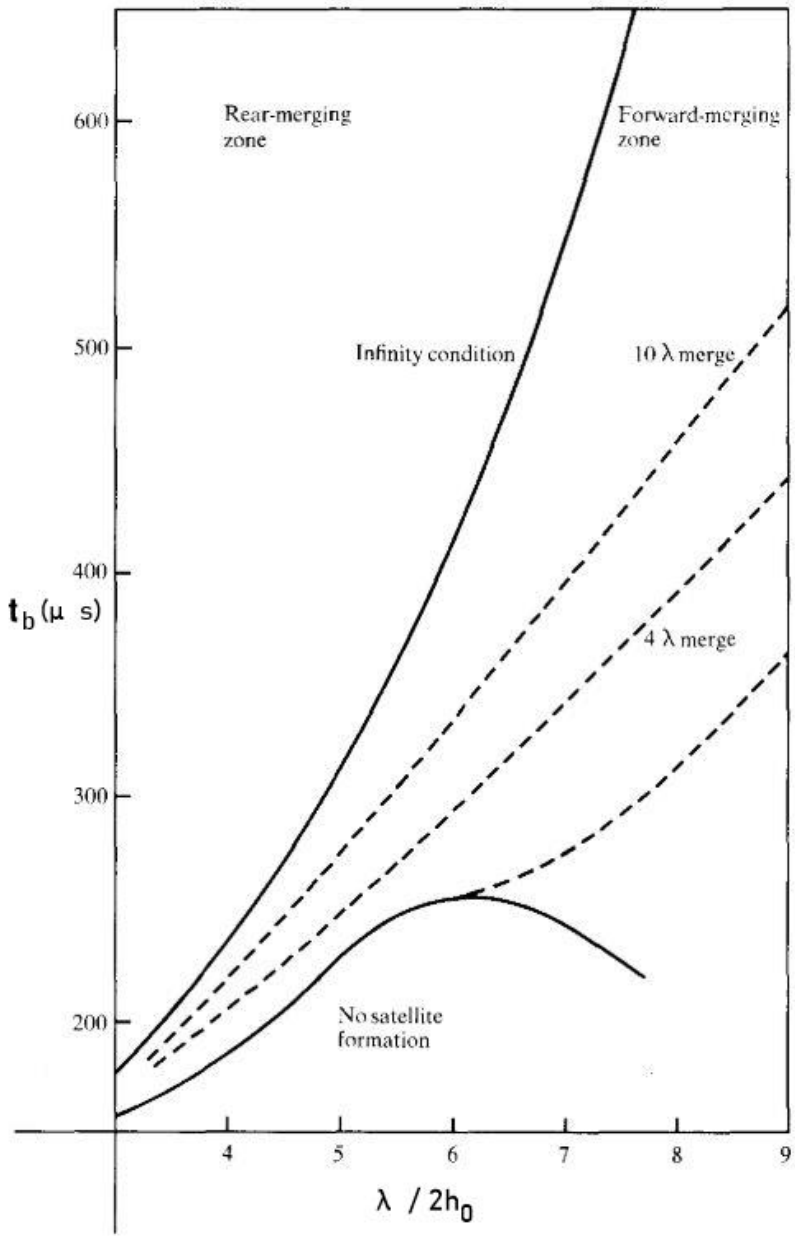

Figure 1.18: Different merging conditions plotted as a function of break-up time t_b. Reproduced from Pimbley and Lee [29]

jectory of the spiralling jet. It is shown that the jet thins in diameter as it flows further away from the orifice. A slender jet approximation using Taylor expansion is made on the base flow and is valid for Weber numbers fairly larger than 1. A linear spatial and temporal instability analysis was performed on this base flow and the growth rate relations are given; it was found that all the modes are unstable in a spatial instability analysis. A prediction for break up length is given and it agrees with reasonable accuracy with the theoretical results.

Wong et al. [45] conducted experiments on the break up of spiralling liquid jets. The authors observe four break up modes and gives a break up regime map as shown in Figure 1.21. The traces of the jet for the four modes of break up is shown in Figure 1.22. Modes 2 & 3 show formation of satellite drops and have bi-modal distribution of drop sizes. Mode 1 has no satellite drops and Mode 4 being extremely viscous causes changes to upstream jet trajectory. The difference between mode 2 and 3 is that the former has short wavelength and grows rapidly and the later has longer wavelengths. It should be noted that the spiralling jets in these experiments breakup under a random background perturbation.

Partridge et al. [28] repeated Wong's experiments on a pilot scale. They found their experimental result to

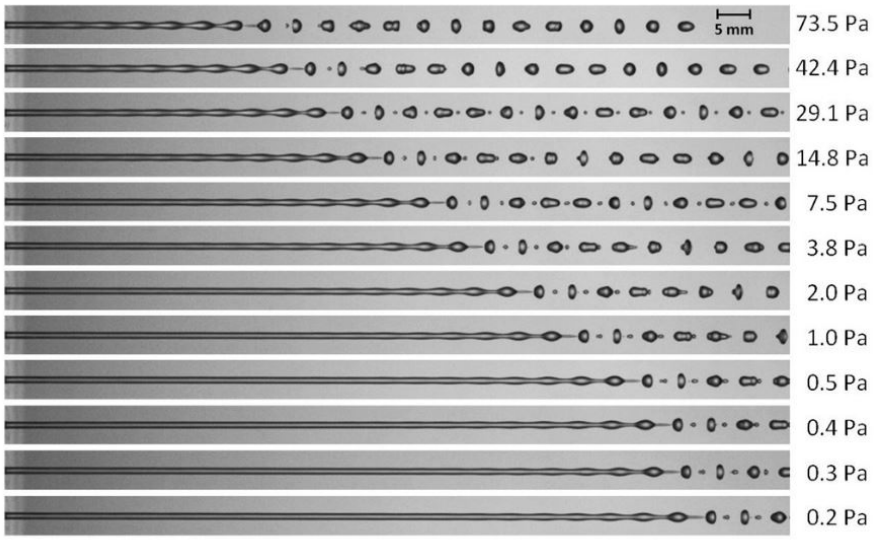

Figure 1.19: Different merging modes as a function of perturbation amplitude, with pressure fluctuations as proxy for amplitude. reproduced from García et al. [14]

Figure 1.20: Solidified molten lava jets also known as Pele's hair. Reproduced from nps.gov

be different in the following ways,

- Modes 1 and 4 were not observed and the authors attribute this to increased wind resistance and unintended vibrations in the system.
- Presence of jets in the no jet regime of Wong et al. [45], this according to the authors is due to increased centrifugal forces because of using larger diameter buckets.
- Overlapping of Mode 2 and 3 for Oh ≈ 0.02 as shown in Figure 1.23
- A difference in the way the satellite drops were created as compared to Wong et al. [45]

Both Wong et al. [45] and Partridge et al. [28] who did spiralling jet experiments only did a qualitative analysis. In the classification of break-up modes, the mode 2 is said to have short wavelengths and mode 3 is said to have long wavelengths. The observation of "short" and "long" is very qualitative and could be different for another researcher who wants to reproduce the regime map. Literature on quantitative experimental analysis of wavelengths and growth rate of capillary waves on the spiralling jets is lacking when this thesis was written.

Although it is recognized that the exit velocity plays a significant role in the break-up dynamics, the uncertainty values on the measured velocities is not given. A plot of the exit velocities comparing the lab scale and pilot scale experiments are shown in Figure 1.24. The paper also solves the slender-jet approximation of Navier-Stokes equation imposed on the steady state trajectory calculated by Wallwork et al. [44] and finds

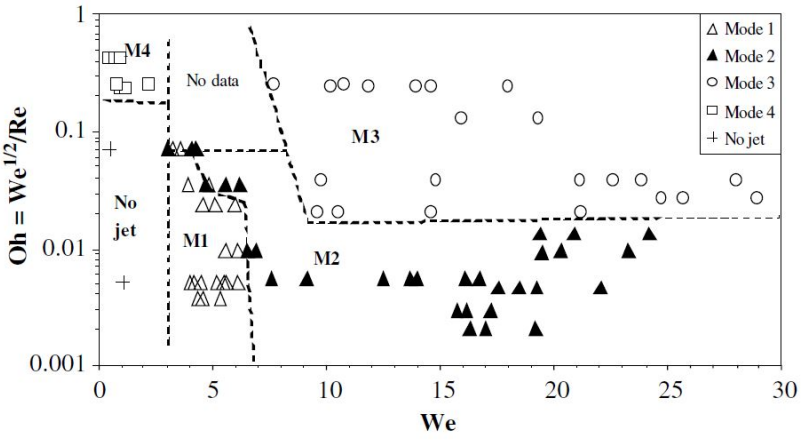

Figure 1.21: spiralling jet break-up regime map reproduced from Wong et al. [45]

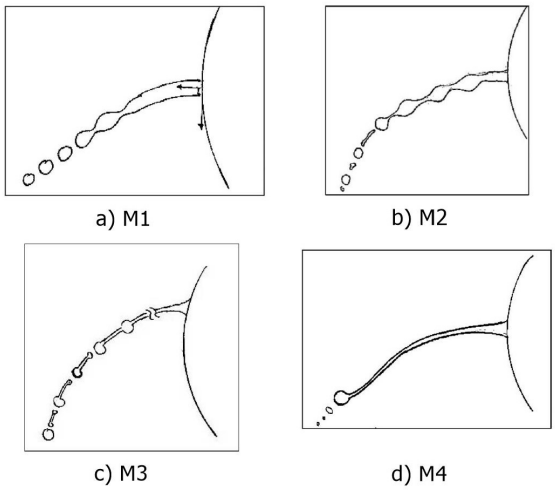

Figure 1.22: Four break-up modes of spiralling jets, reproduced from Wong et al. [45]

a qualitative agreement with the experimental results. The one observation that is unchanged between the lab-scale and pilot scale experiments is that the jet becomes more curved with increasing rotation rates.

Decent et al. [6] extends the analysis done by Wallwork et al. [44] to include viscosity and they compare their results with experiments. They find reasonably good agreement for drop size distribution for different modes of break up. Gurney et al. [17] theoretically considers forced vibrations at the nozzle of the spiralling jet; the author compares the theoretical results with the experiments of Partridge et al. [28]. In order to replicate the M1 mode theoretically, the author suggests adding a harmonic to the fundamental fastest growing frequency. Only when the amplitude of the additional frequency is 10% of the velocity of the nozzle at the jet, there exists some agreement with the experimental results. Such large disturbances may not be present in the bucket experiments since there is no active perturbation imposed on it; this could be the result of complex interactions between different frequencies too, according to the author of the paper. Finally, Gurney et al. [17] calls for the need of more precise experiments with better control over the inherent perturbations of the system.

Shikhmurzaev and Sisoev [38] finds numerous errors in the mathematical framework used by [44], [6] and several other papers published in the modeling of spiralling liquid jets. This study embarks on a rigorous mathematical approach using a local jet specific co-ordinate system. In the following paper Li et al. [24] consider the effect of finite amplitude perturbations and also describes the non-linear evolution of the perturbations near the break-up. In infinitesimally small perturbations the jet thins due to centrifugal, Coriolis and gravity forces and the fastest growing frequency does not correspond to the one at the nozzle. Whereas,

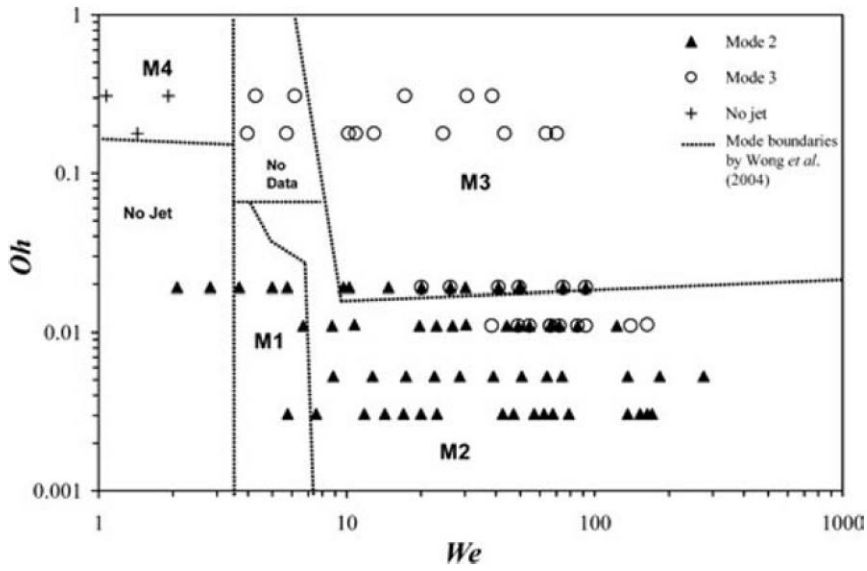

Figure 1.23: Break up modes observed in pilot scale experiments, reproduced from Partridge et al. [28]

when the ratio of radius fluctuations to the radius of the jet is more than 1% at the nozzle it was found that the fastest growing frequency corresponds to the one that is excited at the nozzle.

1.5. Highlights of literature survey

Straight jets

- The frequency and amplitude of disturbance are important in characterizing the breakup process.
- The neck and swell grows at different rates for straight jets.
- The direct relationship between the applied disturbance in the form of voltage or current and the actual velocity fluctuations at the nozzle is mostly unknown. Hence the break-up length or break-up time is used as a proxy for the same.

Spiralling jets

- Weber number, Ohnesorge number, Froude number, Rossby number, jet velocity at nozzle, amplitude of perturbation and dimensionless wavenumber are identified as important parameters affecting the breakup process.
- Existing experimental research on spiralling jets does not include external perturbations of the jet.
- Experiments on lab scale and pilot scales are in contradiction in certain modes of breakup.
- The uncertainties in the jet velocity measured in spiralling jets are not given in the literature.
- The experimental research published so far in spiralling jets is qualitative in nature.

1.6. Research objective

The main objective of this thesis is to understand the formation and merging of satellite drops in spiralling water jets under controlled perturbations. By manipulating the frequency and amplitude of the external perturbations the satellite drops can be merged with the main drops to have a uni-modal drop size distribution. This will be crucial for the design and control of the prilling process to have mono-dispersed prills. Another objective is to perform quantitative analysis on measuring the wavelength and the capillary growth rate on a spiralling jet.

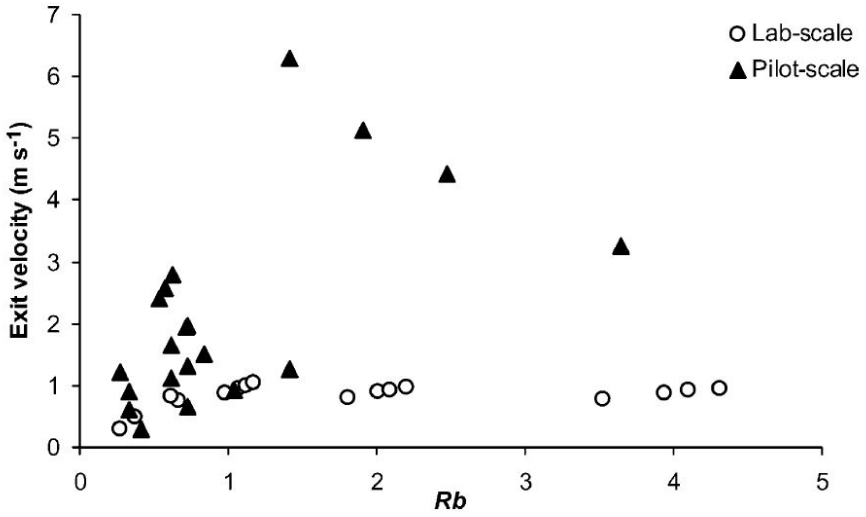

Figure 1.24: Comparison of measured velocities in lab and pilot scale experiments, reproduced from Partridge et al. [28]

1.6.1. Approach for current research

This study begins with the experiments of straight jets to understand the experimental difficulties, implementation of perturbations mechanisms and choosing the right mechanism. Chapter 2 explores these topics and identifies the perturbation mechanism that will be implemented for spiralling jets.

Bucket experiments by Wong et al. [45] are repeated along with audio perturbations to give an insight into controlling the spiralling jet break-up. Learnings from these two experiments are vital and have implicitly contributed to building a better experimental setup for spiralling jets. At the moment of undergoing this study only few experimental papers on spiralling liquid jets have been published. The authors of these papers find it difficult to compare the lab-scale and pilot scale experiments. It is also the suggestion of Gurney et al. [17] to engineer a system with minimum inherent vibrations as possible which has been attempted in this thesis. Hence the following research approach is put forth for spiralling jet experiments,

- Actively perturbing the jet should be done so that the amplitude of other vibrations in the system are relatively insignificant. Hence the external perturbation dominate the break-up process instead of random background perturbation. Because it is a rotating system, periodic high amplitude vibration might occur so the system must be well balanced. This is taken into consideration while conceptualizing the design.

- The velocity of the jet at the nozzle needs to be measured with good accuracy.

- The design should allow the calculation of capillary growth rates for a given perturbation frequency in order to validate linear theories. So far, linear theories have not been validated against the theoretical growth rate values for spiralling jets.

- Classification of modes of breakup is heavily subjective in the literature and is based on existence or lack of satellite drops and the length of unstable wavelengths. Hence, this study considers this as overlooked governing parameters in spiralling jets. Them being, the frequency and amplitude of the perturbation.

- It is hypothesized that changing the frequency of perturbation will result in different wavelengths of break-up and changing the perturbation amplitude will result in different modes of separation and merging of satellite droplets. Hence, the modes identified by the previous works are only a subset of infinitely many combinations of breakups possible.

- The goal of the study is the elimination of satellite drops which has been experimentally observed only for $We < 5$ and $Oh < 0.1$ in lab-scale experiments (refer figure 1.21). In this thesis it is hypothesised that by actively perturbing the jet, satellite drop elimination is possible for different combination of governing dimensionless numbers.

1.7. Summary

It was clear from the literature survey that the near and post breakup scenarios are dominated by non-linear dynamics. These dynamics influence the separation and merging of satellite droplets which is crucial in controlling the breakup process. Hence, introducing a finite amplitude disturbance on the jet surface whose frequency and amplitude can be changed is indispensable for precise control over the breakup process. The novelty of this study resides in the same.

2

Straight jets

2.1. Motivation & objective

Before attempting to study the breakup in spiralling liquid jets, it was vital to experimentally reproduce the breakup of a straight jet for three reasons. Firstly, to understand the perturbation mechanisms used in the literature and to get familiarized with different electronic devices such as audio amplifiers, piezoelectric crystals, piezoelectric amplifiers, etc. Secondly, coupling these devices to perturb the jets should also be investigated as there are many ways of doing this, viz. direct and indirect perturbation. Lastly, perturbed spiralling jets have not been studied in the literature before, so starting from known straight jet studies was necessary to validate the working of perturbation mechanisms. Moreover, experimental peculiarities and workarounds needs to be explored in perturbed jet experiments and starting with perturbed spiralling jets will lead to too many unknowns. Hence, it is logical to start with straight jet experiments and perform validation studies.

The objectives of the straight jet study are formulated to provide clarity on how the perturbed jets work and thereby easing the transition to experimentation in perturbed spiralling jets as smoothly as possible. The objectives are as follows:

- Defining the operating conditions in dimensionless numbers
- Identifying different perturbation mechanisms available in the literature
- Defining the steady breakup
- Performing experiments and validation of results

2.1.1. Operating conditions

Newtonian liquid jets emanating from a nozzle eventually undergo breakup . Although, the breakup mechanism depends on the parameter space (Flow rate, Nozzle geometry, ratio of viscosity of the fluids in contact, We, Re and Fr) as compiled by Leroux et al. [23]. The paper compiles five (A, B, C, D, & E) different breakup mechanism as a function of velocity at the nozzle and the breakup length (L_{BU}) i.e the unbroken length of the jet, as shown in figure 2.1.

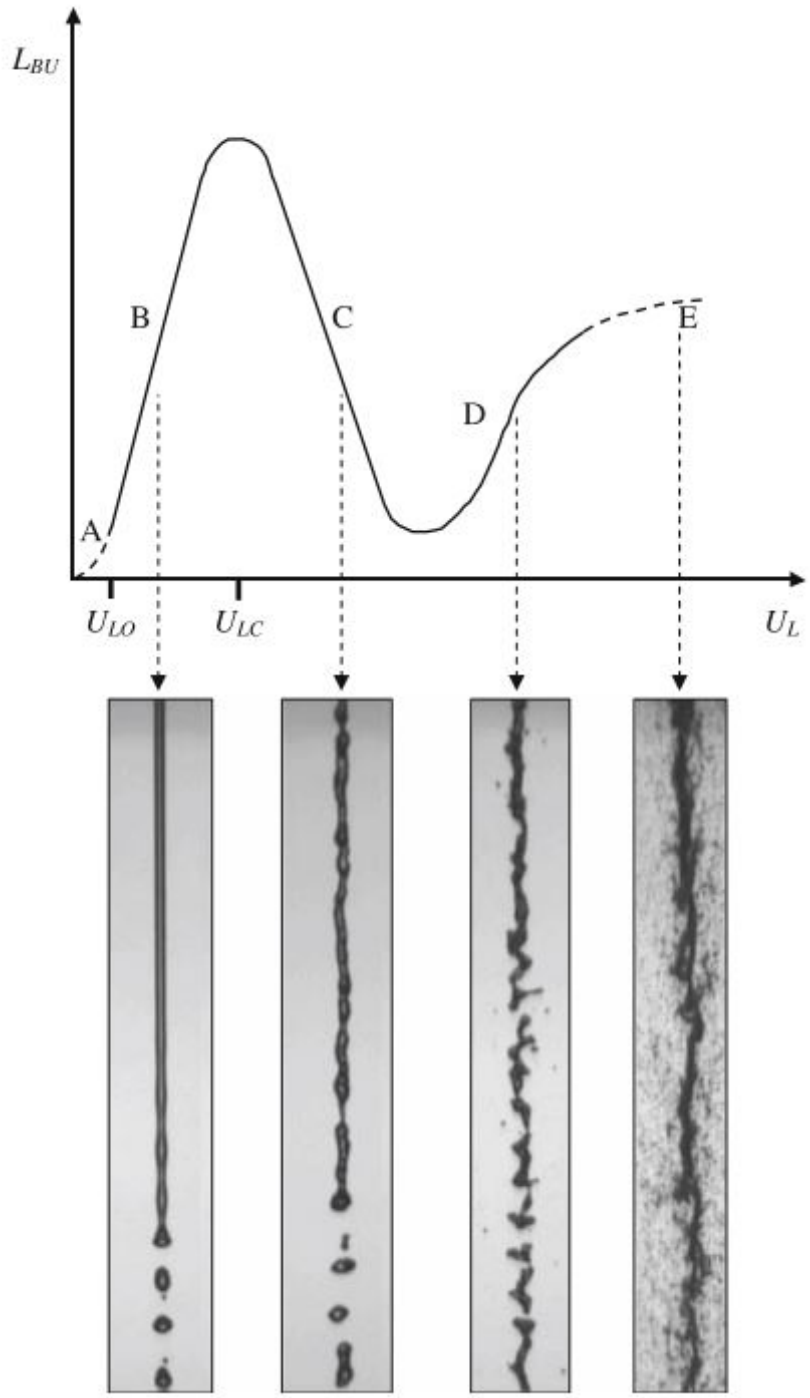

Figure 2.1: Breakup mechanism regime map reproduced from Leroux et al. [23]. The map identifies 5 breakup regimes of straight jet based on breakup length and velocity of the jet.

The Regime A, *the jet formability,* is studied in detail by Leib and Goldstein [22]. This regime pertains to the formability of the jet i.e. the fluid column is in transition from the dripping to the jetting regime. When the We number is below O(1), the fluid column is in dripping regime and when We > O(1) the fluid column forms a jet. This transition takes place at the critical weber number (We_{cr}), which also marks the transition of the breakup mechanism. Below the critical weber number (We_{cr}) the fluid column is *absolutely unstable* and above We_{cr}, the breakup mechanism is *convective instability* as delineated by Keller et al. [19]. The absolute instability stems from a saddle point singularity in the characteristic equation that defines the growth rate of

viscous jets. Physically, what this means is that the unstable wavelenghts travel in both upstream and downstream direction, as the inertia is not strong enough to convect the disturbances downstream. The waves that travel upstream hinders the jet formation at the nozzle influencing the formability of the jet itself, hence the name absolute instability. So the effect of surface tension continues to be the source of jet formability too.

To derive the critical Weber number, Leib and Goldstein [22] uses the viscous growth rate equations derived by Chandrasekhar [1] (Pg. 541) but applies a spatial instability analysis on them. Assuming the effects of gravity and viscosity of the air to be negligible, an inviscid jet is convectively unstable above the critical weber $We_{cr} = \pi$. As the jet becomes more viscous the growth rate of convective instability dominate the breakup mechanism causing a decrease in We_{cr} as the jet becomes more viscous. The figure 2.2 shows the dependence of We_{cr} on Re. Clanet and Lasheras [5] include the effect of gravity to this transition and also provide experimental evidence to the same.

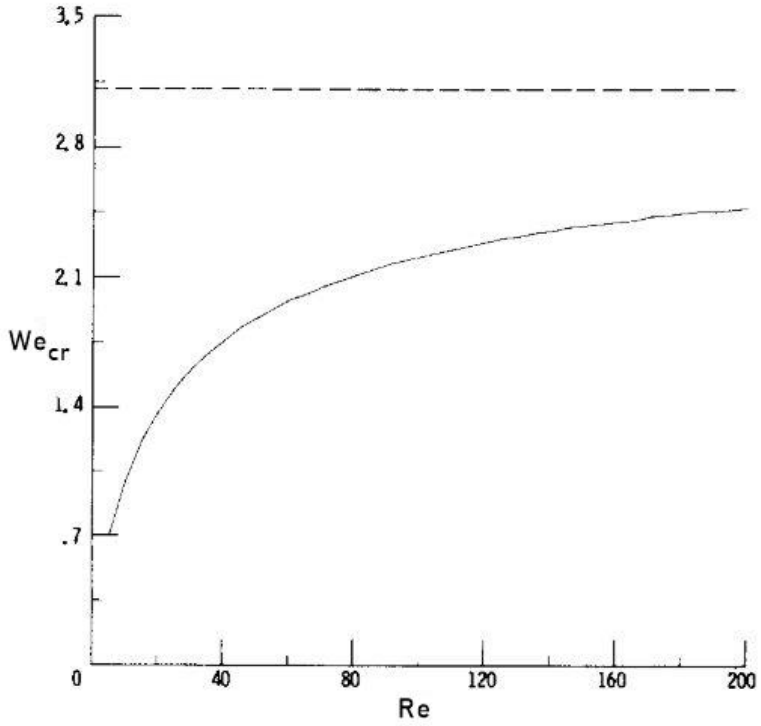

Figure 2.2: We_{cr} Vs Re, reproduced from Leib and Goldstein [22]

Regime B, *the capillary pinch off*, is the focus of this thesis. The breakup mechanism here is the convective instability, proposed by Keller et al. [19]. Although at higher We numbers the breakup is closely captured by the Rayleigh's temporal instability theory [31]. Often in literature the Rayleigh theory is used because of its mathematical simplicity. Note should be made that the jet instability is purely driven by surface tension and the fluid in contact with the jet does not contribute to the breakup.

Regime C, is *the first wind-induced breakup or the wind assisted capillary pinch off*. The capillary forces still drive the onset of instabilities but the pressure fluctuations at the interface, due to the presence of the other fluid starts to become significant.

In Regime D and E, *the second wind-induced regime and the atomization regime*, the pressure fluctuations at the interface dominate the breakup phenomena. The fastest growing wavelengths (λ_m) are much smaller resulting in extremely small droplets.

The limits of the dimensional numbers for the above regimes by different studies have been compiled by Dumouchel [8] as shown in the Table 2.1. The subscripts L and G correspond to liquid and gas phase respectively. Caution should be taken to remain with the limits of Rayleigh regime (B) for the experiments to be done in the straight jet.

Disintegration regime		Comment
Region A: dripping regime	$We_L < 8$	
Region B: Rayleigh regime	$We_L > 8$	
	$We_G < 0.4$ or $1.2 + 3.41Oh^{0.9}$	
Region C: first wind-induced regime	$1.2 + 3.41Oh^{0.9} < We_G < 13$	
Region D: second wind-induced regime	$13 < We_G < 40.3$	
Region E: atomization regime	$40.3 < We_G$	$f(T) = \frac{\sqrt{3}}{6}[1 - \exp(-10T)]$
	$\frac{\rho_G}{\rho_L} > \frac{(\sqrt{A}-1.15)}{744} f(T)^{-2}$	

Table 2.1: Limits of breakup regimes for straight jets, reproduced from Dumouchel [8]

2.1.2. Perturbation mechanisms

The perturbation mechanisms can be classified into two types based on their interaction with the jet, viz. the direct perturbation and the indirect perturbation. As the names suggest, the direct perturbation mechanism is physically coupled to jet and in the indirect method, the perturbation is caused by an indirect force on the jet. The direct perturbation mechanisms include mechanical oscillators, piezoelectric crystals, etc. Some direct perturbation mechanisms found in the literature are shown in figure 2.3. The disadvantage of using direct perturbations is that a simple correlation does not exist between the amplitude of excitation applied and the corresponding perturbation that results on the jet. For instance, Chaudhary and Maxworthy [3] assumes the direct piezoelectric perturbation to be a black box and uses a transfer function to find this correlation experimentally.

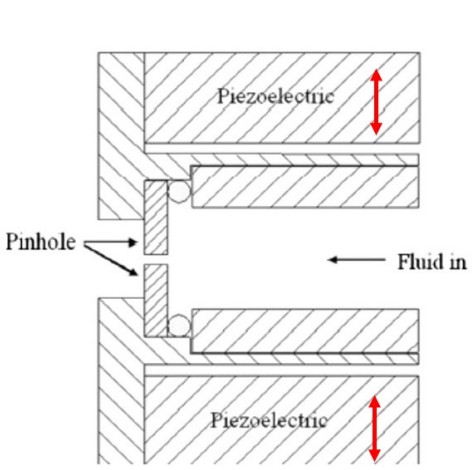

(a) Direct piezoelectric perturbation

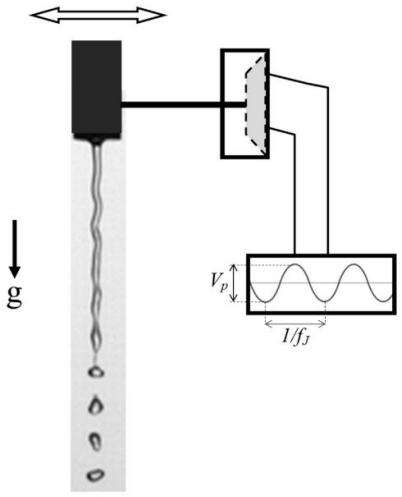

(b) Direct perturbation with mechanical oscillator

Figure 2.3: Different types of direct perturbation techniques. (a) reproduced from Rohani et al. [34] and (b) reproduced from Moallemi et al. [27]

Indirect mechanisms that are used in literature are audio speakers and electrohydrodynamic excitation (EHD). In audio perturbations the pressure waves generated by the speaker travels through air and perturbs the jet surface, here the correlation of amplitude of the sound waves and the jet perturbation amplitude is not known and depends on various factors such as speaker placement, orientation, loudness etc. The EHD induces electric charges on the surface of the jet by placing a conductive ring around the jet which is supplied with alternating voltage. In case of EHD excitation there exists an explicit quadratic relation between the voltage applied to the oscillator and the resulting pressure disturbance is causes on the jet. Figure 2.4 shows the construction of an electrohydrodynamic excitation.

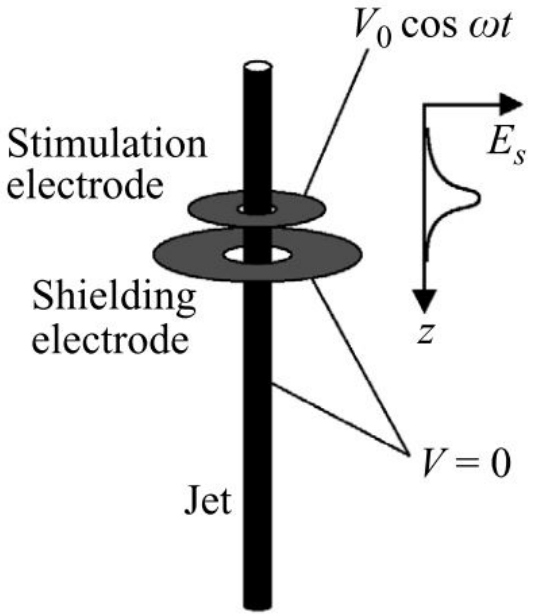

Figure 2.4: Indirect Perturbation - Electrohydrodynamic excitation, reproduced from González and García [16]

An other classification of perturbation mechanisms can be made based on the flow property which is affected by the perturbation mechanism, viz radius perturbation and velocity perturbation. The radius perturbation is achieved by squeezing the radius of the jet and velocity perturbation is achieved by vibrating the fluid in the reservoir. Although the mechanisms are affecting different flow property, they result in the same breakup mechanism, that being the capillary pinch off. This is investigated in detail by [27]. Figure 2.5 shows how these different types of perturbations can be achieved.

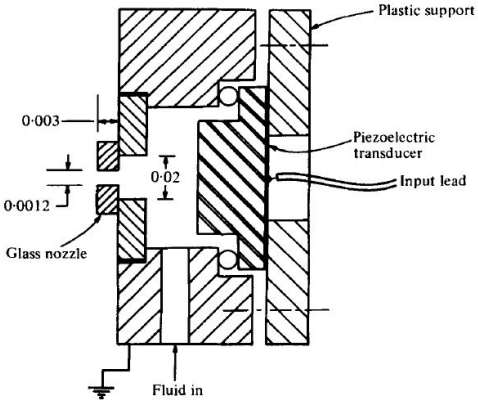

(a) Piezoelectric velocity perturbation

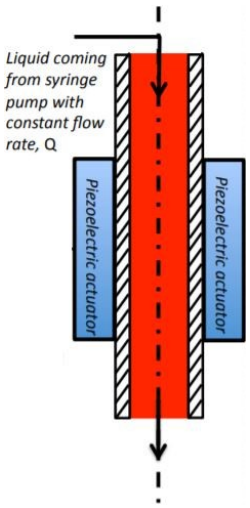

(b) Piezoelectric radius

Figure 2.5: Perturbation of different flow properties.
(a) reproduced from Chaudhary and Maxworthy [3] and (b) reproduced from Keshavarz and McKinley [20]

2.1.3. Steady breakup

As the jet is perturbed it is necessary to make sure that the perturbation applied is such that the amplitude of perturbation is larger than the amplitude of the background noise. Issues such as improper coupling of the

piezoelectric crystal to the nozzle, not having sufficient amplitude of pressure waves when using a speaker, etc can result in the jet not responding to the external perturbation but breaking up under background noise. This again speaks to the unclear connection between amplitude of perturbation produced by the perturbation device and its resulting perturbation in velocity or the radius of the jet as discussed in sub-section 2.1.2. This relation can be expressed by the transfer function f given in equation 2.1. f gives the relation between the actuation signal (current or voltage to piezo crystal) and the resulting amplitude of radius perturbation. The transfer function is device specific and has to be found experimentally, except when using EHD type perturbation devices.

$$(\delta R_{jet}) \; or \; (\delta V_{jet}) = f\big(\text{actuation signal}\big) \tag{2.1}$$

Finding the transfer function is a tedious process and involves post-processing of the results and meticulous experiments (refer [3]), hence it is useful to come up with a simple strategy to make sure that the jet is breaking up as per the applied perturbation, this calls for the definition of 'steady breakup'. A steady breakup is when the reciprocal of the time period between the breakup of two consecutive drops is same as the frequency of perturbation and remains constant for the duration of applied external perturbation. This is mathematically expressed in equation 2.2

$$f_{pert} = 1/T_{(consecutive\ breakup)} \qquad \text{(constant over time)} \tag{2.2}$$

Although this condition for steady breakup seems straight forward, it poses a challenge to experimental investigation for large number of drops. So it is proposed to use the strobe technique to validate steady breakup. When the high-speed camera's acquisition rate is set to match the perturbation frequency the camera acts as a strobe and outputs a still image over time. If the condition given in 2.2 is not satisfied the output images from the strobing camera don't remain the same. It should be noted that this is only a preliminary test to validate steady breakup, as mentioned earlier more rigorous post-processing of data is necessary. Strobed camera images from this study are shown in the figure 2.6. It can be seen that the breakup length and breakup process remains almost similar in all the images.

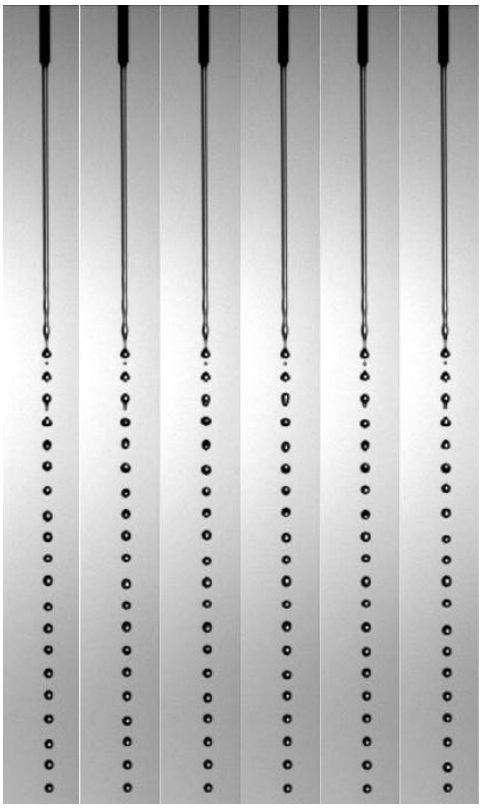

Figure 2.6: Strobe images - Steady breakup
$f_{pert} = f_{acquisition} = 2600Hz$

2.2. Experimental setup

As one of the objectives was to try out different perturbation mechanisms, different devices were fashioned out of readily available speaker and piezoelectric crystals. This was done as a preliminary test to understand different perturbation mechanisms and to analyse cases of steady breakup. Some of the makeshift prototypes that were built earlier in the research are shown in figure 2.7. Sub-figure (a) shows a jet nozzle attached to the voice coil of a speaker, in this way the jet mean velocity is perturbed [27]. Sub-figure (b) shows a pointed tip barely touching the jet, the other end of the pointed tip is attached to the voice coil of a speaker [7]. Sub-figure (c) shows a fluid reservoir with end plates that are fitted with 10 mm square piezo-crystals. Only prototype (a) was able to produce steady breakup. This could be because the amplitudes produced in b and c might have been of the same order of magnitude as the background random noise. Nevertheless, building these prototypes and testing them quickly gave a quick overview of what to expect from different mechanisms and also partly shed light on the transfer function defined in equation 2.1.

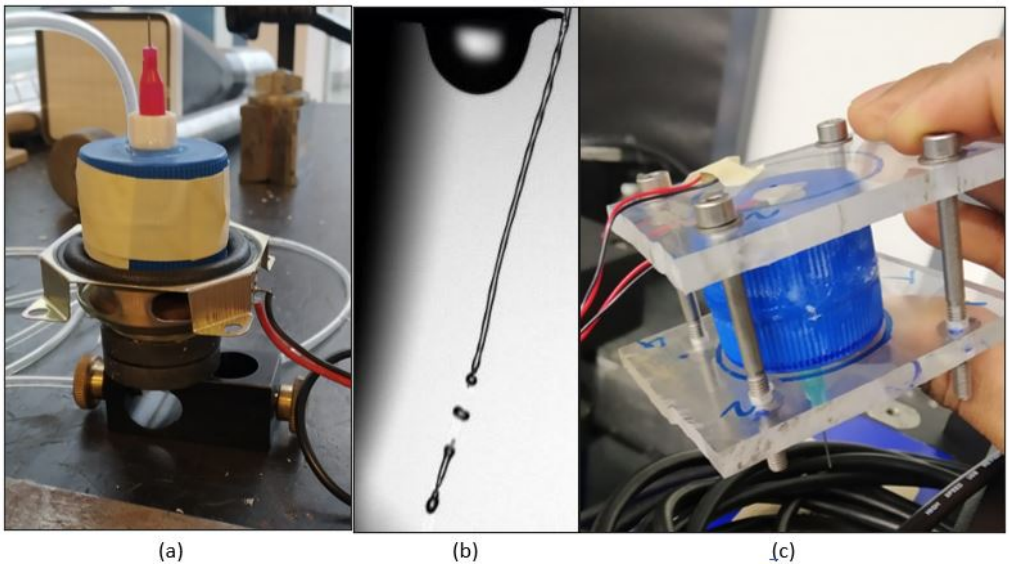

Figure 2.7: Prototypes of different perturbation mechanisms. (a) shows a jet nozzle attached to the voice coil of a speaker, in this way the jet mean velocity is perturbed similar to [27]. (b) shows a pointed tip barely touching the jet, the other end of the pointed tip is attached to the voice coil of a speaker similar to [7]. (c) shows a fluid reservoir with end plates that are fitted with 10 mm square piezo-crystals.

2.2.1. Setup description and methodology

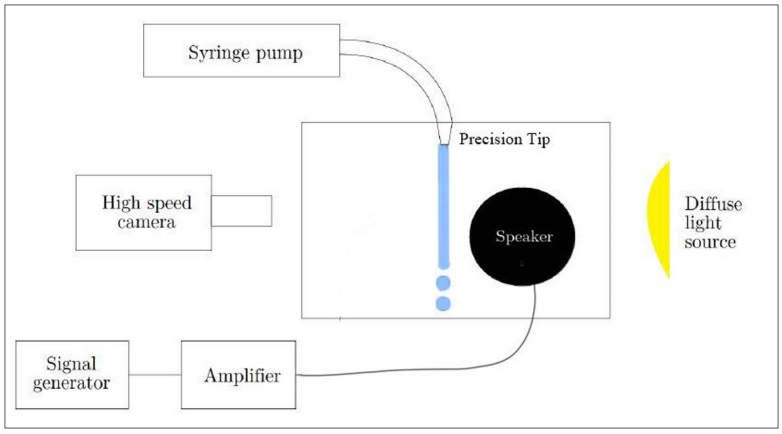

Figure 2.8: Schematic of the straight jet setup

Keeping in mind the operating range and the availability of equipment in the laboratory it was decided to use an indirectly coupled speaker perturbation. The speaker used was a BEYMA 6MI90 6.5 inch speaker rated at

Non-dimensional numbers	Range
We_L	20 > 8
We_G	0.02 < 0.4
Oh	0.006
Fr	86
Re	762
Entrance length	7.6 mm
Nozzle length	6.35 mm

Table 2.2: Parameter range of the study

250 W RMS with a frequency response of 150 - 8000 Hz and a resonant frequency of 120 Hz, refer [40] for more specifications of the speaker. The jet nozzle is placed inside a plexi-glass box and the speaker is mounted on one of the walls of the box. This box can be closed when running the experiments, but steady breakup was found when the box is left open too. General purpose precision tips of NORDSON EFD were used. Flexible tube of 2 mm inner diameter connects the precision tips to the syringe pump which controls the flow rate. The PHD2000 Series Harvard Pumps were used and the setup is placed in a climate controlled room where the temperature is maintained as constant at 22 degree Celsius. The backlight used for shadowgraphy was a 170 W LED panel and the heating can be neglected as the panel is placed outside the plexi-glass box and is switched on only for 10-15 seconds to observe the jet. Deionised water with a resistivity of 18.2 MΩ cm is used in the experiment. The experimental setup used is similar to the one used by Donnelly and Glaberson [7] and the schematic and the actual setup is shown in figure 2.8 and 2.9 respectively. The experimental parameters used in the study is given in the table 2.2. The $We_L > 8$ and the $We_G < 0.4$ to make sure that the experiments lie in the Rayleigh regime. The Fr >> 1 to make sure that the jet doesn't stretch due to gravity.

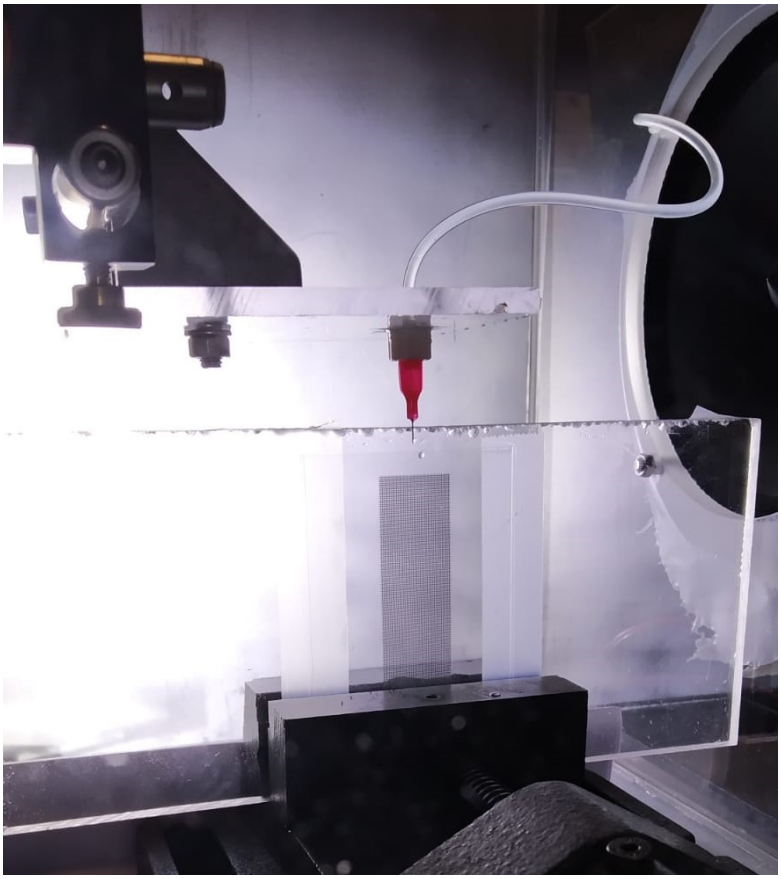

Figure 2.9: The straight jet setup

The setting up of the experiments has to be done in a meticulous way to ensure repeatability, hence the

following precautions are to be taken in order to ensure the same. The nozzle is mounted firmly to a sliding joint, so that the jet does not move when the syringe pump is switched on due to the upward reaction force on the nozzle. The connection of the sliding joint to the plexi-glass box has to be damped so that the sound frequency produced by the speaker is not affecting the source of the jet through the plexi-glass box. This might be important as the speed of the sound is far higher in the plexi-glass box than in the air, which will end up perturbing the jet source itself, this is undesirable, as the jet will be perturbed in a direct and in-direct manner simultaneously. Before starting the experiments, efforts should be made to eliminate all the air bubbles inside the tubing, syringe pump and nozzle as it can hinder the flow having a constant velocity. Faced with a choice of having to use a glass syringe or a plastic syringe the choice was made based on repeatability. The downside of the glass syringe is that it exhibits stick-slip motion between the piston and the cylinder which causes the velocity to vary in time. Due to these reasons the plastic syringe pump is used in the experiments and the images are taken only after 10 ml volume of fluid is expelled to avoid initial transient behavior in velocity if there is any. The speaker and the backlight is switched on and the image acquisition is done. The

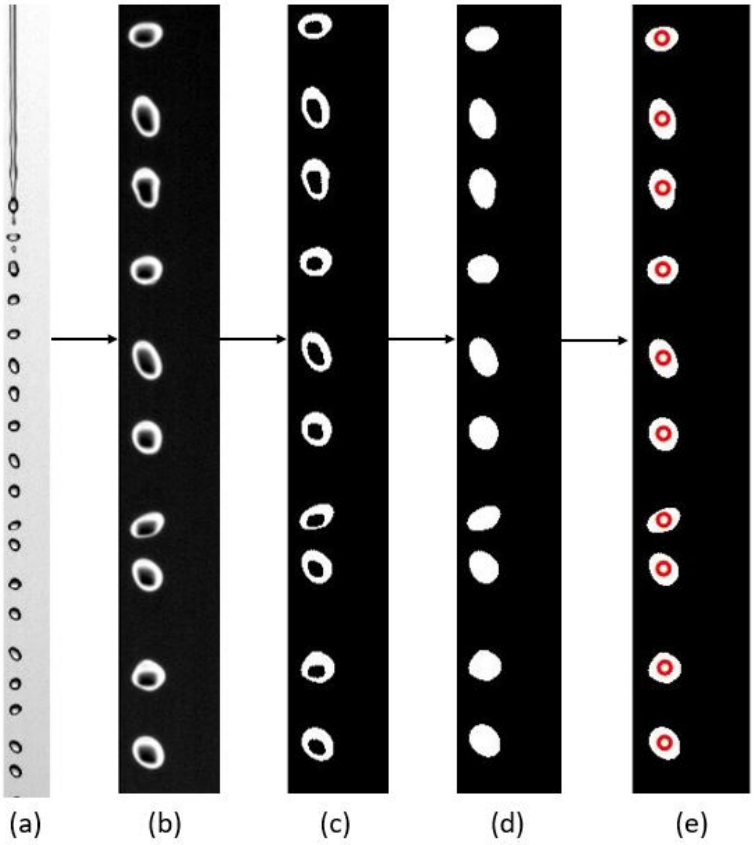

Figure 2.10: Post processing steps
a) Image of jet breakup after background subtraction b) Image is cropped and complemented to have dark background c) Image is binarized d) The black spots inside the droplets are removed e) Droplets with their centroids.

post-processing of the image data is done in the following procedure. Background subtraction is done first, following that, the part of the image that contains the drops is cropped and binarized at a given threshold. Regionprop command in MATLAB is used to find the connected regions which gives the cross section of the drop and the centroid of the drops are found. The distance between the centroid of n (>8) drops is calculated for every image (more than 100 images are used). It should be noted that the camera acquisition frequency is manually adjusted to be same as the perturbation frequency which allows the camera to act as a strobe. The average wavelength of the breakup ($\lambda_{average}$) is calculated by finding the distances between the centroid of the first and the n_{th} drop and dividing it by n-1. The step by step method of post-processing is explained in Figure 2.10. It was calculated that the change in velocity of the first and the last drop only changes by 0.3% over the imaging length due to gravitational pull, and hence ignored. Also the diffraction diameter was not subtracted as it does not affect the position of the centroid.

Note: No new equipment was bought for straight jet experiments as it was only a validation case for the study and minimum amount of time and money was spent on this.

2.2.2. Equipment uncertainties

The flowrate (Q) deliverd by the syringe pump has two errors associated with it, the random error which is 0.35% and a repeatability error of 0.05% as given by the manufacturer. These errors are considered to be independent of each other while calculating the progressive error. The inner diameter of the tip has an error of 7 μm as given by gauge standards. The velocity at the nozzle is found by the ratio of the flow rate and the nozzle cross sectional area and the associated progressive error in the velocity is calculated. Table 2.3 shows the uncertainties that arise due to different equipment used in the experiment.

Flow parameters	Value $\pm Standarddeviation$	Units
$Q_{syringe\ pump}$	7.2 ± 0.025	ml/min
$Diameter_{tip}$	200 ± 7	$\mu\ m$
$Velocity_{Nozzle}$	3.82 ± 0.25	m/s

Table 2.3: Parameter range of the study

The other equipment that is involved in the breakup process is the speaker which perturbs the jet. The error associated with the audio output of the speaker manifests in two ways, the uncertainty in the frequency of the audio and the uncertainty in the amplitude of the audio. This is investigated with the help of the microphone that is available in the smart phones. The audio acquisition in the smart phone is set to raw mode so that the audio file is not post-processed by the smartphone and this audio file is used for analysis. Figure 2.11 (a) shows the frequency response and 2.11 (b) shows the amplitude of the 3000 Hz audio file recorded. It can be seen that the 3000 Hz audio output has a frequency response of 2999 Hz having a 1 Hz error and the amplitude varies about 0.1 on the normalised amplitude scale. Both indicates that the audio produced by the speaker is subjected to errors which can affect the repeatability of the experiments.

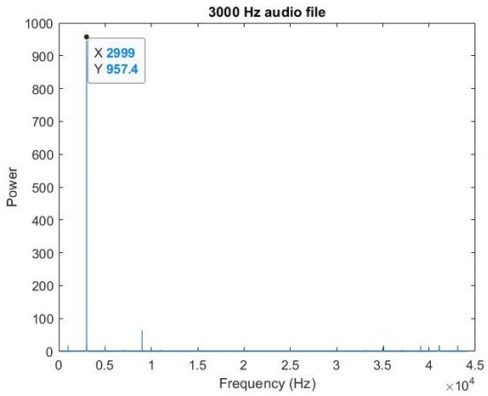

(a) Frequency response

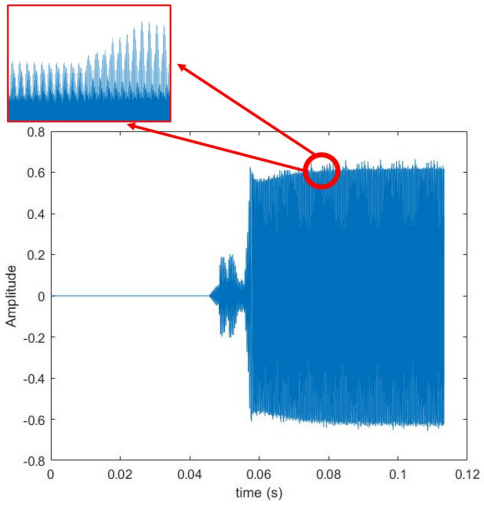

(b) Amplitude

Figure 2.11: Visualization of audio properties. (a) shows the frequency response of recorded audio signal and (b) shows the amplitude of the 3000 Hz audio file recorded

2.3. Results from straight jet experiments

A simple analysis for the validation of steady breakup is performed by comparing the jet velocity calculated from image post-processing and the nozzle velocity set by the syringe pump. The velocity of the jet is calculating by multiplying the average wavelengths of beakup with the frequency of the perturbation, given by $V_{jet} = \lambda_{average} \times f_{perturbation}$. Figure 2.12 shows the graph of velocity of nozzle against the velocity of the jet. Here, the jet velocity is plotted in red circles along with its error bar and the nozzle velocity shown in red line and error bars shown in blue dotted lines. It should be noted that several other factors may influence the

velocity at the nozzle. One hypothesis is the creeping of fluid to the outer edge of the nozzle due to surface tension resulting in a reduction in velocity also observed by Clanet and Lasheras [5]. The other hypotheses include the change in the boundary condition of the fluid leaving the nozzle, from no slip to free slip resulting in increase in velocity (refer Middleman and Gavis [26]) and cyclic oscillations present in the flow rate delivered by the syringe pump due to the way that a syringe pump works. Efforts have not been made to check the validity of these hypotheses but efforts are made to avoid them in the experiments of spiralling jets.

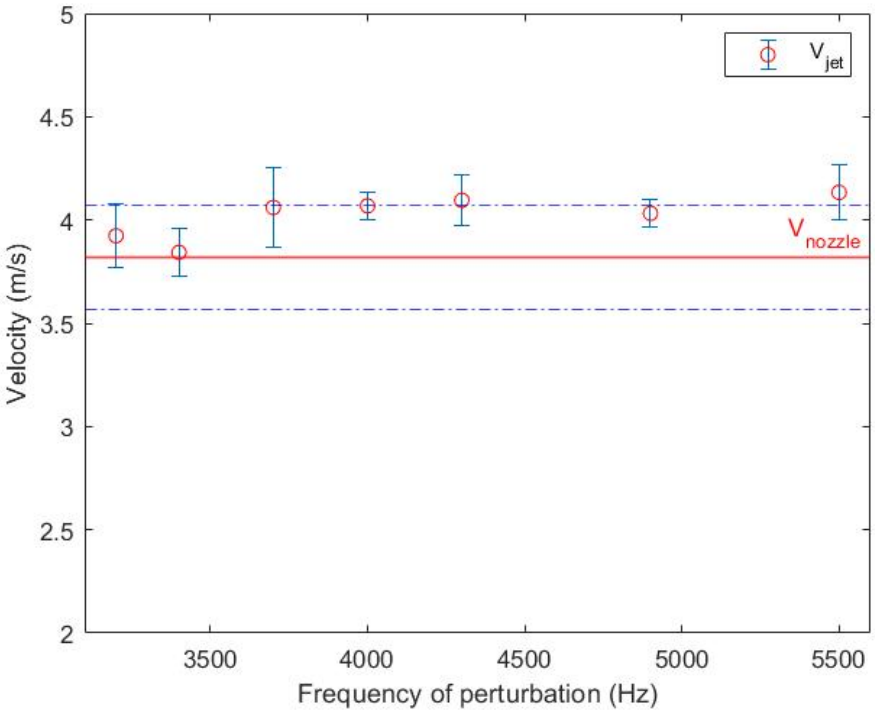

Figure 2.12: Velocity validation. We = 20, 200 μm nozzle.

2.4. Summary

As mention earlier in section 2.1, the aim of the straight jet study has been threefolds: (1) to understand the perturbation of jet, (2) to understand the coupling and limitation of perturbation mechanisms and (3) understanding the experimental peculiarities and workarounds which hasn't been delineated in the existing literature. Such useful findings from performing the straight jet experiments have been listed as follows:

- Short nozzle has to be used so that the flow is not fully developed inside the nozzle and hence do not result in an increase in velocity due to boundary relaxation,
- Hydrophobizing the nozzle will help in avoiding the creeping of the fluid to outer edge of the nozzle,
- Instead of using a syringe pump, a hydro-static pressure driven flow (gravity driven flow) has to be established to eliminate the cyclic oscillations in the flow rate,
- Audio perturbations not being very reproducible, piezo-electric perturbations can be used.

3

Spiralling jets

3.1. Motivation

The motivation of this study is employing active perturbations on spiralling water jets to eliminate satellite drops and to achieve an uni-modal distribution of drop sizes. Some prilled materials such as urea and ammonium nitrate have their molten viscosity as low as 0.005 Pa s and high surface tension, in other words a Ohnesorge number that is very close to that of the water. Hence, prilling of these fertilizers are a direct application of this study.

3.2. Objective

To achieve the final goal of mono-dispersity of drops issuing from a spiralling nozzle, a robust experimental setup has to be designed. This setup must be capable of incorporating external perturbations on the spiralling liquid. Perturbing the spiralling jet in-directly using a speaker is easy to implement, but as seen in section 2.4 audio perturbations have some inherent flaws that hinder repeatability. So it was proposed to use a piezo-crystal perturbation which is more repeatable. Implementing a direct perturbation on a spiralling jet source is not trivial. A novel experimental setup has to be engineered to do the same. This novel setup should also possess other characteristics that are necessary for precise measurement of velocity, provision for high speed shadowgraphy, ability to reproduce different dimensional numbers that govern the flow in prilling process etc. Conceptualizing this novel setup and building it is one of the main objectives. Needless to say, characterisation of the rotating bucket prilling process in terms of dimensional parameters are also in order and hence dealt with. Finally, a program (MATLAB code) to analyse the images from the high speed camera to obtain quantitative data to validate linear theory must also be developed.

3.3. Dimensional analysis

The available mathematical models in the literature given by Saleh et al. [35] and Skydanenko et al. [39] are lacking some essential physics of the problem and the dimensional analysis presented in the literature (Wong et al. [45] and Li et al. [24]) addresses only parts of the prilling process and hence do not provide a comprehensive picture. So in this study, a thorough description of the process is presented and arguments are made for the relevant dimensional numbers.

Owing to the complexity of the flow mechanics, the problem is split into two part. First part deals with the flow mechanics until the jet leaves the nozzle (jet formation) and the second part deals with the jet evolution and breakup phenomena. The geometric, material and flow parameters affecting the mechanics of the problem for both the parts is given in table 3.1. Thirteen different parameters are identified in this table. This along with three physical dimensions (mass, length, time) will result in 10 dimensionless numbers according to Buckingham PI theorem. The geometric parameters are shown in the schematic 3.1.

The dimensional analysis of the jet evolution is adopted from Li et al. [24] which describes the trajectory and the breakup process. The three dimensional numbers that govern the base flow of spiralling jet are Froude number (Fr), Rossby number (Rb) and Weber number (We). The derivations are based on the assumption that the jet is slender, i.e. the length scale in the streamwise direction is much longer than the length scale in directions normal to streamwise direction. Table 3.2 gives the dimensional numbers that govern the flow

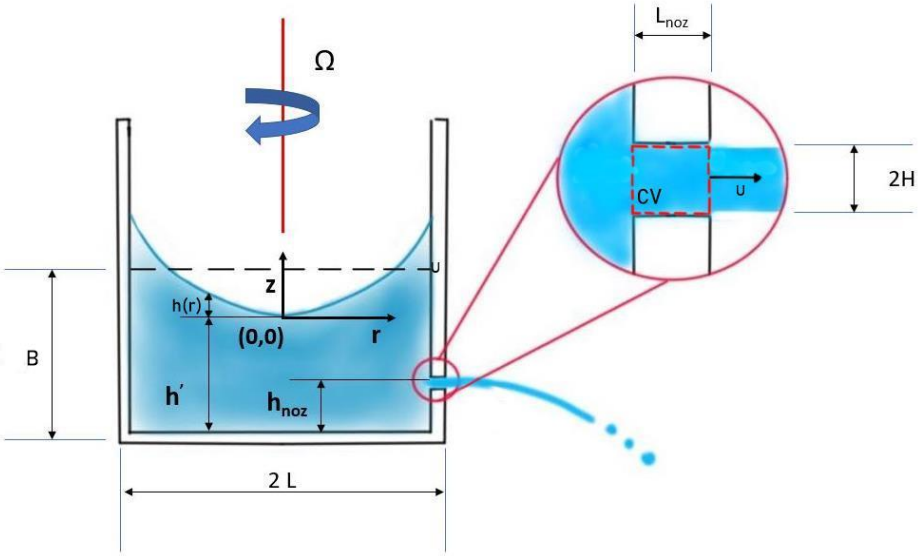

Figure 3.1: Flow dynamics in the rotating priller with a parabolic surface. Zoomed in section shows the flow of jet in the nozzle

Parameters	Symbol	Units
Velocity at nozzle exit (radial direction of bucket)	U	m/s
$Radius_{nozzle}$	H	m
$Radius_{bucket}$	L	m
$Height_{bucket}$	B	m
Rotation speed of bucket	Ω	rad/s
$Thickness_{bucket}(nozzle\ length)$	L_{noz}	m
Density of the liquid	ρ	kg/m^3
Density of the gas	ρ_g	kg/m^3
Surface tension	γ	N/m
Gravitational acceleration	g	m/s^2
Viscosity of liquid	μ	Pa s
Frequency of perturbation	f	Hz
Amplitude of velocity perturbation	δU	m/s

Table 3.1: Parameters affecting the flow

mechanics of jet evolution and breakup. Only 8 dimensional numbers are given in this table the other two are defined in the next section. It is clear from the table 3.2 that the jet velocity has to be determined precisely for characterising the jet evolution. The next section is dedicated to deriving the jet velocity and thereby identifying meaningful dimensional numbers for describing flow mechanics leading up to the nozzle. To define the dimensionless number T = t_σ^2/t_c^2, one needs to define σ. For spiralling jets, σ is defined as the ratio of centrifugal acceleration (apparent gravity experienced by the jet) to jet velocity. $\sigma = \Omega^2 L/U$. This is similar to equation 1.25 where the g is replaced by apparent gravity $\Omega^2 L$.

Dimensional Numbers	Equation
Weber number (We)	$\frac{\rho U^2 H}{\gamma}$
Rossby number (Rb)	$\frac{U}{(\Omega/2\pi)L}$
Froude number (Fr)	$\frac{U}{\sqrt{gL}}$
Ohnesorge number (Oh)	$\frac{\mu}{\sqrt{\rho\gamma H}}$
T = $\frac{t_a^2}{t_c^2}$	$\frac{\gamma U^2}{\rho H^3 L^2 \Omega^4}$
Density Ratio	$\frac{\rho_g}{\rho}$
Scaled frequency (ω_r^*)	$\frac{2\pi H f}{U}$
Scaled Amplitude of perturbation (ϵ)	$\frac{\delta U}{U}$

Table 3.2: Dimensional numbers governing jet evolution

3.3.1. Analytical prediction of jet velocity in prilling

As recognised by Partridge et al. [28] the exit velocity of the jet plays an important role in determining the dimensional parameters that govern the breakup phenomena. Hence, a mathematical model has to be proposed to quantify the exit velocity of the jet leaving the prilling bucket. A simple analytical model is derived. The problem is split into two different parts, solid body rotation of the fluid in the cylinder (priller) and the flow inside the nozzle. The two different parts are shown in figure 3.1.

The mass and momentum conservation equations for solid body rotation in a cylinder in steady state are as follows,

$$\nabla \cdot \mathbf{U} = 0 \implies \mathbf{U} = [0,\ u_\theta = \Omega r,\ 0] \tag{3.1}$$

$$-\rho \frac{u_\theta^2}{r} = -\frac{\partial p}{\partial r} \tag{3.2}$$

$$0 = \mu \frac{\partial}{\partial r}\left(\frac{1}{r}\frac{\partial}{\partial r}(r u_\theta) + \frac{\partial^2 u_\theta}{\partial z^2}\right) \tag{3.3}$$

$$0 = -\frac{\partial p}{\partial z} - \rho g \tag{3.4}$$

Integrating 3.2 & 3.4 we can get an expression for pressure field.

$$p(r,z) = \frac{1}{2}\rho\Omega^2 r^2 - \rho g z + constant \tag{3.5}$$

Assuming a small curvature at the origin O(r=0,z=0) the pressure is p_{atm} gives us,

$$p(r,z) = \frac{1}{2}\rho\Omega^2 r^2 - \rho g z + p_{atm} \tag{3.6}$$

Note that for any point under the interface z is negative. It is assumed that the nozzle is at the bottom of the tank for modeling purposes (i.e $h_{noz} = 0$). Let h' be the height of the fluid below origin (r=0,z=0) and $h(r)$ be the height of the interface from the plane z=0 in the radial direction as shown in figure 3.1.

As the volume of the fluid in the bucket is constant,

$$V = \int_{r=0}^{r=L} 2\pi r h(r) dr + \pi R^2 h' \tag{3.7}$$

From boundary conditions it can be found that,

$$h(r) = \frac{\Omega^2 r^2}{2g} \tag{3.8}$$

Substituting equation 3.8 in equation 3.7 h' is given as,

$$h' = \frac{V}{\pi L^2} - \frac{\Omega^2 L^2}{4g} \tag{3.9}$$

When h'=0, $\Omega_{critical}$ can be found as,

$$\Omega_{critical} = \sqrt{\frac{4gV}{\pi L^4}} \tag{3.10}$$

Hence, this mathematical formulation is suitable only when $\Omega \leq \Omega_{critical}$.
Going back to 3.6 and substituting for z = - (h') and r = L which is the radius of the bucket,

$$p(L,-h') = \frac{1}{2}\rho\Omega^2 L^2 + \rho g\left(\frac{V}{\pi L^2} - \frac{\Omega^2 L^2}{4g}\right) + p_{atm} \tag{3.11}$$

where, p(L,-h') is the pressure at the inlet of the nozzle.
Now following a stream line from the interface to the inlet of the nozzle, the Δp is given as,

$$\Delta p = \frac{1}{2}\rho\Omega^2 L^2 + \rho g\left(\frac{V}{\pi L^2} - \frac{\Omega^2 L^2}{4g}\right) \tag{3.12}$$

$$= \rho g\frac{V}{\pi L^2} + \frac{1}{4}\rho\Omega^2 L^2 \tag{3.13}$$

This can be converted into units of head by dividing it by ρg,

$$H_{rot} = \frac{V}{\pi L^2} + \frac{\Omega^2 L^2}{4g} \tag{3.14}$$

In the nozzle, the forces acting on the control volume (CV) (refer zoomed in section in the figure 3.1) are the centrifugal body force, hydro-static forces and the shear forces. Although a coriolis force acts on the control volume, its projection in the streamwise direction is zero. The centrifugal force inside the nozzle is given in equation 3.18.

$$F = \rho \iiint_{CV} f\,dV \tag{3.15}$$

$$\text{with,}\quad f = \nabla\left(\frac{\Omega^2 x^2}{2}\right) \tag{3.16}$$

$$\implies F = \rho A_{noz} L_{noz}(L + L_{noz}/2)\Omega^2 \tag{3.17}$$

$$\approx \rho A_{noz} L_{noz} L\Omega^2 \qquad (\because L_{noz} << L) \tag{3.18}$$

Since $L_{noz} << L$ the flow in the nozzle can be assumed to be a plug flow (with a velocity U) and the losses can be accounted for by multiplying the momentum leaving the CV by a overall loss factor (K). The force balance in the nozzle simplifies to,

$$K\left(\frac{1}{2}\rho U^2\right) = \rho L_{noz} L\Omega^2 + \rho g H_{rot} \tag{3.19}$$

$$U = \sqrt{\frac{2gH_{rot} + 2L_{noz}L\Omega^2}{K}} \tag{3.20}$$

$$U = C_d\sqrt{2gH_{rot} + 2L_{noz}L\Omega^2} \quad \text{(Where, K} = 1/C_d^2\text{)} \tag{3.21}$$

$$U = C_d\sqrt{2gH_{rot}}\sqrt{1 + \frac{L_{noz}L\Omega^2}{gH_{rot}}} \tag{3.22}$$

Here C_d is the discharge coefficient. For a typical prilling process, L_{noz} = 4 mm, L = 0.2 m, Ω = 300 rpm, H_{rot} = 0.4 m, then the ratio $\frac{L_{noz}L\Omega^2}{gH_{rot}} = 6.3 \times 10^{-3}$. Therefore the nozzle velocity can be simplified as,

$$U = C_d\sqrt{2gH_{rot}} \tag{3.23}$$

Once the jet leaves the nozzle the jet may undergo further contraction depending on whether the flow was fully developed in the nozzle (refer Middleman and Gavis [26]). Going through this rigourous process of getting the velocity at nozzle exit gives an opportunity to make an informed choice about the dimensional numbers that govern the flow mechanics leading up to the formation of jet in the prilling process. The dimensionless numbers proposed by this study is given in the table 3.3. The H_{rot} in this table can be replaced by the bucket height height B at high rotation rates for simplicity. These two dimensional numbers in combination with the other 8 already presented in the table 3.2 completes the dimensional similarity of the prilling process.

Dimensional Numbers	Equation
Coefficient of discharge	C_d
Ratio of centrifugal to hydrostatic forces	$\frac{L_{noz}L\Omega^2}{gH_{rot}}$

Table 3.3: Dimensional numbers governing jet formation, to be used along with the dimensionless numbers in table 3.2

3.4. Rotating bucket experiments

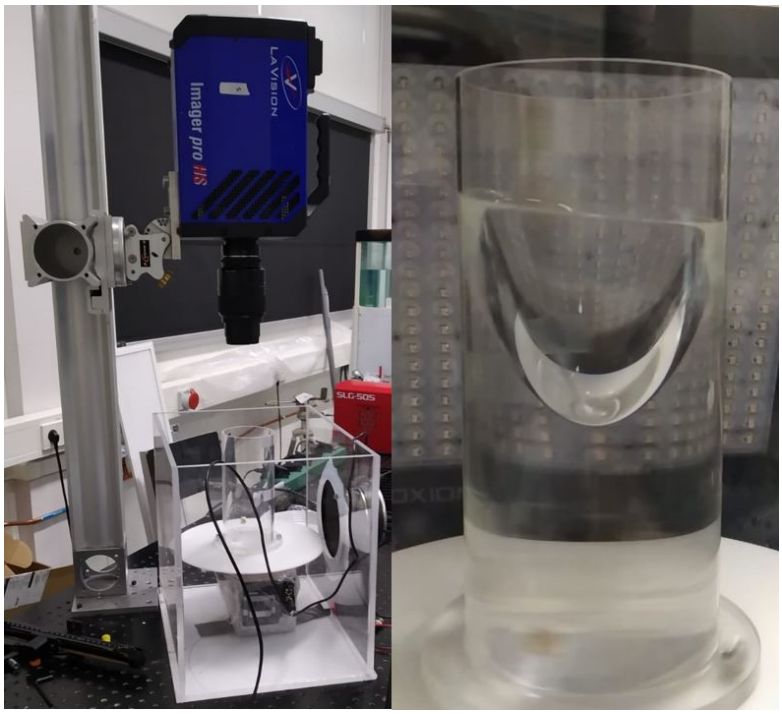

Figure 3.2: Rotating bucket experiments with and without audio perturbations.

The rotating bucket experiments similar to the prilling process has been repeated in a small scale as a preliminary study to check the hypothesis of active perturbation on spiralling jets. A lab scale setup is built for this purpose. A cylindrical bucket of inner diameter 84 cm and 20 cm height is manufactured. A nozzle of 0.4 mm is attached to the bottom of the cylinder at 2 cm height from the base. The experiment's bucket dimensions are kept as same as Wong et al. [45]. It has to be noted that this experiment does not have di-

mensional similarity to the prilling process with respect to jet formation, table 3.3. The experimental setup is shown in figure 3.2.

Wong et al. [45] uses peristaltic pump to continuously pump water into the bucket. This disturbs the free surface and may cause artificial velocity fluctuations at the nozzle. Hence in these experiments the flow is filled to a certain height and then allowed to drain for a height of 1 cm to visualise the jet. i.e. The initial spinning height of the bucket is 18 cm and by the end of the experiment it reduces to 17 cm. But this makes it difficult to determine the jet velocity in this experiment, unlike Wong et al. [45] where the fluid height is constant and is collected for a certain amount of time to calculate the jet velocity. Because of not maintaining constant bucket height accurate velocities of the jet are unknown, limiting the study only to qualitative measurements. An audio perturbation is added to the bucket experiment and a frequency sweep is done to see if the jet responds the perturbations. As this is done with a poor knowledge of the velocity of the jet, the ability to choose the fastest growing frequency is curtailed forcing a frequency sweep study. The jet seems to be breaking up uniformly around 800 Hz as shown in the figure 3.3. The experimental conditions are as follows, rotation speed 30 rad/s, height of the liquid in the bucket at zero rotation is 13 cm and the rotation height is 16.5 cm. Although this is not a quantitative study this gives us confidence to build an experimental setup where the velocities and rotation speed can be precisely controlled.

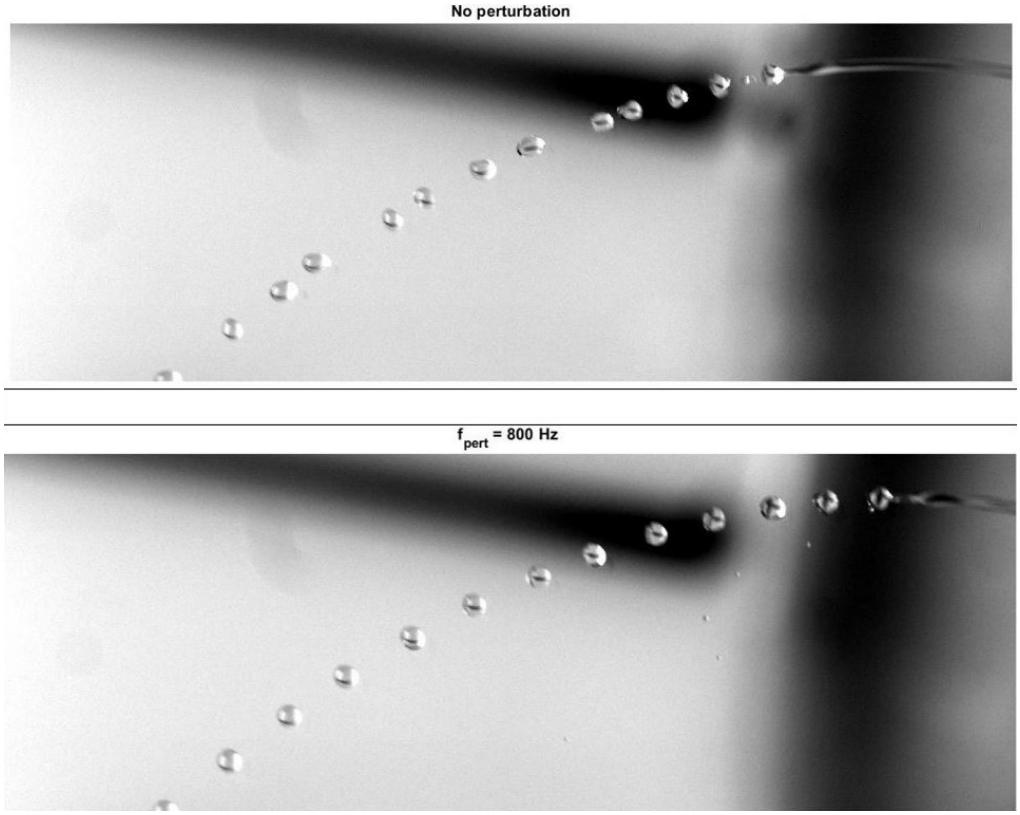

Figure 3.3: Rotating bucket experiments.

3.5. Experimental setup

Because of difficulties with measuring velocities from a spiralling source and to be able to change the dimensionless numbers in table 3.2 with ease, rethinking the design of experimental setup is crucial. Also, from figure 2.11 it is known that audio perturbations has to be replaced with piezo electric perturbations. The design is inspired from a lawn sprinkler and is shown in figure 3.4. This device has sealing mechanism and hence allows the jet to be perturbed as it is rotating. It has a very sturdy build so that the vibrations generated by the rotating parts are small. The CAD design, tolerancing, sealing, perturbation mechanism, manufacturing etc are explained in detail in Appendix A. The placement of this design in a broader sense with the ancillary devices is shown in the schematic 3.5. The different parts of this new setup are explained as follows:

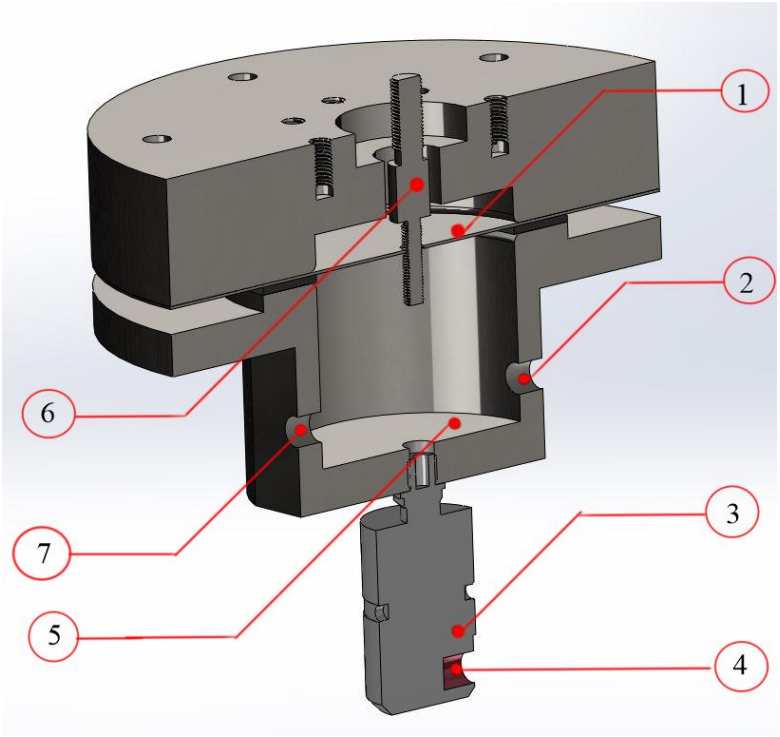

Figure 3.4: New design of experimental rig.

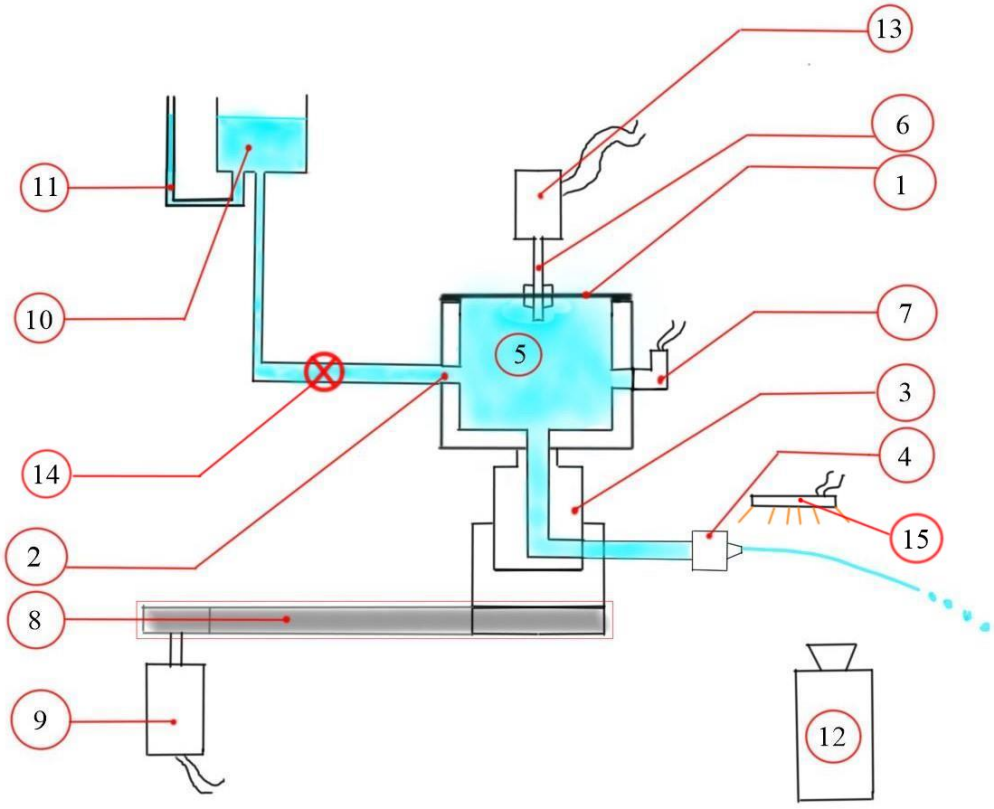

Figure 3.5: Schematic of experimental setup (Not to Scale).

- **1 - The vibrating plate**. Top surface of the fluid chamber which is connected to the piezo crystal through (6). This delivers the fluid perturbation. An eigen frequency analysis of this plate is given in

Appendix B. This is done to ensure that the plate is not in resonance condition when the perturbations are switched on.

- **2 - Fluid inlet port**. Fluid enters the fluid chamber from the gravity pump.
- **3 - Rotary Union**. This is fluid coupling that has a non rotating input and a rotating output. The rotary union is connected to a speed controlled motor. This is the heart of this new design which enables the perturbation of a rotating jet.
- **4 - Nozzle**. The nozzle is connected to the rotary union via a threaded joint. In this new setup the rotating arm length (L) and the nozzle length (L_{noz}) is the same.
- **5 - Fluid chamber**
- **6 - Connecting shaft**. The shaft that connects the piezo crystal to fluid chamber.
- **7 - Pressure port**. The pressure in the fluid chamber is measured in this port.
- **8 - Timer belt and Pulleys** A timer belt pulley system connects the rotary union to the pulley on the motor.
- **9 - Motor** A stepper motor with PID control that can deliver various rotation speeds
- **10 - Fluid reservoir** Fluid reservoir which acts as a hydro-static pump. The height at which the reservoir is placed can be adjusted to change the velocity of the jet at zero rotation speed of the motor. The temperature of the water is measured in the fluid reservoir.
- **11 - Graduated tube** This graduated tube connected in parallel with the tank is used to measure the height of the liquid in the tank precisely as it is easier to distinguish the upper and lower meniscus.
- **12 - High speed camera**
- **13 - Piezo-electric Crystal** The piezo crystal can deliver a force of 6000 N and has a resonant frequency of 25 kHz. The displacement of the shaft per oscillation can be controlled by the amplitude of the sinusoidal voltage applied to the crystal, the shaft amplitude can be adjusted between 0 - 60 μm, corresponding to a voltage input of 0 - 1000 V.
- **14 - Valve** A valve that can be opened or closed to start the jet.
- **15 - Diffuse LED Light source** The light source is rated at 25 W power.

The guidelines proposed in section 1.6.1 list various requirements for the experimental setup, which is met in the above design. The features of this new experimental setup are as follows:

- Different combinations of We and Rb can be obtained by adjusting the fluid reservoir's height (10) and the rotation speed of the motor.
- Precise calculation of velocity is possible and is done by measuring the flow rate and then dividing by nozzle area.
- Different nozzle diameters can be mounted which enables the control of Oh number to an extent.
- The jet can be perturbed by applying sinusoidal voltage to the piezo-electric crystal.

The actual setup that was built and assembled in the multi-phase experimental lab is shown in figure 3.6.

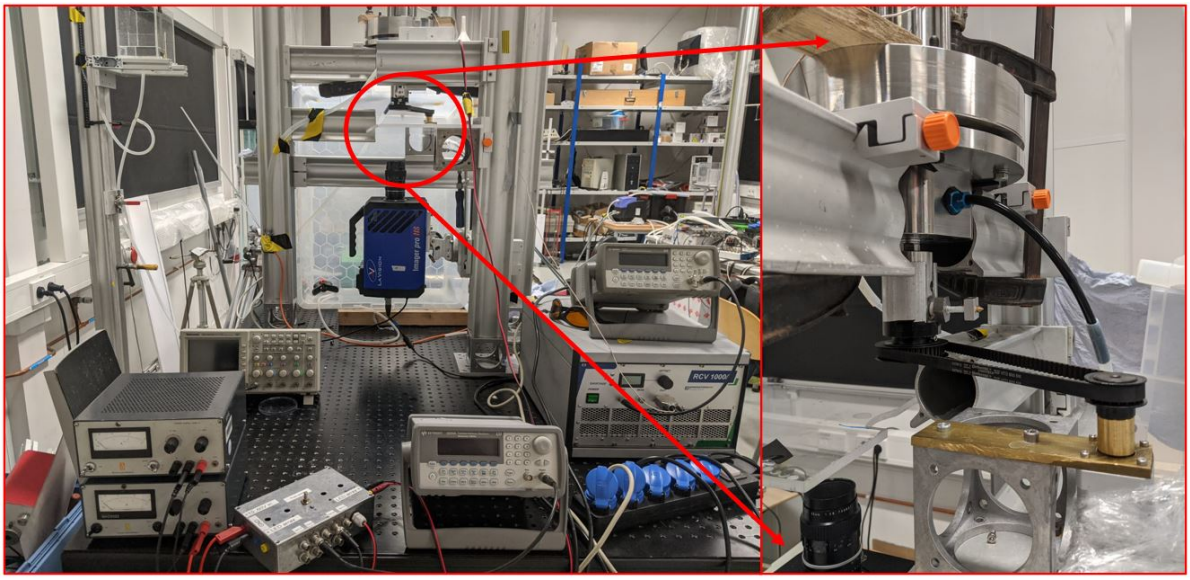

Figure 3.6: The setup along with supporting electronics.

3.5.1. Procedure for experimentation

An initial setup procedure is followed every time to ensure reproducible experiments. The procedure is as follows:

1. The system has to be void of bubbles. The bubbles could absorb the perturbations and hence result in a weaker perturbation of velocity. The procedure to render the fluid chamber (5) devoid of bubbles is explained in Appendix C.

2. The FFT of the pressure signal should give the frequency of the perturbation, this is an additional check to validate the removal of bubbles.

3. Let the height of the top surface of the water in the reservoir (10) from the nozzle be h_n. To measure the velocity of the jet, the motor is spun after opening the valve (14). The time for 1 cm ($\Delta h_n = 1cm$) of liquid to decrease in the graduated tube (11) is measured. The flow rate is found by multiplying tank area to Δh_n and then the velocity can be found by dividing this flow rate by nozzle cross sectional area. Here the assumption is that the jet does not contract after leaving the nozzle. This step is repeated and the uncertainty in nozzle velocity is determined.

4. Caution should be taken that $\Delta h_n / h_n$ is small so that the velocity at the nozzle doesn't change significantly within the measurement time. In this study $\Delta h_n / h_n = 1/17$. The error in velocity due to this type of measurement is 2.5 %.

5. Calibration of the target should be carried out.

3.6. Post processing

Apart from just visualising the jet, there needs to be quantitative information extracted from the images. Experimental studies in the literature have not measured any quantitative information from spiralling jet experiments. Hence a MATLAB program was written to perform a quantitative analysis of jet breakup. The two most common validation of instability analysis is the wavelength of the unstable wave and the growth rate of the same. Attempts have been made to measure both of them. This section will explain the novel post-processing code and address the challenges and limitations of the code. The matlab code is given in Appendix F.

A sample of input images to the code is shown in figure 3.7. These images undergo a series of pre-processing such as background subtraction, binarization and median filtering so that they are suitable for quantitative analysis. Such pre-processed images are shown in figure 3.8. In this figure temporal evolution of

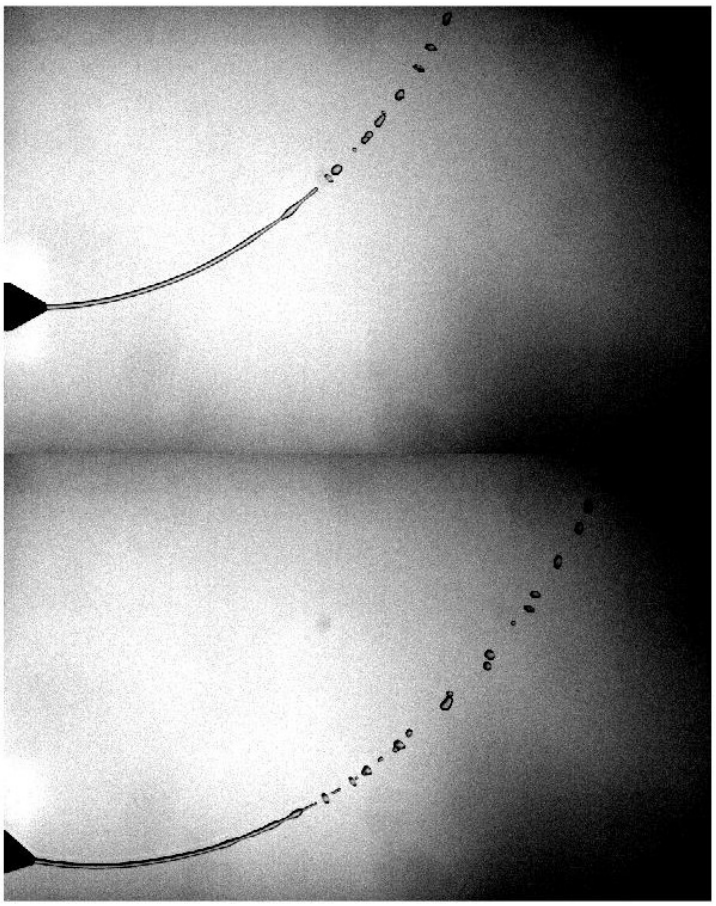

Figure 3.7: Input images to code, top and bottom images are a few time steps apart.

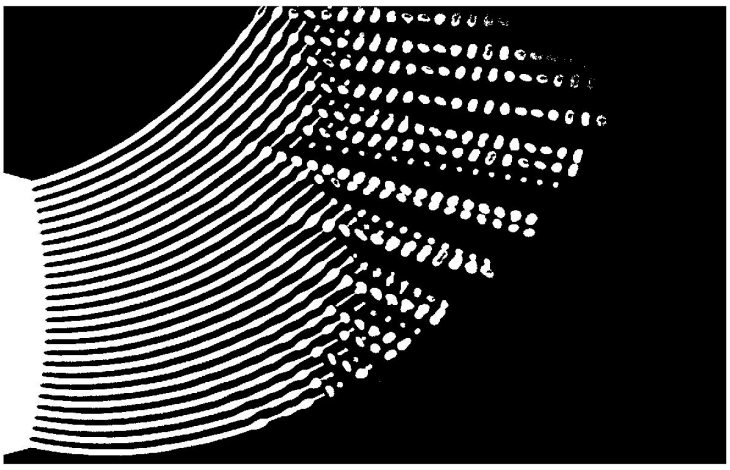

Figure 3.8: Pre-processing images (Temporally evolving jet).

an unperturbed jet is shown, this is a more powerful image as it gives both spatial and temporal information, in other words this is a video recording shown in an image.

In order to calculate the wavelength and the growth rate, an individual wavelength has to be tracked over time. This is done using 2D cross-correlation. The code takes the wavelength to be tracked as input on the i^{th} image and finds the closest looking wavelength in the $i+1^{th}$ image. Then it cross-correlates the newly found

wavelength on $i+1$ image to find its temporal evolution in $i+2$ image and so on. This process is explained in the figure 3.9. Here an individual wavelength is tracked over 6 images. The wavelength that are tracked till breakup occurs is shown in figure 3.10.

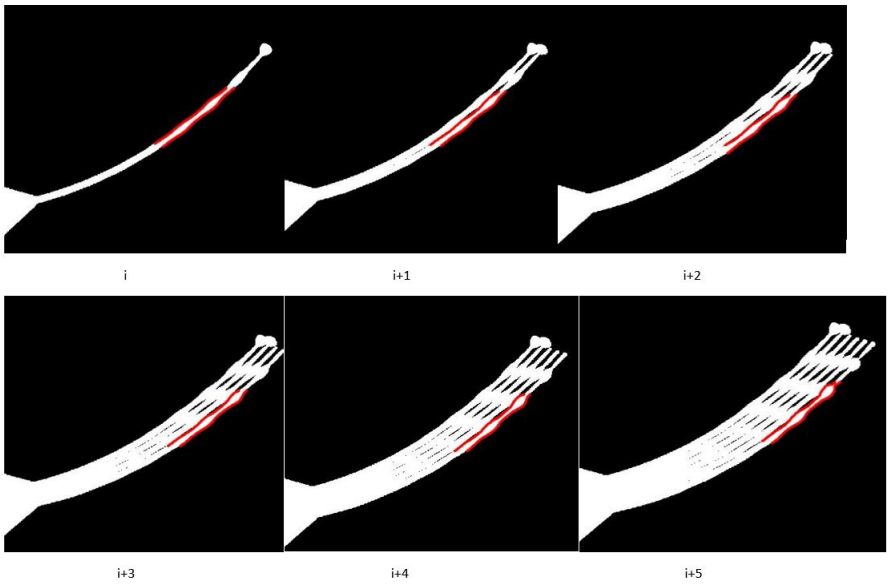

Figure 3.9: Wavelength tracked over time.

Figure 3.10: Temporal evolution of a wavelength.

Finally the wavelength, diameter of crest and trough are calculated for individual wavelets over time. A separate function is written for this purpose. This function fits a straight line as the trajectory of the wavelength and rotates the image such that the jet is perpendicular. Here an assumption is made that the trajectory over one wavelength is a straight line. Now by drawing horizontal lines the diameter is found as a function of the trajectory length. This process is shown in figure 3.11. Red and blue line on the image on the right shows the two crests and the trough, from which the wavelength and the diameters of crests and troughs are calculated.

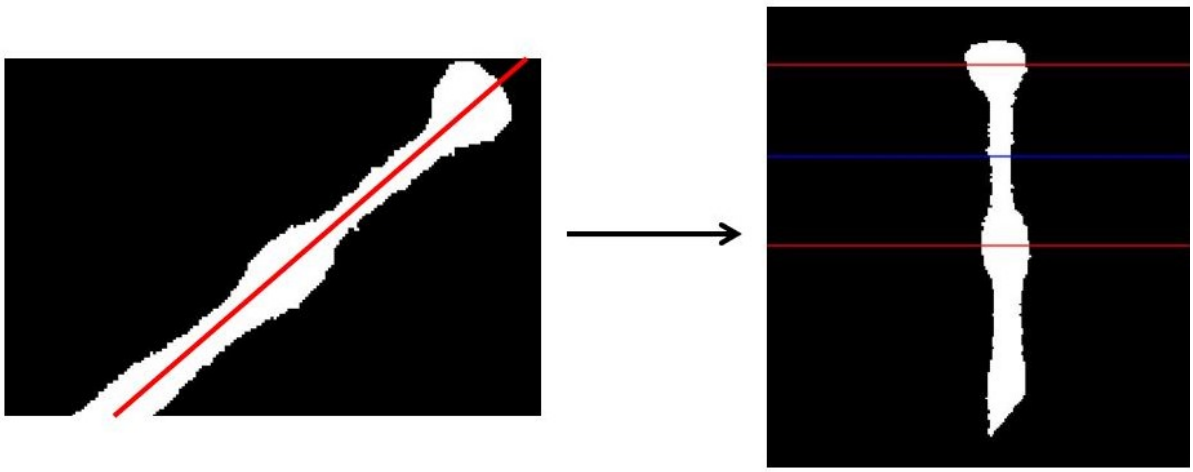

Figure 3.11: Acquiring quantitative data from wavelets.

3.7. Summary

A comprehensive dimensional analysis for the prilling process is developed and a robust experimental rig is built. The guidelines proposed in section 1.6.1 and 2.4, viz. active perturbation with piezo crystals, minimising vibration in the system, hydrophobizing the nozzle and a hydro-static pump were implemented in the new design. Apart from this, lesson learnt from rotating bucket experiments are also implemented, i.e. the provision made for the precise measurement of velocity. It is worth to mention that doing straight jets and rotating bucket experiments were vital in conceptualizing the new design. Furthermore, a MATLAB program is developed for obtaining quantitative data from spiralling jet images.

4

Results and discussion

This chapter presents the results of the experimental analysis of spiralling jets. It begins with the derivation of linear temporal instability analysis for spiralling jets, as the literature ([24]) only gives a spatial analysis. Following that, experimental values of wavenumber and linear growth rate are plotted against the theoretical lines. Finally, a simple route for achieving mono-dispersity is presented. The dimensional numbers implemented in the experiments are given in the table 4.1. The scaled amplitude of perturbation is not estimated. Usually in literature a transfer function is experimentally found to estimate the same.

Dimensional Numbers	Values
Weber number (We)	18.21
Rossby number (Rb)	5.96
Froude number (Fr)	2.16
Ohnesorge number (Oh)	0.006
T	1508
Density Ratio	0.0012
C_d	1
Ratio of centrifugal to hydrostatic forces	1.95
Scaled angular frequency (ω_r^*)	0.7, 0.9 & 1.1
Scaled amplitude of perturbation	> 0

Table 4.1: Dimensional numbers of the experiments conducted in the new experimental setup. Refer to table 3.3 and 3.2 for the definition of these dimensional numbers

The transfer function f given in equation 2.1 has not be found for the perturbation mechanism used in this study. Hence, the relation between the applied voltage and the amplitude of velocity perturbation is unknown and is given as a recommendation for the future research. Hence, the scaled amplitude of perturbation ($\delta U/U$) is unknown and is given as a value greater than zero in table 4.1. In the rest of the discussion the actual value of volts given to the piezo crystal is considered as a measure of the amplitude of perturbation. Higher the voltage stronger the perturbation.

It can be seen that the ratio of centrifugal to hydrostatic forces is 1.95 in the new setup whereas this number is of the order of 1/1000 for a typical prilling process. Meaning the jet experiences a significant acceleration in the nozzle in the new setup when compared to the actual prilling process where the acceleration in the nozzle is negligible. But this enables reaching high jet velocities in the lab scale setup with a hydrostatic pump that is only a few centimeters tall instead of one that is few meters tall, while the operating rotation rates are still approximately the same as that of the prilling process.

4.1. Temporal instability analysis

A slender jet approximation is assumed in the calculation of the spiralling jet trajectory by Shikhmurzaev and Sisoev [38]. Following that, Li et al. [24] used the same approximations to derive the spatial linear instability dispersion relation. In this section the same equations will be used to derive the temporal linear instability

dispersion relation for spiralling jets. A temporal instability analysis is necessary because of the way post-processing is done which is by tracking a wavelength over time, i.e the capillary growth is calculated in a Lagrangian frame moving with jet velocity.

$$\frac{\partial h}{\partial t} + u\frac{\partial h}{\partial s} + \frac{h}{2}\frac{\partial u}{\partial s} = 0 \tag{4.1}$$

$$\rho\left(\frac{\partial u}{\partial t} + u\frac{\partial u}{\partial s}\right) = -\gamma\frac{\partial \kappa}{\partial s} + 3\mu\frac{\partial^2 u}{\partial s^2} \tag{4.2}$$

The simplified continuity equation and momentum equation for the inviscid spiralling jets is shown in equations 4.1 and 4.2. The equations presented here are in dimensional form. They are obtained by incorporating slender jet approximations on the base flow. These derivations can be found in Eggers [10] and hence not repeated here. Another assumption made here is that the cross section of the base flow is circular and the trajectory passes through the center of this circle. This assumptions is also valid when considering first order terms in the trajectory equations (refer [24]). These equations are same as the straight jet case, but now the base flow is chosen as the spiralling case. The base flow is obtained from Shikhmurzaev and Sisoev [38].

$$h(s,t) = h_0(s) + \tilde{h}(s,t) \tag{4.3}$$

$$u(s,t) = u_0(s) + \tilde{u}(s,t) \tag{4.4}$$

$$\tilde{h}(s,t) = \epsilon_h e^{i(ks-\omega t)} \tag{4.5}$$

$$\tilde{u}(s,t) = \epsilon_u e^{i(ks-\omega t)} \tag{4.6}$$

Here s is the length along the streamwise direction, h(s,t) is the radius of the jet at any point in space and time, u(s,t) is the velocity in stream wise direction. k is the real wavenumber and ω is the complex angular frequency. h_0 and u_0 corresponds to the base flow and are only functions of streamwise direction (s) and $\tilde{h}$ and $\tilde{u}$ are the perturbations on the base flow, which are functions of both streamwise direction and time (s,t) given as follows,

Substituting h(s,t) and u(s,t) in to equations 4.1 and 4.2 and negating the base flow for an inviscid case, the following set of equations 4.7 and 4.8 are obtained. The simplifications performed are explained in Appendix D.

$$(ku_0 - \omega)\epsilon_h + \frac{kh_0}{2}\epsilon_u = 0 \tag{4.7}$$

$$\frac{\gamma k}{\rho}\left(k^2 - \frac{1}{h_0^2}\right)\epsilon_h + (ku_0 - \omega)\epsilon_u = 0 \tag{4.8}$$

Equations 4.7 and 4.8 form a set of homogeneous equations, this set of equations has a non-trivial solutions only if the determinant of the coefficient matrix is zero, given in equation 4.9.

$$(ku_0 - \omega)^2 - \frac{\gamma}{2\rho h_0^3}(k^4 h_0^4 - k^2 h_0^2) = 0 \tag{4.9}$$

By substituting $\omega = \omega_r + i\omega_i$ and k as real in 4.9 and equating the real and imaginary parts, the relations 4.10 and 4.11 are obtained. It can be seen that these equations are same for the straight jet as we used the straight jet equations. But these equations have to be solved along with the base flow of spiralling jets.

$$\omega_r = ku_0 \tag{4.10}$$

$$\omega_i = \sqrt{\frac{1}{2}\frac{\gamma}{\rho h_0^3}(k^2 h_0^2 - k^4 h_0^4)} \tag{4.11}$$

From equation 4.10, the wave-speed is given as,

$$c_r = \omega_r / k = ku_0 / k \implies c_r = u_0 \tag{4.12}$$

Hence, the wave travels at the same speed as the local velocity of the jet.

Non-dimensionalising the growth rate (equation 4.11), with advection time scale,

$$\omega^*_{i,adv} = \sqrt{\frac{k^{*2}}{2We h^*_0}(1-(k^* h^*_0)^2)} \tag{4.13}$$

In equation 4.13 the time scale used is $t_{adv} = H/U$, the scale for length is H (radius at the nozzle) and the scale for velocity of jet is U (velocity at the nozzle). An equivalent spatial growth rate can be derived by, $k_i = -\omega_i / u_0$, as given in 4.14.

$$k^*_{i,adv} = -\sqrt{\frac{k^{*2}}{2We h^*_0 u^{*2}_0}(1-(k^* h^*_0)^2)} \tag{4.14}$$

Although the growth rates 4.13 and 4.14 only depends on We number, they have to be solved along with the spiralling jet base flow equations given in Shikhmurzaev and Sisoev [38] to obtain the continously changing u_0 and h_0. The MATLAB program for solving the base flow was provided by the thesis daily supervisor Yavuz E. Kamis. The figure 4.1 compares the the spatial growth rate obtained by derivation in this study to the spatial growth rate given by Li et al. [24]. Here the spatial growth rates are plotted against the scaled velocity which serves as a proxy for streamwise direction 's' . The Fr and Rb numbers are kept constant at 2.5 and 5 respectively, the dimensionless excitation frequency $\omega^*_r = 0.7$ and the We number is varied from 5 to 100. It can be seen that the k_i from equation 4.14 closely follows the k_i obtained in [24] except for small We numbers, this is trend that is similar to the trend observed in straight jets.

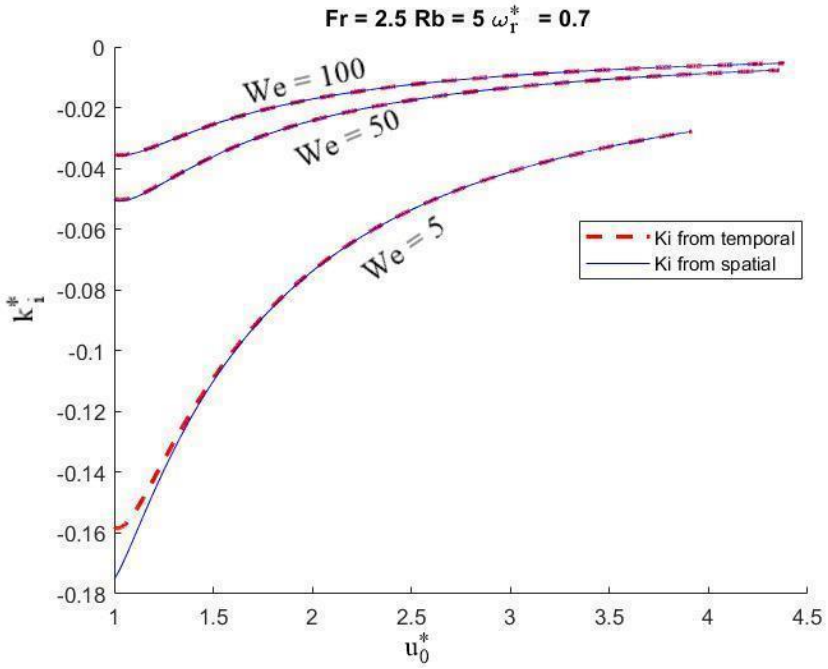

Figure 4.1: The spatial growth rate obtained in this study compared to the spatial growth rate from Li et al. [24].

4.2. Wavenumber and Linear growth rate

The wavelength obtained from post-processing is converted into non-dimensional wavenumber by the equation 4.15. The corresponding non-dimensional velocity of the jet, where the wavenumber is calculated is given in equation 4.16. Using equations 4.16 and 4.15 the wavenumber can be verified against the theoretical results.

$$k^*_r = k_r H = \frac{2\pi H}{\lambda} \tag{4.15}$$

$$u^*_0 = \frac{u_0}{U} \implies u^*_0 = \frac{c_r}{U} \qquad \text{(From equation 4.12)}$$

$$u_0^* = \frac{\omega_r / k_r}{U} \tag{4.16}$$

The linear growth rate is found by tracking a wavelength as discussed in section 3.6. The radius of the swelling crest is found from the images and subtracted from the unperturbed radius and plotted over time in a semi log scale. A line is fitted through the experimental values of equation 4.18 whose slope will give the capillary growth rate. As the growth rate measured is the slope of a fitted line in the graph of $log(h_{crest}(t) - h_0)$ against time, the slope also has an error, as the value of $h_{crest}(t) - h_0$ has an measurement uncertainty associated with it. To make things more complicated performing a logarithmic transformation to this data yields a non-uniform uncertainty to $log(h_{crest}(t) - h_0)$ (i.e) uncertainty at each time step is different. Such an error analysis and line fitting through data with non-uniform uncertainty is presented in Appendix E. Surprisingly this type of error analysis is not found in previous literature for growth rate measurement.

$$h_{crest}(t) = h_0 + \epsilon_h e^{(\omega_i t)} \tag{4.17}$$

$$\omega_i t + log(\epsilon_h) = log(h_{crest}(t) - h_0) \tag{4.18}$$

The ω_i measured is a dimensional quantity, hence it is multiplied by the capillary time scale ($t_c = \sqrt{\frac{\rho H^3}{\gamma}}$) to give $\omega_{i,cap}$. To plot the data against the spatial growth rate given by Li et al. [24] the following conversion is made,

$$\omega^*_{i,adv} = \omega^*_{i,cap} / \sqrt{We}$$

$$k^*_{i,adv} = -\omega^*_{i,adv} / u^*_o$$

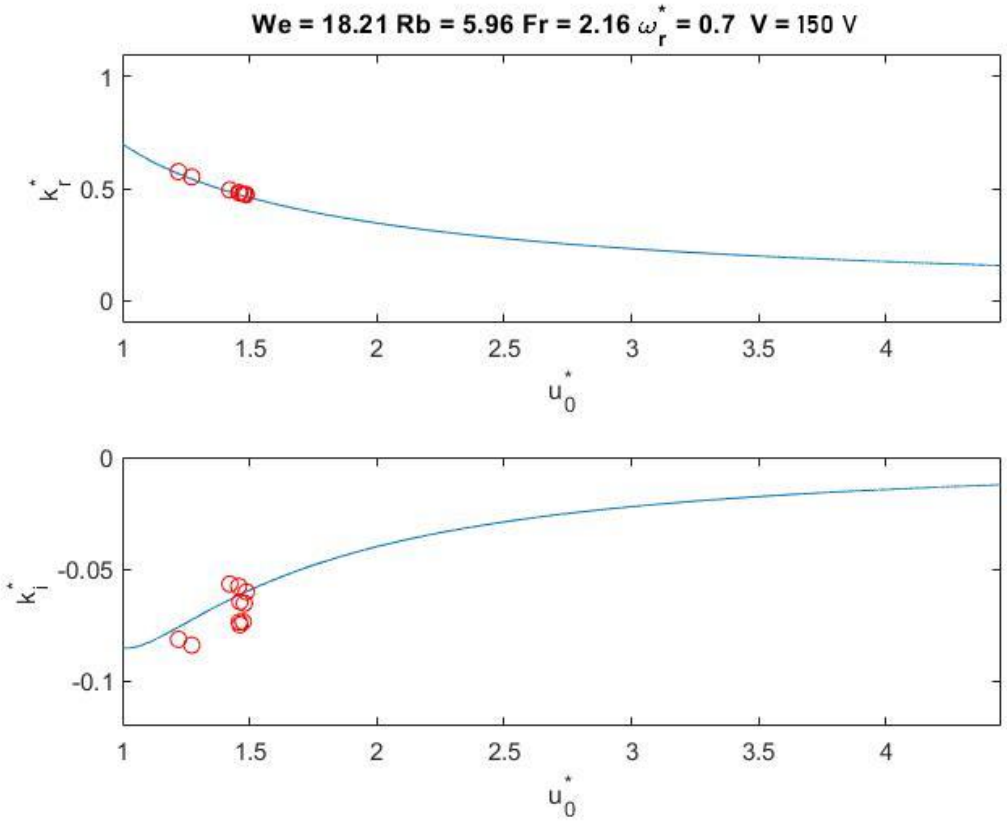

Figure 4.2: Experimental validation of wave-stretching and spatial growth rate. The red circles indicate the experimental values and the blue lines are the theoretical values.

The time steps are set by the frequency of the camera. To have sufficient temporal resolution, the camera frequency is set to $5 \times \omega/(2\pi) = 5 * 500$ Hz = 2500 Hz. A continuous video is taken every time the jet passes over the camera and 10 such sweeps are taken. The figure 4.2 shows the experimental values plotted against the theoretical lines, here the non-dimensional angular frequency is set at 0.7 and the amplitude of the vibrations is set to 150 Volts which corresponds to 9 μm displacement of the perturbation plate (the displacement values corresponding to the applied voltage are known from the manufacturer). A zoomed in version of the same figure along with the error in the experimental values is shown in figure 4.3. Each data point corresponds to one tracked wavelength. Ten such points are plotted corresponding to the ten sweeps of data collected. There is some difference in the local jet velocities because the start of the tracking and the end of the tracking is not exactly the same for different sweeps. It should be noted that the wavelengths are not tracked till they breakup, the tracking starts at a point where visible deformations starts and stopped when the deformations on the surface tends to deviate from sinusoidal waves. Typically a wave is tracked over 6 time steps. Hence the error bars plotted on the data points are standard deviation rather than standard error. Another way to calculate capillary growth rate would be to calculate the difference between the radius of the crest and the radius of the trough which was also found to give growth rate values very close to the ones plotted on the figure 4.2.

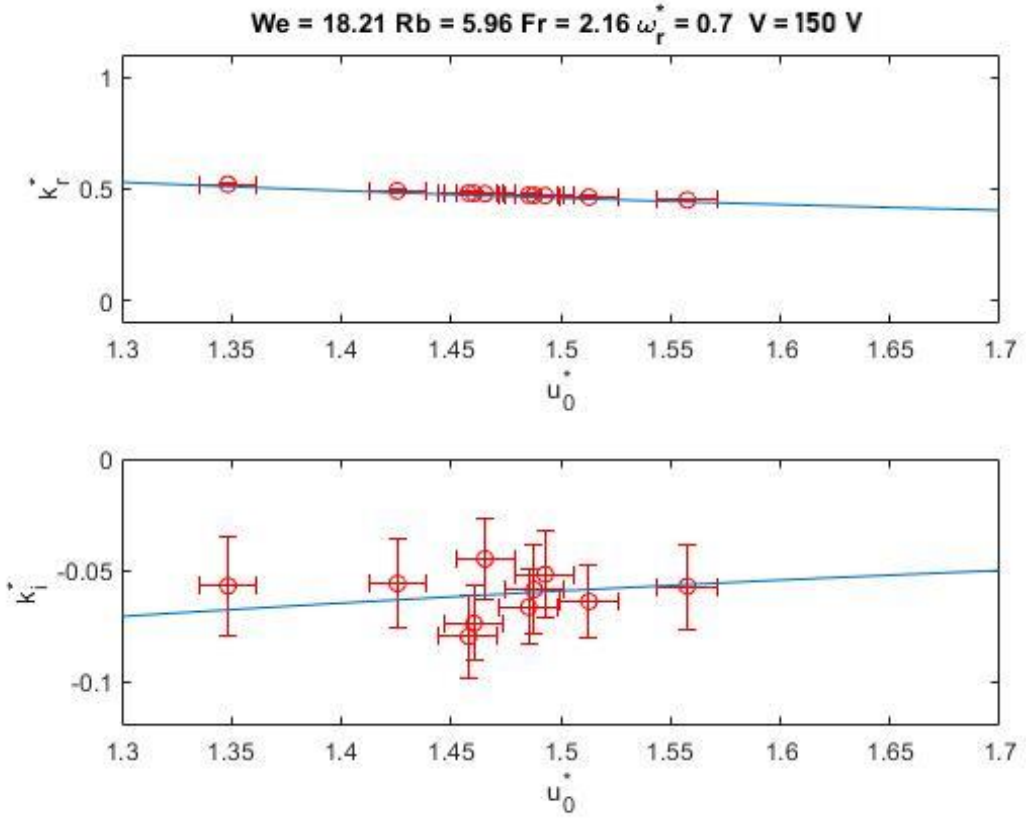

Figure 4.3: Experimental validation of wave-stretching and spatial growth rate zoomed in version. The red circles indicate the experimental values and the blue lines are the theoretical values. There is error bars in both directions as the scaled local jet velocity (u_0^*), the non-dimensional wavenumber (k_r^*) and non-dimensional spatial growth rate (k_i^*) all are experimentally determined from the images. The error in k_r^* is very small to be noticed on the figure.

4.3. Elimination of satellite drops

Following a wavelength over time, two competing phenomena determine the break-up dynamics. The rate of strain (du_0/ds) experienced by the jet has a damping effect on the growth of the instability as proposed by Tomotika [42]. While the surface tension force causes the exponential growth of the instability. Figure 4.4 shows the individual effects of strain rates, capillary growth and the combined effect. It can be seen that the combined effect of the straining and capillary growth are superposition of both effects. Depending on the

actual rate of both effects one or the other dominates the jet evolution. As discussed earlier in section 1.2.4 the competition between the two phenomenon is governed by the dimensionless number T. For the spiralling jet investigated in this thesis the dimensionless number T is 1508. As T >> 1 the capillary waves are not damped and they grow exponentially in time (refer figure 1.11). Another phenomena that could damp the instability is the viscosity, but the Ohnesorge number = 0.006 (<< 1). So the viscosity does not affect the linear growth rate of the perturbations.

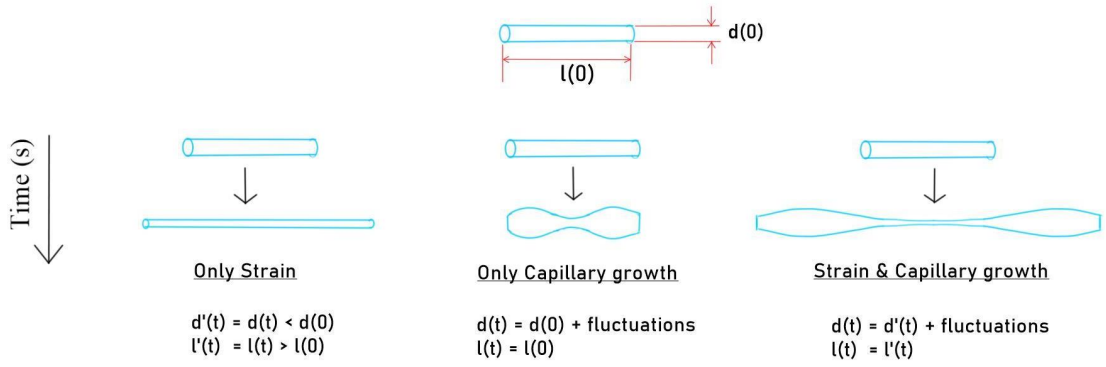

Figure 4.4: Schematic representation of fluid straining, capillary growth and the combined effect (Not to scale).

For analysis purpose a straight jet with the same initial radius and same T value as the spiralling jet is analysed in figure 4.5. Figure 4.5 (a) shows the growth of the small perturbation ($\epsilon_h = h_0/100$) over time and the evolution of the base radius of the jet over time. Figure 4.5 (b) shows the decrease in the non-dimensional wavenumber over time. Although the low strain rate does not damp the growth of capillary waves, it is sufficient enough to stretch the wavelengths. The point where $ln(\epsilon(t))$ and $\ln(h_0(t))$ meet corresponds to the time t = 0.019. This is the time instant when the perturbations become as large as the local jet radius and the break-up occurs (based on linear analysis). The near break-up non-dimensional wavenumber is 0.32 for this case.

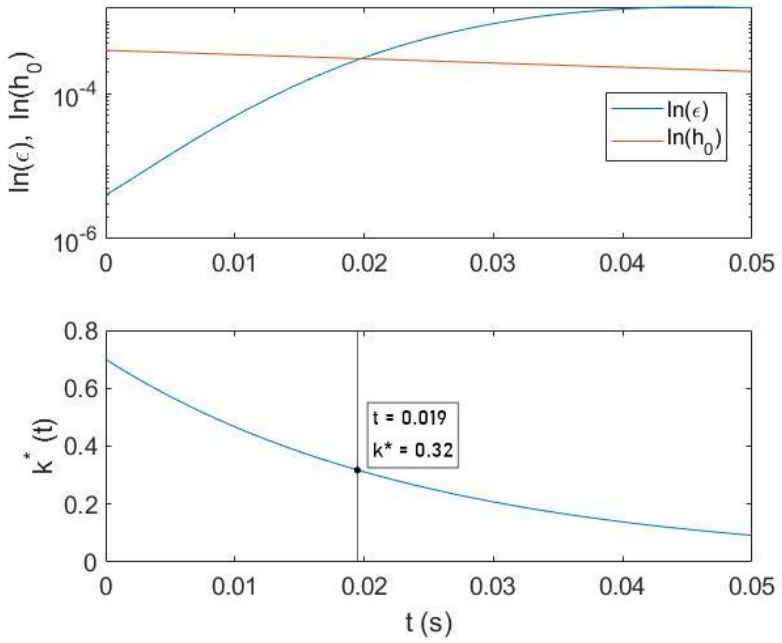

Figure 4.5: Evolution of perturbations for a water jet along with h_0 and k^*. The initial conditions are $h_0(0)$ = 0.4 mm, $\epsilon(t=0) = 0.01 \times h_0(0)$ and $k^*(0) = 0.7$. The T = 1508 and the σ = 27.

The spiralling case is different from the straight jet case because σ ($= du_0/ds$) is not a constant along the jet trajectory. The T value is therefore changing continously along the stream wise direction of the jet. From simple force balance it is found that,

$$u_0 \frac{du_0}{ds} \approx \Omega^2 L \tag{4.19}$$

$$u_0(s) \approx (u_0)\,|_{s=0} \sqrt{1 + \frac{2\Omega^2 L s}{(u_0)\,|_{s=0}}} \tag{4.20}$$

$$u_0(s) \approx U\sqrt{1 + \frac{2\Omega^2 L s}{U}} \qquad (\because (u_0)\,|_{s=0} = U) \tag{4.21}$$

The approximate strain rate is given as,

$$\sigma = \frac{du_0}{ds} \approx \frac{\Omega^2 L}{U} \times \frac{1}{\sqrt{\left(1 + \frac{2\Omega^2 L s}{U^2}\right)^3}} \tag{4.22}$$

From the above equation it can be seen that the value of σ is decreasing in the downstream direction. For ease of use the maximum value of σ ($= \Omega^2 L/U$) which occurs at the nozzle is used so far for the calculation of T. Since σ decreases in the downstream direction the value of T increases. So the stretching becomes weaker in the downstream direction.

4.3.1. Tuning the perturbation frequency

Experiments are done for the three different perturbation frequencies viz. $\omega_r^* = 0.7,\ 0.9$ & 1.1 for the experimental conditions given in table 4.1. These different frequencies correspond to different initial conditions of k_r^*. 50 different measurements of the wavelength near breakup is found and their mean is taken. Using the equations 4.15 and 4.16 the corresponding k_r^* and u_0^* is found. This data is plotted against the theoretical curves for different frequencies of perturbation as shown in figure 4.6.

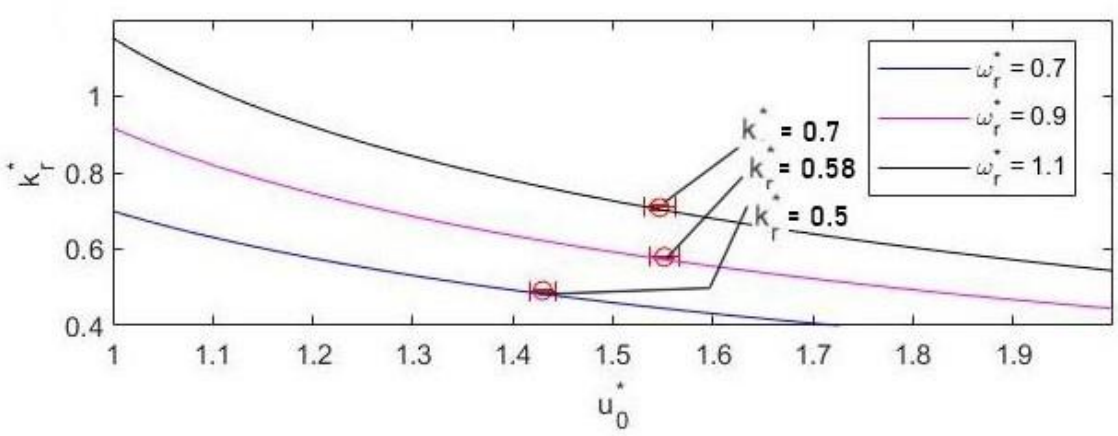

Figure 4.6: Experimental values of near break-up non-dimensional wavenumber for different perturbation frequencies are plotted against the theoretical curves. The non-dimensional numbers are kept as the same as given in table 4.1 and the perturbation amplitude corresponds to 150 V.

It can be seen in the figure 4.6 that the reduced wavenumber just before breakup is 0.5, 0.58 and 0.7 respectively for the reduced angular frequencies 0.7, 0.9 and 1.1, meaning shorter and shorter wavelengths breakup. In the case of $\omega_r^* = 0.7$, the $k_r^*|_{noz} = 0.7$ and before breakup $k_r^* = 0.5$, which results in a longer ligament and bigger satellite drops. This is shown in the figure 4.7.

Figure 4.8 shows the temporal evolution of the same jet with an angular perturbation of $\omega_r^* = 0.9$. Here the reduced wave number near breakup is $k_r^* = 0.58$. This is already a shorter wavelength than the previous case and is reflected in the smaller satellite drop size.

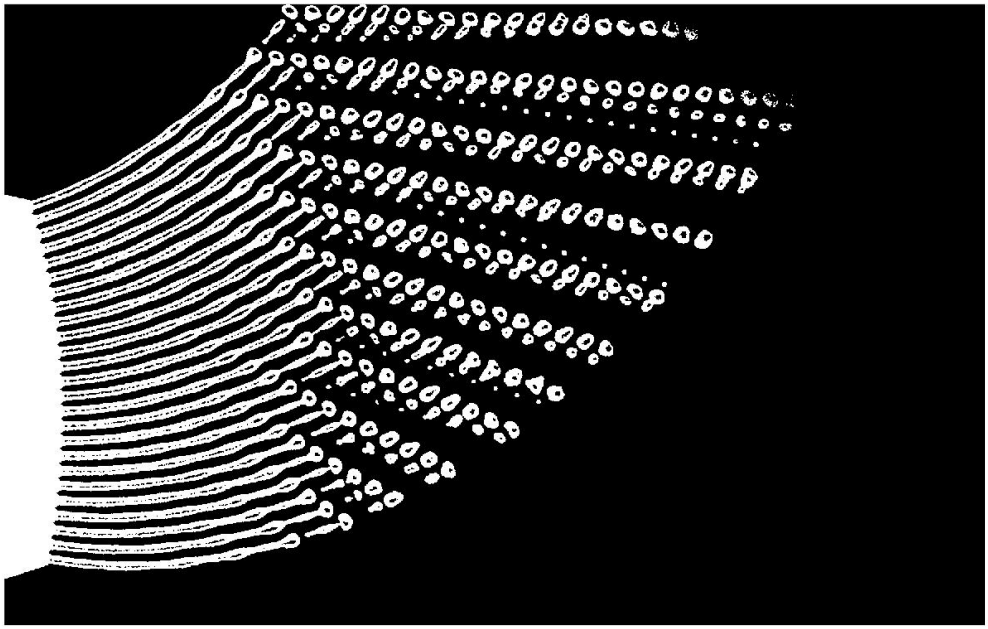

Figure 4.7: Temporally evolving jet perturbed at $\omega_r^* = 0.7$. The non-dimensional numbers are kept as the same as given in table 4.1 and the perturbation amplitude corresponding to 150 V.

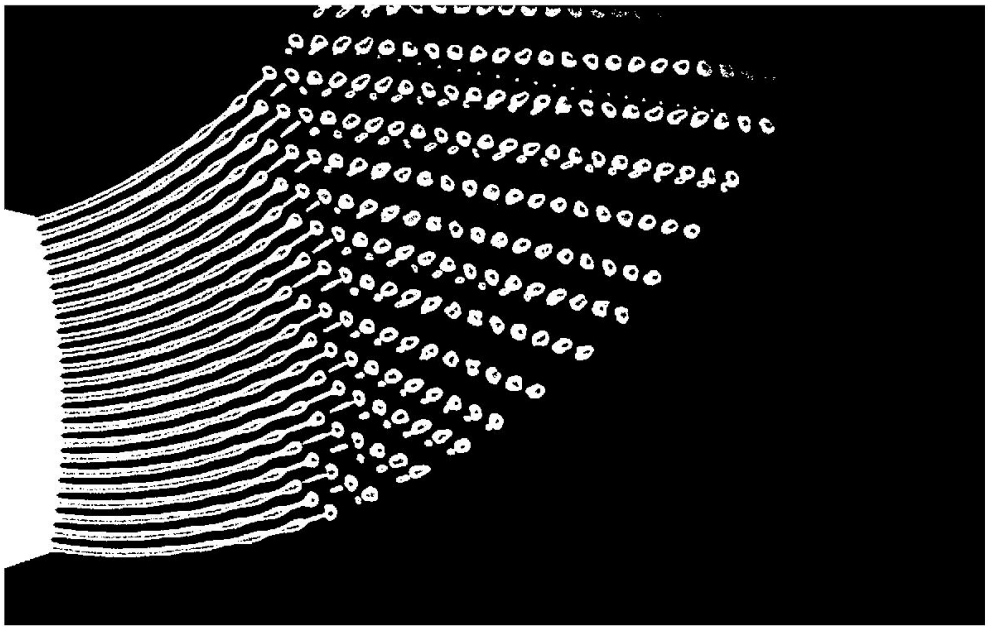

Figure 4.8: Temporally evolving jet perturbed at $\omega_r^* = 0.9$.The non-dimensional numbers are kept as the same as given in table 4.1 and the perturbation amplitude corresponding to 150 V.

Finally, figure 4.9 shows the jet with an angular perturbation of $\omega_r^* = 1.1$. Here the reduced wave number near breakup is $k_r^* = 0.7$. Figure 4.10 shows the wavelengths before breakup for the three different frequencies of perturbation. This gives a visual representation of decrease in the wavelengths when perturbed at increasing frequencies. Also it can be seen that the satellite drops are at its smallest when the near breakup

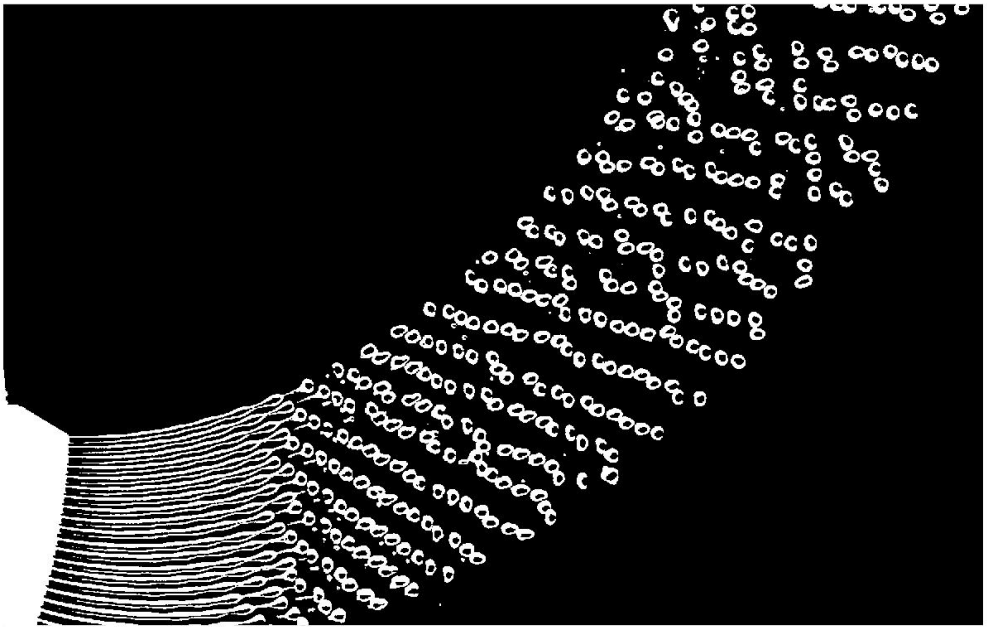

Figure 4.9: Jet perturbed at $\omega_r^* = 1.1$. The non-dimensional numbers are kept as the same as given in table 4.1 and the perturbation amplitude corresponding to 150 V.

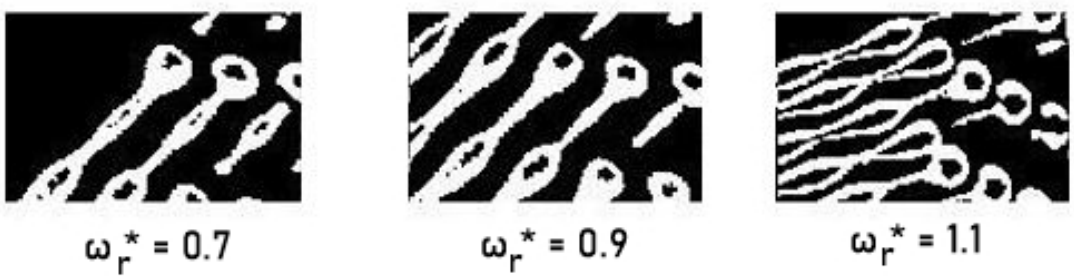

Figure 4.10: Near breakup wavelengths visual representation. All the three images are in the same scale. The non-dimensional numbers are kept as the same as given in table 4.1 and the perturbation amplitude corresponding to 150 V.

non-dimensional wavenumber (k_r^*) is 0.7. This corresponds to a non-dimensional angular perturbation frequency of $\omega_r^* = 1.1$ for the non-dimensionless numbers chosen in this thesis. For satellite drop elimination having a smallest satellite drops is more suitable. So the frequency of perturbation has to be changed such that the near breakup non-dimensional wavenumber is 0.7.

4.3.2. Tuning the perturbation amplitude for satellite elimination

The spiralling jet perturbed at $\omega_r^* = 0.9$ for three different amplitudes of perturbation (75, 100 & 150 V) is analysed in this section. Figure 4.11 shows the jet perturbed at 75 V. Since the jet is perturbed at $\omega_r^* = 0.9$ the near breakup non-dimensional wavenumber is 0.58. In the wavelength tracked with red boxes, rear separation and forward merging seems to happen. Although the actual merging is not seen in the field of view which may or may not happen downstream. The wavelength tracked in green boxes have a forward separation and rear merging. Therefore, at this perturbation amplitude the merging seems to be irregular.

When the amplitude of perturbation is increased to 100 V for the same frequency of perturbation the merging is more regular as shown in figure 4.12. The rear separation (green boxes) happens more consistently for this amplitude of perturbation and the merging appears to be forward merging. In some cases the merging happens in the field of view and it other cases it may or may not happen downstream.

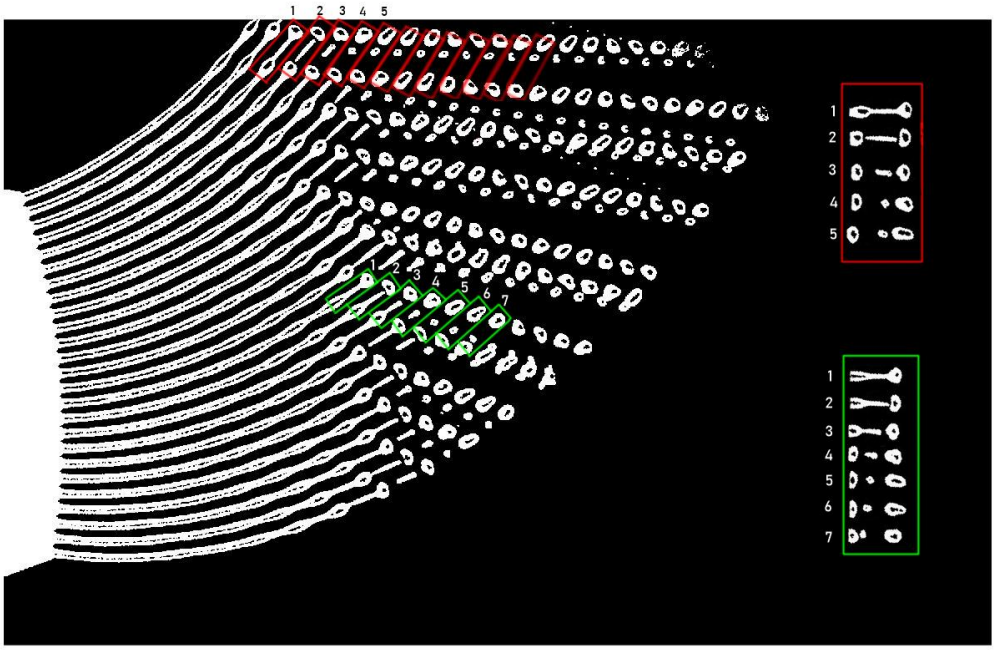

Figure 4.11: Temporal evolution of jet perturbed with $\omega_r^* = 0.9$ and an amplitude corresponding to 75 V. All the other non-dimensional numbers are kept as the same as given in table 4.1.

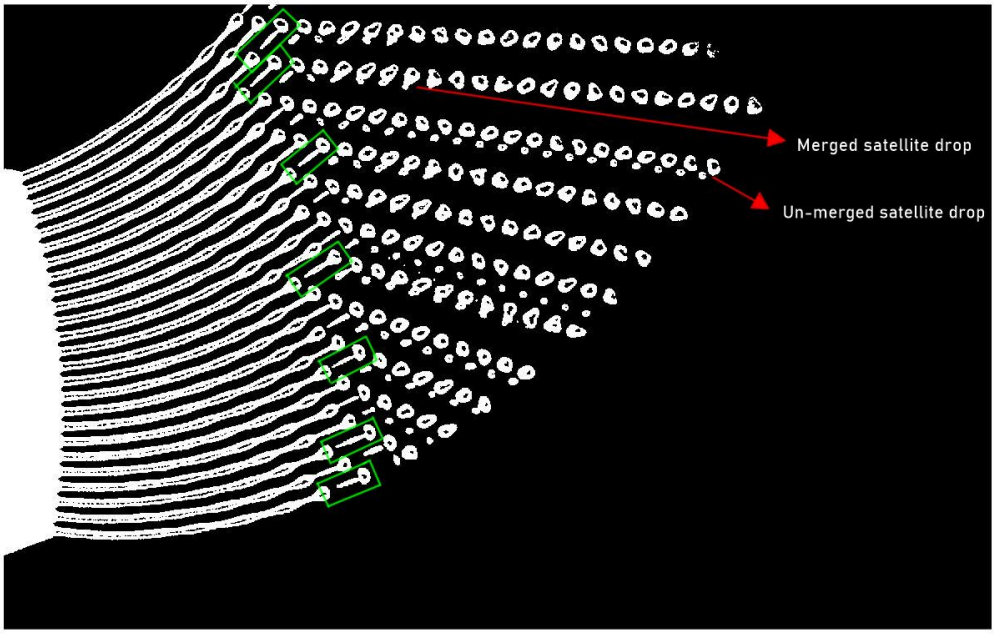

Figure 4.12: Temporal evolution of jet perturbed with $\omega_r^* = 0.9$ and an amplitude corresponding to 100 V. All the other non-dimensional numbers are kept as the same as given in table 4.1.

When the perturbation amplitude is set to 150 V the temporal evolution of the jet is shown in figure 4.13. Here a rear separation and forward merging is observed. The satellites merge with the main drops in the field of view itself. This combination of frequency and amplitude of perturbation results in a uni-modal distribution of drop sizes. Although this is not the most optimum frequency ($\omega_r^* = 0.9$ instead of $\omega_r^* = 1.1$), it is used

to illustrate the effect of different amplitudes of perturbation. With increasing amplitudes of perturbation the merging time in the forward direction decreases. This is similar to that of the straight jet case in the rear separation and forward merging zone (see subs-section 1.2.3). Further investigation has to be done at several amplitudes of perturbation to validate this claim and get a smooth curve for merging time.
The figure 4.9 shows the jet perturbed at the optimum frequency ($\omega_r^* = 1.1$) and an amplitude of 150 V. The satellite drops are eliminated within the field of view and a uni-modal drop distribution is seen.

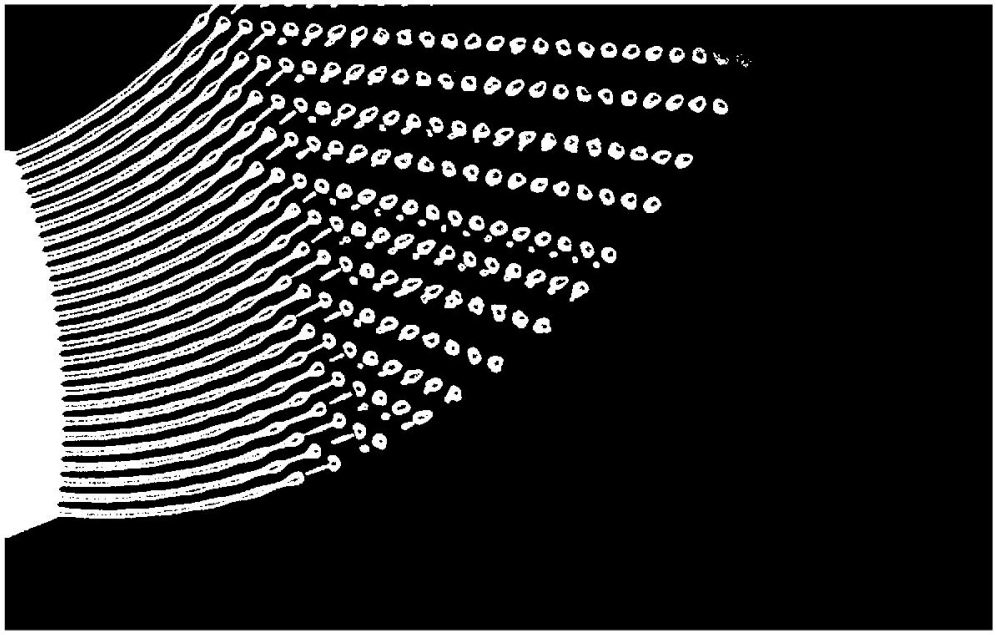

Figure 4.13: Temporal evolution of jet perturbed with $\omega_r^* = 0.9$ and an amplitude corresponding to 150 V. All the other non-dimensional numbers are kept as the same as given in table 4.1.

The We = 18.21 and the Oh = 0.006 should correspond to mode 2 breakup regime and have a bi-modal drop size distribution according to the experimental results of Wong et al. [45] as shown in figure 1.21. This is indeed the case when the jet is not externally perturbed. By introducing external perturbations and tuning them, the bi-modal distribution can be manipulated to give a uni-modal drop size distribution. Figure 4.14 shows the un-perturbed jet and a perturbed jet where the perturbations are tuned for satellite elimination. The sub-figures (c & d) give the histogram of the drop size distribution corresponding to the un-perturbed and the perturbed jet. A bi-modal distribution is seen for an un-perturbed jet and a uni-modal distribution for the perturbed jet. These histograms shown here should be considered only as an overall trend as some of the drops are still in the process of merging. In future works data should be collected further downstream of the jet so that the merging is completed.

4.4. Procedure to eliminate satellite drops in prilling process

In this study the capillary break up of spiralling water jets is controlled to have mono-dispersed drop sizes. A similar approach can be implemented in the prilling process to have mono-dispersity. The procedure is as follows:

1. For an unperturbed prilling process the size distribution of the product should be plotted. This bi-modal distribution will give an estimation of the wavenumber near breakup.

2. The jet should be perturbed on a trial and error basis. The bi-modal distribution from this perturbed jet will give a new estimation for the near breakup wavenumber. The perturbation frequency is increased till the near break-up non-dimensional wavenumber becomes close to 0.7. The satellite drops will still be present but will have a very small size.

3. Now the amplitude of perturbation is increased till the product drop size distribution is uni-modal.

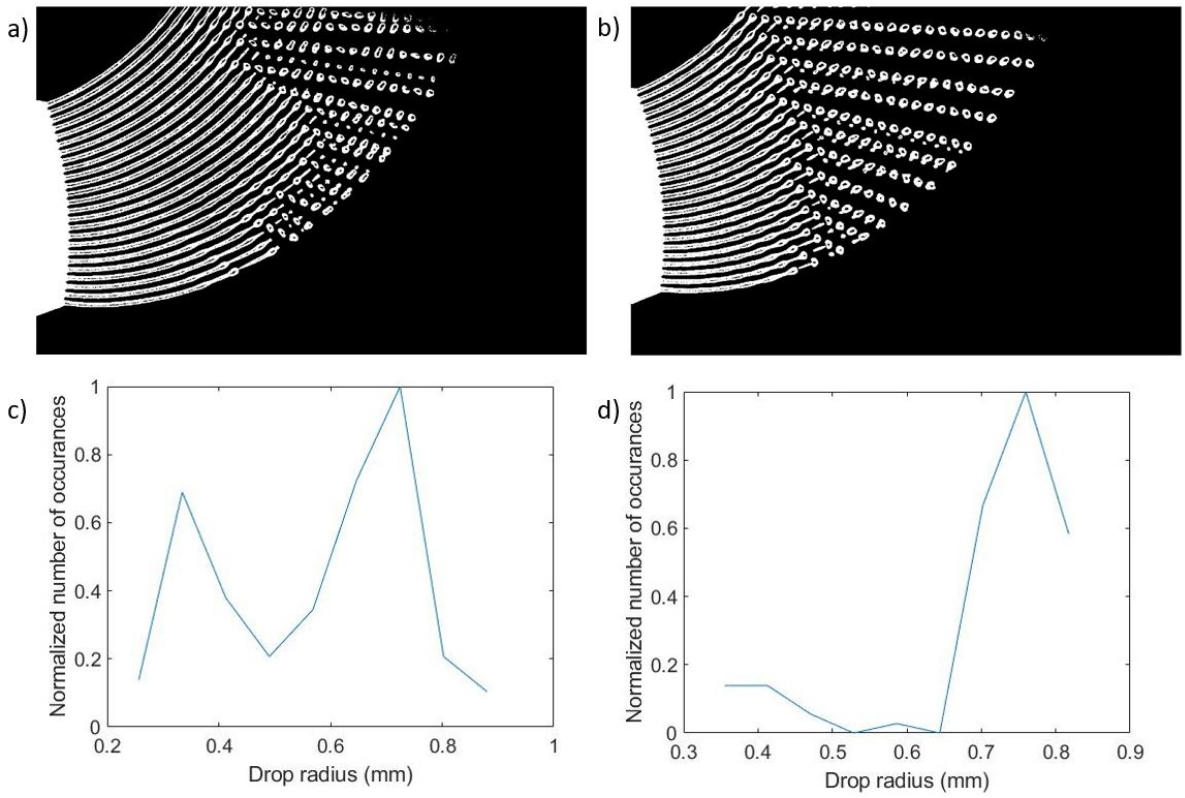

Figure 4.14: Temporal evolution of spiralling jets. All the other non-dimensional numbers are kept as the same as given in table 4.1. Sub-figure (a) shows the temporal evolution of an unperturbed jet. Sub-figure (b) shows the temporal evolution of jet perturbed with $\omega_r^* = 0.9$ and an amplitude corresponding to 150 V. Sub-figure (c) gives the histogram of 110 drops corresponding to sub-figure (a). Sub-figure (d) gives the histogram of 95 drops corresponding to sub-figure (b)

4.5. Summary

A temporal instability analysis is performed and its relation to spatial analysis is derived. It is found that for large We numbers, the conversion between spatial and temporal analysis is possible. Experiments to measure reduced wave number and growth rate are performed and the values are plotted against theoretical curves and a good agreement is found. The near breakup wavenumber determines the size of the satellite drops and can be changed by changing the perturbation frequency. The amplitude of perturbation governs the merging phenomena and can be tuned to merge satellite drops with the main drops. Finally, a route to satellite elimination is presented.

5

Summary and conclusions

5.1. Summary

In the pursuit of achieving mono-dispersity in the prilling process, the approach adopted led to the following:

- A straight jet experimental setup was built to understand the perturbation mechanisms and to gain a basic understanding of performing experiments on jet instabilities. Experimental workarounds and improvements that could be implemented in spiralling jet experiments were found.
- After repeating spiralling jet experiments from the literature, the limitations of the rotating bucket setup used in those studies were understood. Performing these experiments also gave insights into developing a new setup which could provide quantitative information on contrast to the qualitative research published so far. It was also clear that external perturbations are necessary for controlling the breakup process and hence were incorporated in the new setup.
- A comprehensive dimensional analysis was proposed for the prilling process.
- Experiments in spiralling jets were carried out in the new setup to validate growth rate and wavenumber against the theoretical values.
- The dimensional numbers chosen in the study falls in the mode 2 of the regime map found in the literature which has a bi-modal drop size distribution. The same was observed in the experiments from this thesis. By tuning the frequency and amplitude of perturbation it was possible to change the bi-modal distribution to uni-modal drop size distribution.

5.2. Conclusion

The study furthers the understanding of the breakup of spiralling liquid jets significantly through experimental analysis. This is achieved by validating the theoretical linear growth rate and wavenumber against the experimental values. Elimination of satellite drops which is crucial to the prilling process was achieved in a spiralling water jet by tuning the perturbation frequency and amplitude. A procedure to implement uni-modal drop size distribution in a prilling process is outlined.

5.3. Future recommendations

- The pressure measured at the fluid chamber whose FFT gives the same frequency of perturbation. The amplitude of these fluctuations can be used to model the velocity perturbations at the nozzle. This model will give a transfer function between the voltage of amplitude and velocity fluctuations.
- Post-processing code needs to be developed for obtaining the trajectory of the jet.
- Different combinations of the dimensionless numbers have to be experimented for mono-dispersity.

- The post-processing code developed uses a forced learning for certain operations. A machine learning code can be developed that uses this forced learning to automate the post-processing. Or else drop in flight visualisation technique developed by, "Image Expert" can be purchased which is a similar commercially available computer vision code developed for ink-jet printing industries (see [18]).
- Viscous fluids can also be tested, although there is limit to the viscosity of the liquid as the flow is driven by gravity. A pressure pump has to be implemented in the place of gravity pump for highly viscous liquids.
- For testing of high velocity jets and to reduce the blur error, a strobing capacitive LED has to be incorporated. This is to eliminate streaking behaviour. This step is in progress at the moment of publishing this thesis.
- Only the jet edges cast a shadow when the liquid is transparent, this complicates the post-processing in MATLAB. Hence using a dye would significantly reduce experimental challenges such as shadowgraphy and post processing.

A

Experimental setup

As the rotary union is the heart of this new setup, shown in figure A.1, the rest of the setup is designed around it. The next important part being the perturbations from piezo crystal it is designed next. The sizes of the piezo housing are designed with a massive weight so that it has high inertia and does not vibrate on itself when the perturbations are switched on. The setup in real life is shown in the figure A.2. The machining was done by Kreber industry. Additional components that are found in this figure includes, frequency spectrum analyser, frequency generator, power sources for diffuse light and piezo amplifiers. Figure A.3 shows the placement of diffuse light source and figure A.4 shows the timer belt connections between the motor and the rotary union.

The CAD models were developed in solidworks and the tolerancing was decided in communication with the manufacturer. The reader is encouraged to contact the author for CAD models.

Figure A.1: Rotary union.

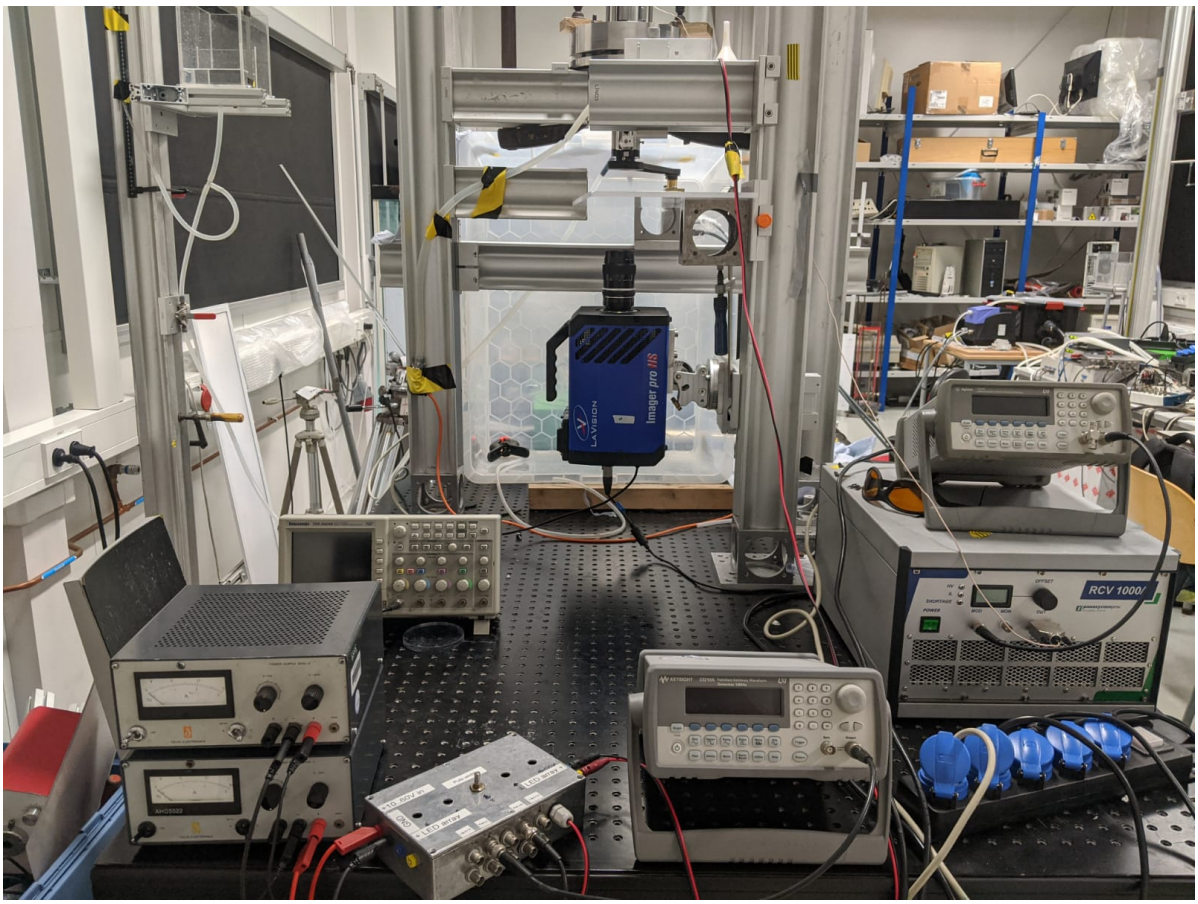

Figure A.2: Real life setup.

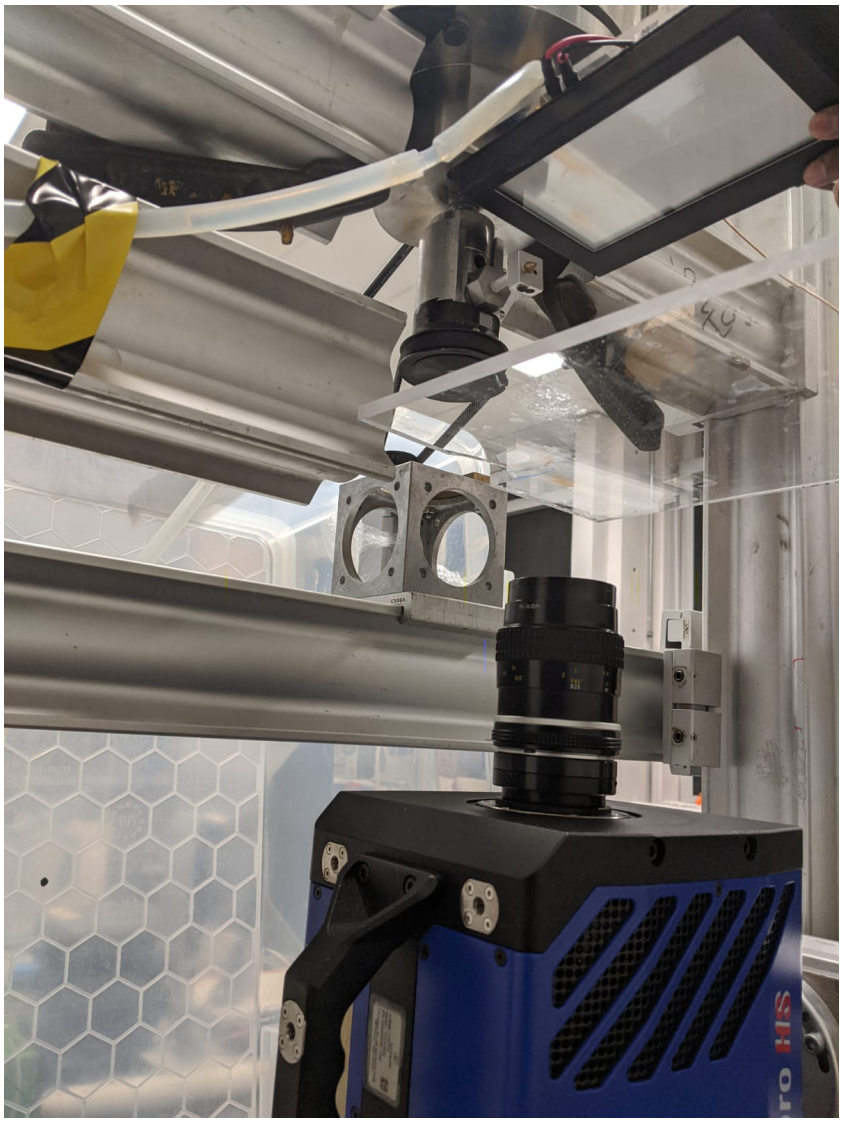

Figure A.3: Placement of diffuse light.

Figure A.4: Timer belt connections.

B

Modal analysis

The Eigen mode analysis of the plate that is perturbed is done. The plate that is perturbed is shown here along with a surface plot of displacement. When 150 V is applied to piezo crystal the shaft attached to the crystal moves 9 μm as shown in figure B.1. The 9 μm displacement is given at the 8 mm hole at the center of the plate in y direction.

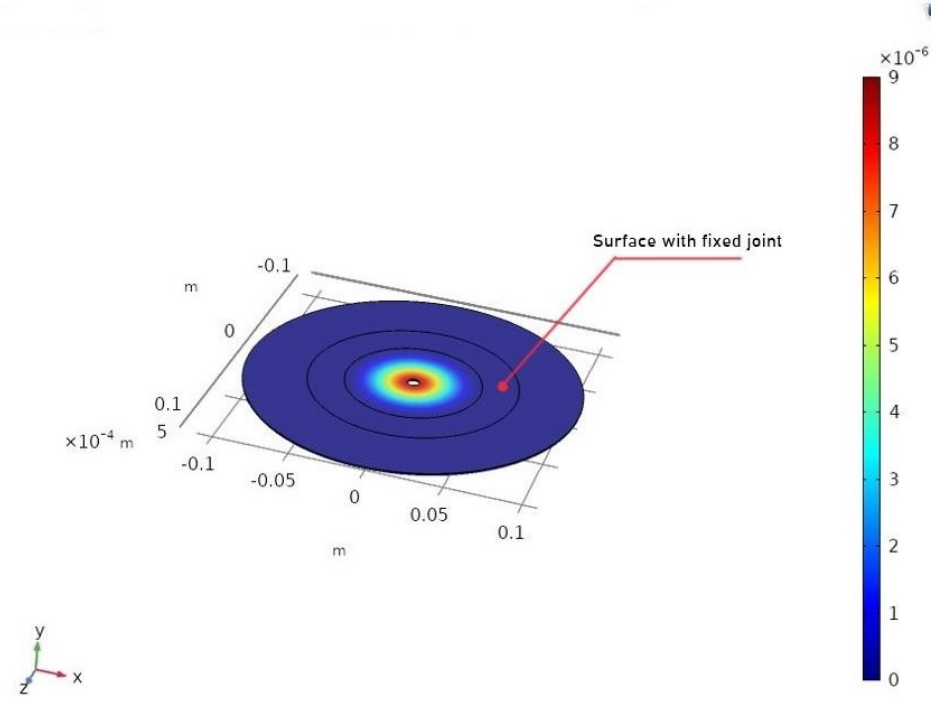

Figure B.1: Displacement plot.

The fluid that is to be perturbed is present inside the surface with fixed joints. Hence the interesting eigen mode is when the inner regions of the plate is excited. The first 14 eigen modes are shown in the figure B.2 and B.3. The mode that is dangerous to our process is found at the frequency of 1196 Hz. In this study the operating range of frequency is in between 500 - 850 Hz. If there is a need to operate the system at higher frequencies a thicker plate (thickness > 1 mm) can be used. The simulations are made in COMSOL with appropriate boundary conditions and discretization with the help of another student from mechanical engineering masters' (precision and micro-systems engineering track).

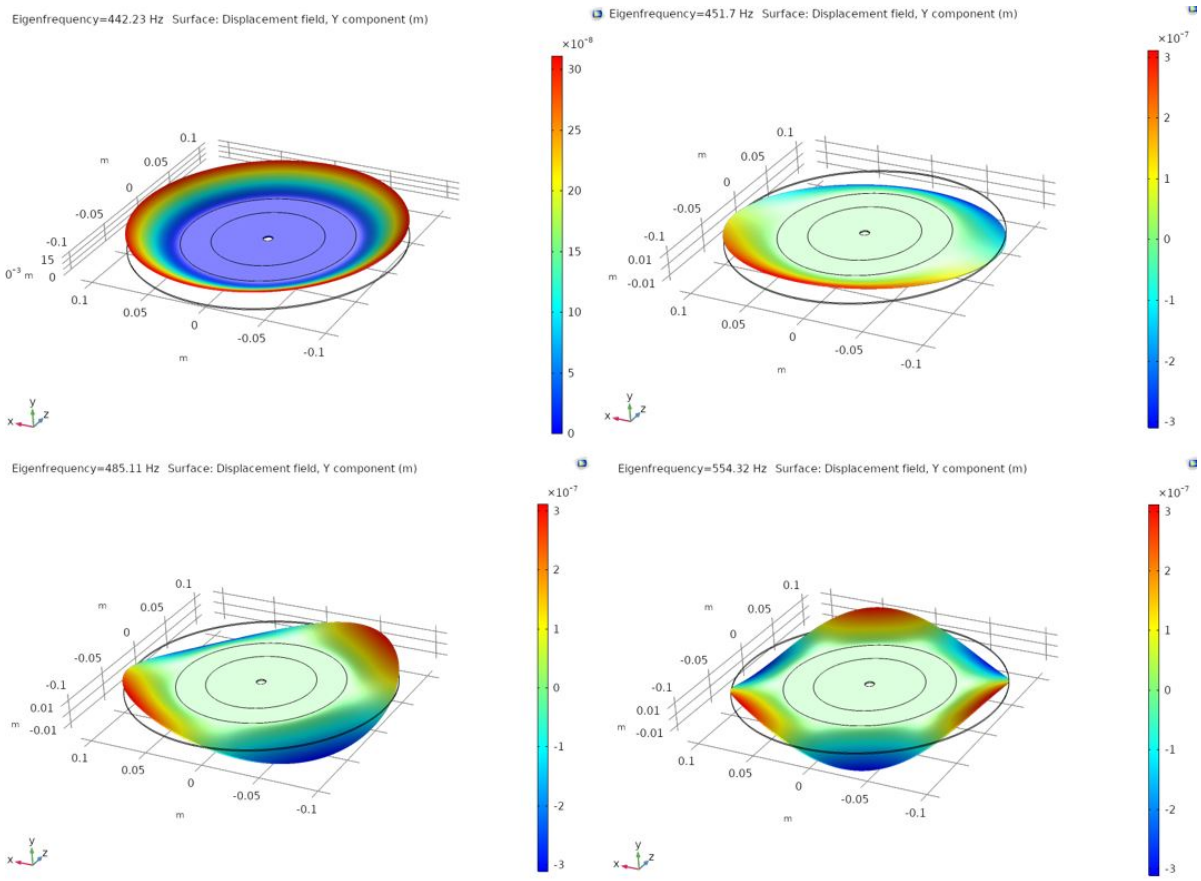

Figure B.2: First four eigen modes.

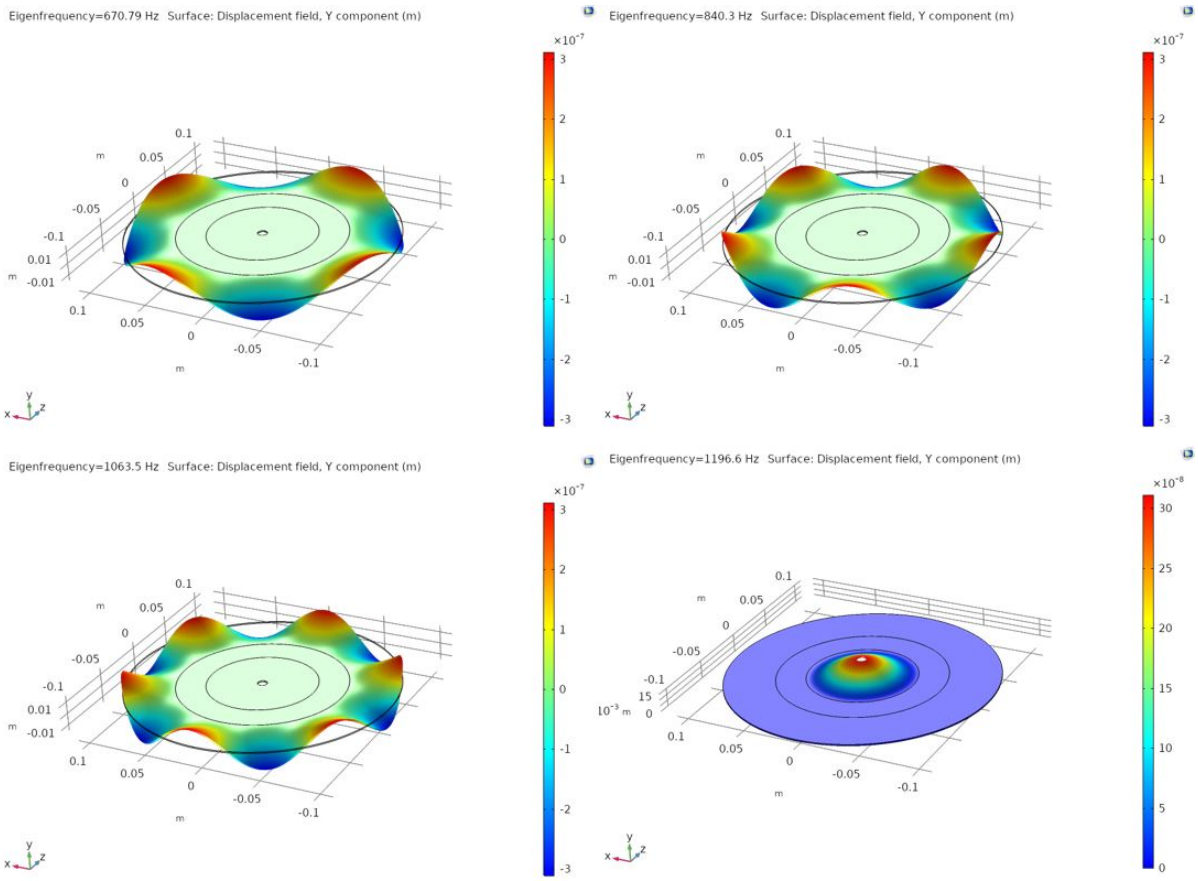

Figure B.3: Eigen modes five to eight.

C

Procedure for air bubble removal

While filling the fluid chamber **5**, in figure 3.4, air bubbles will get trapped at the top surface. These bubbles have to be removed or else the they will absorb the piezo perturbations since they deform easier than the liquid. So in order to remove the bubbles provisions were made in the fluid chamber as shown in figure C.1. This figure shows a tube with many holes at the top surface of the fluid chamber. A schematic of bubble removal technique is shown in figure C.2. The air bubbles are trapped at the top are shown in the figure. A syringe with the liquid is attached to the nozzle and water is forced into the fluid chamber after closing the inlet valve from gravity pump. This increases the pressure inside the fluid chamber. This increased pressure is stronger than the buoyancy force that is keeping the air at the top of the fluid chamber. Hence the air bubbles are forced to come out through the tube that is in the top of the fluid chamber. Complete removal of bubbles cannot be ascertained as the chamber is opaque, although a simple test can be done by pressure measurement. Once the bubbles are removed, the piezo perturbations are switched on and the pressure is measured as a function of time. If the FFT of the pressure signal gives the same frequency as the piezo perturbation frequency then it is sure that the largest air bubbles are removed. The FFT was performed on the time signal by the software that does data acquisition. The length of the time signal for FFT can be given as an input to the software.

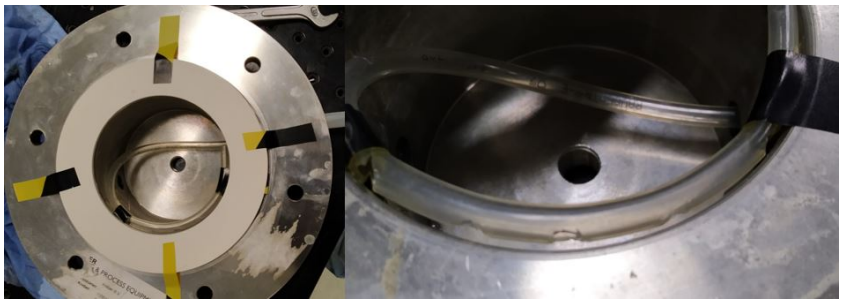

Figure C.1: Provisions for bubble removal.

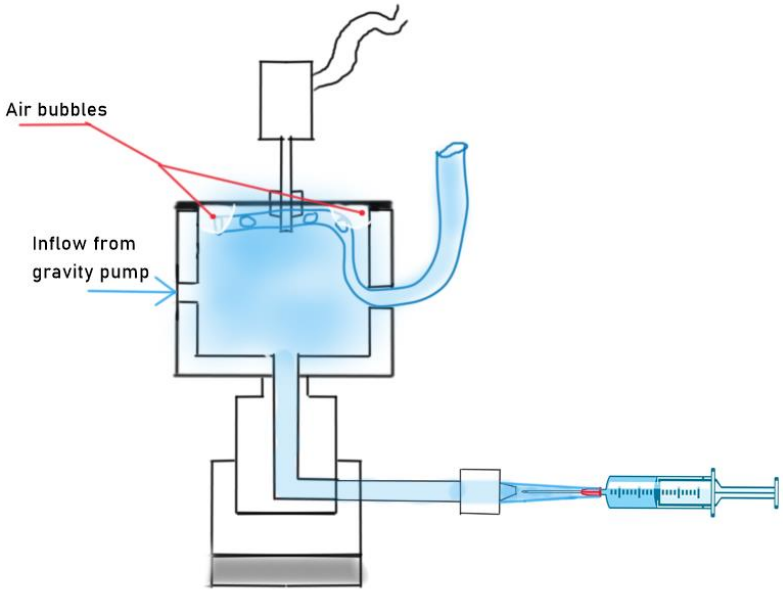

Figure C.2: Bubble removal schematic.

D

Derivations of linear stability equations

The kinematic condition and the momentum equation in the streamwise direction is repeated here given in equations D.1 and D.2.

$$\frac{\partial h}{\partial t} + u\frac{\partial h}{\partial s} + \frac{h}{2}\frac{\partial u}{\partial s} = 0 \tag{D.1}$$

$$\rho\left(\frac{\partial u}{\partial t} + u\frac{\partial u}{\partial s}\right) = -\gamma\frac{\partial \kappa}{\partial s} + 3\mu\frac{\partial^2 u}{\partial s} \tag{D.2}$$

The equations for the radius and velocity is given as,

$$h(s,t) = h_0(s) + \tilde{h}(s,t) \tag{D.3}$$

$$u(s,t) = u_0(s) + \tilde{u}(s,t) \tag{D.4}$$

$$\tilde{h}(s,t) = \epsilon_h e^{i(ks-\omega t)} \tag{D.5}$$

$$\tilde{u}(s,t) = \epsilon_u e^{i(ks-\omega t)} \tag{D.6}$$

Substituting equations D.3 and D.4 in equation D.1 gives,

$$\frac{\partial \tilde{h}}{\partial t} + u_0\frac{\partial h_0}{\partial s} + u_0\frac{\partial \tilde{h}}{\partial s} + \tilde{u}\frac{\partial h_0}{\partial s} + \frac{h_0}{2}\frac{\partial u_0}{\partial s} + \frac{h_0}{2}\frac{\partial \tilde{u}}{\partial s} = 0 \tag{D.7}$$

The kinematic condition for base flow is given as,

$$u_0\frac{\partial h_0}{\partial s} + \frac{h_0}{2}\frac{\partial u_0}{\partial s} = 0 \tag{D.8}$$

Subtracting equation D.7 by base flow equation D.8 yields,

$$\frac{\partial \tilde{h}}{\partial t} + u_0\frac{\partial \tilde{h}}{\partial s} + \tilde{u}\frac{\partial h_0}{\partial s} + \frac{h_0}{2}\frac{\partial \tilde{u}}{\partial s} + \frac{\tilde{h}}{2}\frac{\partial u_0}{\partial s} = 0 \tag{D.9}$$

Now substituting equations D.5 and D.6 in equation D.9 gives,

$$\epsilon_h(-i\omega)e^{i(ks-\omega t)} + u_0\epsilon_h(ik)e^{i(ks-\omega t)} + \epsilon_u e^{i(ks-\omega t)}\frac{\partial h_0}{\partial s} + \frac{h_0}{2}\epsilon_u(ik)e^{i(ks-\omega t)} + \frac{\epsilon_h}{2}e^{i(ks-\omega t)}\frac{\partial u_0}{\partial s} = 0 \tag{D.10}$$

Dividing this equation by $e^{i(ks-\omega t)}$ and equating the imaginary parts to zero gives equation D.11 which is the same as 4.7

$$(ku_0 - \omega)\epsilon_h + \frac{kh_0}{2}\epsilon_u = 0 \tag{D.11}$$

A similar approach is adopted for equation D.2, the only new term encountered here is the spatial derivative of curvature term. Subtracting the perturbed momentum equation by the base flow momentum equation and ignoring the viscous terms yields,

$$\frac{\partial \tilde{u}}{\partial t} + u_0 \frac{\partial \tilde{u}}{\partial s} + \tilde{u} \frac{\partial u_0}{\partial s} - \frac{\gamma}{\rho} \left(\frac{1}{h_0^2} \frac{\partial \tilde{h}}{\partial s} - \frac{2\tilde{h}}{h_0^3} \frac{\partial h_0}{\partial s} + \frac{\partial^3 \tilde{h}}{\partial s^3} \right) = 0 \tag{D.12}$$

By substituting equations D.5 and D.6 in equation D.12 and equating the imaginary terms will result in equation D.13 which is the same as equation 4.8,

$$\frac{\gamma k}{\rho} \left(k^2 - \frac{1}{h_0^2} \right) \epsilon_h + (k u_0 - \omega) \epsilon_u = 0 \tag{D.13}$$

E

Error estimation

The standard deviation (SD) for the non-dimensionalized wave number, growth rate and jet velocity has to be found to plot the experimental values on the theoretical graphs. The non-dimensionalized wave-number is given as,

$$k_r^* = \frac{2\pi H}{\lambda} \tag{E.1}$$

From this the standard deviation on k_r^* is given as,

$$SD_{k_r^*} = \sqrt{\left(\frac{\partial k_r^*}{\partial \lambda}\right)^2 (SD_\lambda)^2 + \left(\frac{\partial k_r^*}{\partial H}\right)^2 (SD_H)^2} \tag{E.2}$$

Where the uncertainty of the nozzle inner diameter SD_H is measured experimentally. The standard deviation of the λ is given as,

$$SD_\lambda = \sqrt{\frac{1}{N-1}\sum(\lambda_i - \lambda_{mean})^2} \tag{E.3}$$

The non-dimensionalized velocity is given as,

$$u_0^* = \frac{f\,\lambda}{U} \tag{E.4}$$

where f is the frequency of perturbation and U is the velocity at the nozzle. The uncertainty in u_0^* is given as,

$$SD_{u_0^*} = \sqrt{\left(\frac{\partial u_0^*}{\partial \lambda}\right)^2 (SD_\lambda)^2 + \left(\frac{\partial u_0^*}{\partial U}\right)^2 (SD_U)^2} \tag{E.5}$$

The uncertainty in nozzle velocity is measured by repeating the experiments.

Finally the error in the capillary growth rate has to be measured. The capillary growth rate is the slope of the line fit into the equation E.7,

$$h_{crest}(t) = h_0 + \epsilon_h e^{(\omega_i t)} \tag{E.6}$$

$$h_{crest}(t) - h_0 = \epsilon_h e^{(\omega_i t)} \tag{E.7}$$

h_{crest} is the radius of the swell measured at every time instance. The diameter of the crest is the distance between the two edges of the jet. Each edge detection has a an error of half a pixel and the h_{crest} has an error of 1/2 pixels on imaging plane. h_0 the local unperturbed jet radius is calculated from the local velocity which also has an error associated with it. By error propagation the error on $h_{new}(t) = h_{crest}(t) - h_0$ at every time instance is found. As the next step is taking the logarithm of the values $h_{new}(t)$, the error propagation is given as,

$$\delta ln(h_{new})(t) = \delta h_{new}/h_{new}(t) \tag{E.8}$$

Before taking the logarithm, the errors on all the points were the same (i.e.) δh_{new} was constant for all points, but after taking the log, the error in each time instance is different.

As the error at each point is different and the slope of that data has to be found, instead of a simple Linear Regression analysis a weighted Linear Regression analysis has to be used. The equations for the slope and the uncertainty in the slope for weighted Linear Regression is taken from the book [41] (Page 198).

Consider X_i be the independent variable, Y_i be the dependent variable and $\sigma_{Y,i}$ be the error at each Y_i. The weights are given as,

$$w_i = 1/\sigma_{Y,i}^2 \tag{E.9}$$

and the slope of the line is given as,

$$Slope = \frac{\sum w \sum wXY - \sum wX \sum wY}{\sum w \sum wX^2 - (\sum wX)^2} \tag{E.10}$$

Finally, the deviation in the slope is given as,

$$SD_{slope} = \sqrt{\frac{\sum w}{\sum w \sum wX^2 - (\sum wX)^2}} \tag{E.11}$$

The last two equations are used to estimate the capillary growth rate and its deviation.

F

Matlab code

F.1. Code for wavelength tracking

```
clear;
close all;
clc;

datadir = 'C:\camera_highspeed\15July\test4\swp1';
bg  = imread(fullfile(datadir,sprintf('bg.tif')));
bg = bg(:,:,1);
st = 6;
en = 11;
Kim  = 0;


for i = st:en

I =imread(fullfile(datadir,sprintf('swp1_%04d.tif',i)));
I = I(:,:,1);
I = imcomplement(I) - imcomplement(bg);
I = imbinarize(I,0.2);
I = medfilt2(I);
% I = imcomplement(I);
% cc = bwconncomp(I);
I = imfill(I,'holes');
cc = bwconncomp(I);
stats = regionprops(cc,'Area');
[~,idx] = max([stats.Area]);
I = ismember(labelmatrix(cc),idx);

if i == st
fh1  = figure(1);
imshow(I);
[x1,y1] = ginput(1);
x1 = round(x1); y1 = round(y1);
hold on
plot(x1,y1,'ro');
[x2,y2] = ginput(1);
x2 = round(x2); y2 = round(y2);
hold on
plot(x2,y2,'ro');
hold on
x = [x1,x1,x2,x2,x1];
y = [y1,y2,y2,y1,y1];
plot(x,y);
pause(1);
close(fh1);
    secI = I (y1:y2,x1:x2);
    leny = size(secI,1);
    lenx = size(secI,2);
    secI = I (y1:y1+leny,x1:x1+lenx);
else
    secI = I(a(3):a(3)+leny,a(1):a(1)+lenx);

end
% fh2 = figure(2);
% imshow(secI);
moving = cast(secI,'single');


J =imread(fullfile(datadir,sprintf('swp1_%04d.tif',i+1)));
J = J(:,:,1);
J = imcomplement(J) - imcomplement(bg);
J = imbinarize(J,0.2);
J = medfilt2(J);

J = imfill(J,'holes');
cc_j = bwconncomp(J);
stats_j = regionprops(cc_j,'Area');
[~,idx_j] = max([stats_j.Area]);
J = ismember(labelmatrix(cc_j),idx_j);
fixed = cast(J,'single');

c = xcorr2(fixed,moving);
[max_c, imax] = max(abs(c(:))); %find the max value
[ypeak, xpeak] = ind2sub(size(c),imax(1)); %Find peak in cross-correlation.

% fh3 = figure(3);
% imshow(J);
% hold on
% plot(xpeak,ypeak,'ro');
% hold on
% plot(xpeak-size(moving,2),ypeak-size(moving,1),'ro');
% pause(1);
% close(fh3)

x1 = xpeak-size(moving,2);
x2 = xpeak;
y1 = ypeak-size(moving,1);
y2 = ypeak;
a = [x1,x2,y1,y2];


p1 = edge(J(a(3):a(3)+leny,a(1):a(1)+lenx));
[,id] = find(p1);
[row,col] = ind2sub(size(p1),id);
col = col + a(1);
row = row + a(3);
p = secI;
% p(1,:) = 1;
% p(end,:) = 1;
edge_I{i-st+1} = p;
Kim = Kim + J;
% K(y(1):y(2),x(1):x(3)) = K(y(1):y(2),x(1):x(3)) + edge_I{i-st+1,:,:};
fh4 = figure(4);
imshow(Kim);
hold on
plot(col,row,'r.');
hold on
pause(0.3);
% save(fh4,sprintf('tem_%d.jpg',i-st+1));
% imshow(edge_I{i-st+1,:,:}, 'ColorMap', [0 0 0; 1 0 0]);

% [optimizer, metric] = imregconfig('multimodal');
% moving_reg = imregister(moving,fixed,'similarity');
% fh3 = figure(3);
% imshowpair(moving_reg)
% % C = cat(1,I,J);
% montage(C);
% I = edge(I);
% imshow(I);
% J = J + I;


end
% %
K = edge_I{1};

for j = st:en-1
    K = cat(2, K,edge_I{j-st+2});

end
figure(2)
imshow(K);

% K_rot = matrix_rot(edge_I{1});
% size1 = size(K_rot);
% for j = st:en-1
%     m = matrix_rot(edge_I{j-st+2});
%     K_rot = cat(2, K_rot,m);
%
% end
%
% figure(3)
% imshow(K_rot);
```

```
%% lambda_extract
diameter = zeros(size(edge_I,2),2);
lambda = zeros(size(edge_I,2),1);
d_min = zeros(size(edge_I,2),1);

fh5 = figure(5);
imshow(edge_I{en-st+1});
q1 = ginput(1);
hold on
plot(q1(1),q1(2),'ro')
q2 = ginput(1);
hold on
plot(q2(1),q2(2),'ro')
pause(0.5);
close(fh5);

min_peak = 0.7 * sqrt( (q1(1)-q2(1))^2 +  (q1(2)-q2(2))^2  );


for j = st:en

    [lambda(j-st+1,1) , diameter(j-st+1,:), d_min(j-st+1,1)] =
    ... matrix_rot(edge_I{j-st+1},min_peak);

end

diam = [(diameter(end,1) - diameter(1,1)), length(diameter(:,1))-1];

pix_s = 11*10^(-6);
M = 0.2057;
d_n = 0.0008;
f = 500;

lam_f = mean(lambda)*pix_s/M;
lambda = (lambda)*pix_s/M;
% blurr = 1.725*10^(-4);
cam_res = pix_s/M;
lam_dev = sqrt((std(lambda)*pix_s/M)^2 + (cam_res)^2);
Kr = pi*d_n/lam_f;
dev_d_n =  20 * 10^(-6);
Kr_dev = sqrt((pi*d_n*lam_dev/lam_f^2)^2 + (pi * dev_d_n/lam_f)^2 );
u_noz = 1.788;
u_noz_dev = 0.027;
u_r = f*lam_f;
u_l = f*lambda/u_noz;
u_fit = polyfit(1:1:length(u_l),u_l',1);
u_l = polyval(u_fit,1:1:length(u_l));

u_r_dev =  f*lam_dev;
u_f = u_r/u_noz;
u_f_dev = sqrt( (u_r_dev/u_noz)^2 + (u_r*u_noz_dev/u_noz^2)^2  );

% growth rate cal
f_acq = 2500;
We = 18.21;
gamma = 0.073;
% g = (2*pi*250/60)^2;
rho = 998;
% r_l = 1./sqrt(u_l);
Rs = 0.5.*diameter(:,1).*pix_s/M;
% Rs2 = 0.5.*diameter(:,2).*pix_s/M;
% r_s = Rs/(d_n/2);
% r_sfit = polyfit(1:1:length(r_s),r_s',1);
% r_s1 = polyval(r_sfit,1:1:length(r_s));

% Rn = 0.5.*d_min.*pix_s/M;
% r_n = Rn/(d_n/2);
% r_nfit = polyfit(1:1:length(r_n),r_n',1);
% r_n1 = polyval(r_nfit,1:1:length(r_n));

temp1 = Rs' - (d_n/2)/sqrt(u_f);
Rs_dev = pix_s/M /2;
Rl_dev = sqrt ( 1/(4*u_f)*dev_d_n^2 + u_f_dev^2 * d_n^2/(16*u_f^3) );
temp1_dev = ones(1,length(temp1)).*sqrt(Rs_dev^2 + Rl_dev^2);
% temp2 = (Rs' - (d_n/2)/sqrt(u_f)) / (d_n/2);
% temp3 = Rs2' - (d_n/2)/sqrt(u_f);

% temp_fit = polyfit(1:1:length(temp1),temp1,1);
% temp1 = polyval(temp_fit,1:1:length(temp1));
temp1_dev = temp1_dev ./ temp1;

temp1 = log(temp1);

time1 = (0:1:length(Rs)-1)./f_acq;
% temp2 = log(temp2);
% ps = polyfit(time1,temp1',1);
% ki_s = ps(1);
% temp2 = log(d_n/2 - Rn);

X = time1;
Y = temp1;
sigY = temp1_dev;
w = 1 ./ (sigY).^2;

del2 = sum(w)*sum(w.*X.^2) - (sum(w.*X))^2;
B = sum(w)*sum(w.*X.*Y) - sum(w.*X).*sum(w.*Y);
B = B/del2;

sig_B = sqrt(sum(w)/del2);
% pn = polyfit(time1,temp2',1);
% ki_n = pn(1);
% temp3 = log(temp3);
% len_eta = time1.*u_r;
wi_swell = B;
wi_swell_dev = sig_B;
% wi_err = sqrt(diag((bint.R)\inv(bint.R'))./bint.normr.^2./bint.df);
% ki_neck = polyfit(len_eta,temp2',1);
% cap_len = sqrt(gamma/(rho * g));
% ki_swell = ki_swell(1)*cap_len;
% ki_neck = ki_neck(1)*cap_len;
%
% rl = (d_n/2)/sqrt(u_f);
% rl = d_n/2;
wi_swell = wi_swell / sqrt(gamma/ (rho*(d_n)^3));
wi_swell = wi_swell / sqrt(We);
ki_swell = wi_swell/u_f;

wi_swell_dev = wi_swell_dev / sqrt(gamma/ (rho*(d_n)^3));
wi_swell_dev = wi_swell_dev / sqrt(We);
ki_swell_dev = wi_swell_dev/u_f;
% wi_err = wi_err(1)/ sqrt(gamma/ (rho*(d_n)^3));
% wi_dev = wi_err / sqrt(We);



% ki_dev = wi_err/u_f;

% wi_f = polyfit(time1,temp3,1);
% wi_f = wi_f(1)/sqrt(gamma/ (rho*d_n^3));
% wi_f = wi_f / sqrt(We);
% ki_f = wi_f/u_f;

%
% ki_f = ki_f(1)*u_noz / sqrt(rho/(gamma*(d_n/2)^3));
% ki_f = ki_f(1)*cap_len;
% res = [Kr,Kr_dev,u_f,u_f_dev,ki_swell];
% res = res';

% ki = Kr^2 - (1/)
pp = [Kr,Kr_dev,u_f,u_f_dev,ki_swell,ki_swell_dev];
pp = transpose(pp);
```

F.2. Code to rotate an individual wavelength and find the radius of crest and trough

```
function [lambda,peks,d_min] = matrix_rot(M,min_peak_dist)


    Ed = edge(M);
    [id] = find(Ed);
    [row,col] = ind2sub(size(M),id);
    polyno = polyfit(col,row,1);

    scale = 1;       % scale factor
    angle = atan((polyno(1))) + pi/2;  % rotation angle
    tx = 0;            % x translation
    ty = 0;            % y translation
    fill = 0;

    sc = scale*cos(angle);
    ss = scale*sin(angle);

    T = [ sc -ss  0;
      ss  sc  0;
      tx  ty  1];

    t_nonsim = affine2d(T);

    m = imwarp(M,t_nonsim,'FillValues',fill);

    ed_m = edge(m);
    d = zeros(1,size(ed_m,1));
    for j = 1:size(ed_m,1)
        pp = find(ed_m(j,:)==1);
        if ( isempty(pp) || length(pp) == 1)
            d(j) = 0;

        else
        if( length(pp) == 2)
            d(j) = abs(pp(2)- pp(1));
        else
             d(j) = abs(pp(end) - pp(1));
        end

        end
    end


% code without smoothing
% [pks,locs] = findpeaks(d,1:1:length(d),'MinPeakDistance',min_peak_dist);
```

```
% smoothing data code
dia = smoothdata(d);
[pks,locs] = findpeaks(dia,1:1:length(d),'MinPeakDistance',min_peak_dist);
peks = [(d(locs(1)-1)+d(locs(1))+d(locs(1)+1))/3, d(locs(2))];
%[d_min, lo]= min(d(locs(1):locs(2)));
lo = round((locs(2) + locs(1))/2);
d_min = (d(lo)+d(lo+1)+d(lo-1))/3;
lambda = abs(locs(2)-locs(1));
fh2 = figure(2);
imshow(m);
hold on
yline(round(locs(1)),'r','LineWidth',2);
hold on
yline(round(locs(2)),'r','LineWidth',2);
hold on
yline(round(lo),'b','LineWidth',2);

pause(0.5);
close(fh2);



end
```

F.3. Code to plot histograms of drop sizes

```
clear;
close all;
clc;

datadir = 'C:\camera_highspeed\15July\test7\swp1';
bg  = imread(fullfile(datadir,sprintf('bg.tif')));
bg = bg(:,:,1);

len = 50;
J = 0;
start = 1;

for i = start:2:len

I =imread(fullfile(datadir,sprintf('swp1_%04d.tif',i)));
% I = I(:,:,1);
% % I = I(195:1318,13:1788);    %test 11 strobe
% % bg = adaptthresh(I,0.7);
% I = imcomplement(I) - imcomplement(bg);
%  I = imbinarize(I);
% I = imcomplement(I);
% I = medfilt2(I);
I = I(:,:,1);
I = imcomplement(I) - imcomplement(bg);
I = imbinarize(I,0.2);
I = medfilt2(I);
I = imfill(I,'holes');
cc = bwconncomp(I);
stats = regionprops(cc,'Area');
[~,idx] = max([stats.Area]);
% s = cc.NumObjects;
I1 = ismember(labelmatrix(cc),idx);
% I = imcomplement(I);
% cc = bwconncomp(I);
I = I - I1;
J = J + I;
end

cc2 = bwconncomp (J);
bubbles_props2 = regionprops(cc2,'Area','BoundingBox','Centroid'
... ,'MajorAxisLength','MinorAxisLength','Orientation','Eccentricity');
idx2 = find([bubbles_props2.Eccentricity] > 0.4 & [bubbles_props2.Eccentricity] < 0.8
... & [bubbles_props2.Area] < 1100  & [bubbles_props2.Area] > 50);
J2 = ismember(labelmatrix(cc2),idx2);
cc3 = bwconncomp (J2);
bubbles_props3 = regionprops(cc3,'Area');

rad = zeros(1,cc3.NumObjects);
for pp = 1: cc3.NumObjects
rad(pp) = sqrt(bubbles_props3(pp).Area/pi);
end

pix_s = 11*10^(-6);
M = 0.2057;

rad = rad.*pix_s/M * 1000;
% J = J / length(start:2:len);
imshow(J2);
rad_n = rad;

%% plotting
% w = rad(min):0.05:rad(max);
rad_n = cat(2,rad_n,rad);


%%
figure(3)
[n1,n2] = hist(rad_n,9);
% n1 = sgolay(n1,11);
n1 = n1./max(n1);
plot(n2,n1);
xlabel('Drop radius (mm)')
ylabel('Normalized number of occurances')
```

Bibliography

[1] Subrahmanyan Chandrasekhar. *Hydrodynamic and hydromagnetic stability*. Courier Corporation, 2013.

[2] K. C. Chaudhary and T. Maxworthy. The nonlinear capillary instability of a liquid jet. Part 3. Experiments on satellite drop formation and control. *Journal of Fluid Mechanics*, 96(2):287–297, 1980. ISSN 14697645. doi: 10.1017/S0022112080002121.

[3] KC Chaudhary and T Maxworthy. The nonlinear capillary instability of a liquid jet. part 2. experiments on jet behaviour before droplet formation. *Journal of fluid mechanics*, 96(2):275–286, 1980.

[4] KC Chaudhary and LG Redekopp. The nonlinear capillary instability of a liquid jet. part 1. theory. *Journal of Fluid Mechanics*, 96(2):257–274, 1980.

[5] Christophe Clanet and Juan C. Lasheras. Transition from dripping to jetting. *Journal of Fluid Mechanics*, 383:307–326, 1999. ISSN 00221120. doi: 10.1017/S0022112098004066.

[6] S. P. Decent, A. C. King, M. J.H. Simmons, E. I. Părău, I. M. Wallwork, C. J. Gurney, and J. Uddin. The trajectory and stability of a spiralling liquid jet: Viscous theory. *Applied Mathematical Modelling*, 33 (12):4283–4302, 2009. ISSN 0307904X. doi: 10.1016/j.apm.2009.03.011.

[7] Russell James Donnelly and W Glaberson. Experiments on the capillary instability of a liquid jet. *Proceedings of the Royal Society of London. Series A. Mathematical and Physical Sciences*, 290(1423):547–556, 1966.

[8] Christophe Dumouchel. On the experimental investigation on primary atomization of liquid streams. *Experiments in Fluids*, 45(3):371–422, 2008. ISSN 07234864. doi: 10.1007/s00348-008-0526-0.

[9] Jens Eggers. Universal pinching of 3d axisymmetric free-surface flow. *Physical Review Letters*, 71(21): 3458, 1993.

[10] Jens Eggers. Eggers RMP 1997. 69(1833):1–65, 1998. URL `papers2://publication/uuid/1329B18C-197E-4787-8771-930B99E1706E`.

[11] Jens Eggers and Todd F. Dupont. Drop Formation in a One-Dimensional Approximation of the Navier-Stokes Equation. *Journal of Fluid Mechanics*, 262:205–221, 1994. ISSN 14697645. doi: 10.1017/S0022112094000480.

[12] Jens Eggers and Emmanuel Villermaux. Physics of liquid jets. *Reports on Progress in Physics*, 71(3), 2008. ISSN 00344885. doi: 10.1088/0034-4885/71/3/036601.

[13] I Frankel and D Weihs. Stability of a capillary jet with linearly increasing axial velocity (with application to shaped charges). *Journal of Fluid Mechanics*, 155:289–307, 1985.

[14] FJ García, H González, JR Castrejón-Pita, and AA Castrejón-Pita. The breakup length of harmonically stimulated capillary jets. *Applied Physics Letters*, 105(9):094104, 2014.

[15] E. F. Goedde and M. C. Yuen. Experiments on liquid jet instability. *Journal of Fluid Mechanics*, 40(3): 495–511, 1970. ISSN 14697645. doi: 10.1017/S0022112070000289.

[16] Helio González and F. J. García. The measurement of growth rates in capillary jets. *Journal of Fluid Mechanics*, 619:179–212, 2009. ISSN 00221120. doi: 10.1017/S0022112008004576.

[17] C. J. Gurney, M. J.H. Simmons, V. L. Hawkins, and S. P. Decent. The impact of multi-frequency and forced disturbances upon drop size distributions in prilling. *Chemical Engineering Science*, 65(11):3474–3484, 2010. ISSN 00092509. doi: 10.1016/j.ces.2010.02.030. URL `http://dx.doi.org/10.1016/j.ces.2010.02.030`.

[18] I. Image expert. URL `http://imagexpert.com/`.

[19] Joseph B. Keller, S. I. Rubinow, and Y. O. Tu. Spatial instability of a jet. *Physics of Fluids*, 16(12):2052–2055, 1973. ISSN 10706631. doi: 10.1063/1.1694264.

[20] Bavand Keshavarz and Gareth McKinley. Kelvin-helmholtz and buckling instabilities for a viscoelastic liquid, 2012.

[21] HC Lee. Drop formation in a liquid jet. *IBM Journal of Research and Development*, 18(4):364–369, 1974.

[22] SJ Leib and ME Goldstein. Convective and absolute instability of a viscous liquid jet. *The Physics of fluids*, 29(4):952–954, 1986.

[23] Samuel Leroux, Christophe Dumouchel, and Michel Ledoux. The stability curve of newtonian liquid jets. *Atomization and sprays*, 6(6), 1996.

[24] Yuan Li, Grigori M Sisoev, and Yulii D Shikhmurzaev. On the breakup of spiralling liquid jets. *Journal of Fluid Mechanics*, 862:364–384, 2019.

[25] Pierre Simon marquis de Laplace. Traité de mécanique céleste. 5, 1805.

[26] Stanley Middleman and J Gavis. Expansion and contraction of capillary jets of newtonian liquids. *The Physics of Fluids*, 4(3):355–359, 1961.

[27] Nima Moallemi, Ri Li, and Kian Mehravaran. Breakup of capillary jets with different disturbances. *Physics of Fluids*, 28(1), 2016. ISSN 10897666. doi: 10.1063/1.4938095.

[28] L. Partridge, D. C.Y. Wong, M. J.H. Simmons, E. I. Părău, and S. P. Decent. Experimental and theoretical description of the break-up of curved liquid jets in the prilling process. *Chemical Engineering Research and Design*, 83(11 A):1267–1275, 2005. ISSN 02638762. doi: 10.1205/cherd.05090.

[29] W. T. Pimbley and H. C. Lee. Satellite Droplet Formation in a Liquid Jet. *IBM Journal of Research and Development*, 21(1):21–30, 1977. doi: 10.1147/rd.211.0021.

[30] Joseph Plateau. Experimental and static static theory of liquids subjected only to molecular forces. 2, 1873.

[31] Lord Rayleigh. Lord Rayleigh on the Instability of Jets. *Proceedings of the London Mathematical Society*, s1-10(1):4–13, 1878. ISSN 00246115. doi: 10.1145/3007748.3018280.

[32] Lord Rayleigh. Xvi. on the instability of a cylinder of viscous liquid under capillary force. *The London, Edinburgh, and Dublin Philosophical Magazine and Journal of Science*, 34(207):145–154, 1892.

[33] Osborne Reynolds. Iv. on the theory of lubrication and its application to mr. beauchamp tower's experiments, including an experimental determination of the viscosity of olive oil. *Philosophical transactions of the Royal Society of London*, (177):157–234, 1886.

[34] Mina Rohani, Faryar Jabbari, and Derek Dunn-Rankin. Breakup control of a liquid jet by disturbance manipulation. *Physics of Fluids*, 22(10), 2010. ISSN 10706631. doi: 10.1063/1.3494610.

[35] Saad N Saleh, Shakir M Ahmed, Dawood Al-mosuli, and Shahzad Barghi. Basic design methodology for a prilling tower. *The Canadian Journal of Chemical Engineering*, 93(8):1403–1409, 2015.

[36] F 'e lix Savart. M 'e moire on the shock of a liquid vein launched é e against a circular plane. *Ann. chem*, 54(56):1833, 1833.

[37] Vivek Sharma, Simon J Haward, James Serdy, Bavand Keshavarz, Asa Soderlund, Phil Threlfall-Holmes, and Gareth H McKinley. The rheology of aqueous solutions of ethyl hydroxy-ethyl cellulose (ehec) and its hydrophobically modified analogue (hmehec): Extensional flow response in capillary break-up, jetting (rojer) and in a cross-slot extensional rheometer. *Soft matter*, 11(16):3251–3270, 2015.

[38] Yulii D Shikhmurzaev and Grigori M Sisoev. Spiralling liquid jets: verifiable mathematical framework, trajectories and peristaltic waves. *Journal of Fluid Mechanics*, 819:352–400, 2017.

[39] Maksym Skydanenko, Vsevolod Sklabinskyi, Saad Saleh, and Shahzad Barghi. Reduction of dust emission by monodisperse system technology for ammonium nitrate manufacturing. *Processes*, 5(3), 2017. ISSN 22279717. doi: 10.3390/pr5030037.

[40] Speaker. Specifications of beyma speakers. URL `https://usspeaker.com/beyma%206MI90-1.htm`.

[41] John Taylor. *Introduction to error analysis, the study of uncertainties in physical measurements*. 1997.

[42] S Tomotika. Breaking up of a drop of viscous liquid immersed in another viscous fluid which is extending at a uniform rate. *Proceedings of the Royal Society of London. Series A-Mathematical and Physical Sciences*, 153(879):302–318, 1936.

[43] CM Van't Land. *Industrial crystallization of melts*. CRC Press, 2004.

[44] I. M. Wallwork, S. P. Decent, A. C. King, and R. M.S.M. Schulkes. The trajectory and stability of a spiralling liquid jet. Part 1. Inviscid theory. *Journal of Fluid Mechanics*, 459:43–65, 2002. ISSN 00221120. doi: 10.1017/S0022112002008108.

[45] D. C.Y. Wong, M. J.H. Simmons, S. P. Decent, E. I. Parau, and A. C. King. Break-up dynamics and drop size distributions created from spiralling liquid jets. *International Journal of Multiphase Flow*, 30(5):499–520, 2004. ISSN 03019322. doi: 10.1016/j.ijmultiphaseflow.2004.04.002.

[46] Thomas Young. Iii. an essay on the cohesion of fluids. *Philosophical transactions of the royal society of London*, (95):65–87, 1805.

[47] Man Chuen Yuen. Non-linear capillary instability of a liquid jet. *Journal of Fluid Mechanics*, 33(1):151–163, 1968. ISSN 14697645. doi: 10.1017/S0022112068002429.